DESIGN OF A TWO-COMPONENT PASSIVE DYNAMIC SUNSHADE COMBINING SHAPE MEMORY ALLOYS AND KNITTED TEXTILE

MASTER'S THESIS

VALERIO LANFRANCO

Research report for Master's Thesis

in fulfilment of the requirements for the degree of Master of Science in Building Engineering, at the Delft University of Technology, to be defended publicly on the 18th of September 2023

Author:

Valerio Lanfranco

5541840

MSc Building Engineering - Building Physics and Technology Track

Chairperson:

Dr. M.A. Popescu - Applied Mechanics, TU Delft

Committee:

Dr. ir. H.R. Schipper - Applied Mechanics, TU Delft

Dr. A. Luna Navarro - Architectural Engineering and Technology, TU Delft

Ing. G. Peters - ABT

To the unexpected.
And to the joy in it.

ABSTRACT

To lessen our influence on the environment, we are moving towards solutions that can meet our needs of shelter, nutrition, mobility, communication, and health with little to no energy or resources. In the construction industry, adaptive façades have gained attention for their capacity to adapt to changing conditions. These façades can modify their state in response to varying factors such as temperature and sunlight. This adaptability offers potential benefits in energy efficiency and occupant comfort, making them significant in architectural advancement. Despite being promising, these technologies are seldom used in buildings because they consist of numerous components and intricate mechanisms that can hinder their overall lifespan. To find more straightforward solutions for these systems, designers and researchers have focused on Smart Materials in combination with passive strategies. Shape Memory Alloys (SMAs), in particular, have found applications in diverse designs owing to their dual functionality as temperature sensors and actuators. SMAs have the remarkable ability to 'remember' their original shape and can revert to it when subjected to specific temperatures. This unique trait enables them to serve as both sensors, by detecting temperature changes, and actuators, by initiating shape changes in response to those shifts. However, current SMA-based sunshade designs do not provide visual contact with the exterior, as they continuously block the occupant's field of view. This work aims at lowering the mechanical complexity of SMA-based sunshades while maintaining thermal comfort and visual contact with the exterior. The first part highlights the significance of precise control strategies for effective sunshade designs. The research emphasizes the importance of tailored control methods aligned with climate conditions. The conclusion underscores that an optimal sunshade design must balance cooling demand reduction, thermal comfort maintenance, and opening hours. Mechanical designs should minimize components while ensuring maximal stroke capabilities. The mechanical design of the counterAKT system exhibited promising stroke results despite not reaching the 200% benchmark. Further research avenues are suggested for textiles and Shape Memory Alloys (SMAs). Integration of findings from both materials is essential for realizing a complete working counterAKT system. Nodal thermal modeling provided insights into the major factors influencing SMA temperature in the counterAKT system. Solar radiation and convective heat transfer were identified as key contributors. The conclusion recommends future research to shift reliance from outdoor air temperature to solar radiation by enhancing emissivity, reducing convection losses, and concentrating solar radiation on the SMA. Finally, The system's feasibility is demonstrated through a small-scale prototype, affirming its practical viability and potential applicability.

CONTENT

ACKNOWLEDGMENTS

I would like to begin my acknowledgments by expressing my deep gratitude to my thesis advisors, who have played pivotal roles in my academic journey.

Mariana, you have not only been a tutor but also an inspiration. Your guidance and passion for our field have been fundamental in shaping my research. I appreciate your dedication to the CocoFab group and your support for the students.

Alessandra, your name is well-known to everyone, and rightfully so. Your insistence on scientific rigor and the *legendary* literature review were transformative experiences. Yet, your role in my life transcends that of a professor. You have been my mentor, providing both demanding challenges and unwavering support. You believed in me when I needed it most, and for that, I am profoundly grateful. Your passion for your work is contagious, and I hope you continue to inspire others as you have inspired me.

Gertjan, you were my introduction to the professional world beyond academia, and I couldn't have asked for a better mentor. Throughout my internship and thesis, you treated me not just as a student but as a valued consultant. Your openness to my ideas and opinions, even as a first-year master's student, was truly encouraging. Thank you for welcoming me to ABT and for imparting the wisdom of "work hard, rest hard."

Roel, though our interactions were brief, I want to acknowledge your guidance and the challenging questions you posed during our meetings. Your understanding when I made mistakes and your gentle reminders were invaluable to my growth.

I extend my heartfelt appreciation to both TU Delft for providing an exceptional academic environment and to ABT for their warm welcome and support throughout my research project. The colleagues at ABT consistently offered fresh perspectives and ideas that enriched my work.

I want to express my deep gratitude to my family, each and every member. Special thanks to Zia Silvia for our meaningful chats and to Zia Patty for always being there for me and my mother.

To my mother, Barbara, and my sister, Barbie, these two years have been challenging for both of us, yet we persevered and triumphed over obstacles that seemed insurmountable. Thank you, mamma, for always being there, answering random video calls, and being happy just to hear me talk about topics you may not fully understand but still rejoice in my enthusiasm. Thank you for the opportunities you have provided and for being my mother.

To my father, Alessandro. I am proud of our ability to see things from each other's perspectives and to realize that it's not as easy as it may seem from the outside. Thank you, papà, for providing me with what you did not have and for always being proud of my achievements, even my mistakes, which, as we know, are where we truly learn.

Edo, while you may not have supported me financially or emotionally, your smile means the world to me. I want you to be proud of me when you look at your big brother. Keep being you, because it is my favorite thing.

Mina and Valerio, if I am the support of your old age, you are the pillars of my youth. You have always been there to catch me when I felt like falling. I want to thank you for being more important than you might realize, for having the broadest smiles when you see me, for marking my arrival date on the calendar and counting the days. Thank you for being here, even though in your eyes, I am still going to *school*.

I want to thank the family I chose—my friends. I want to thank the ones from Casale, who always welcome me when I come back, and the ones from Delft, who never failed in making me feel at home. In addition, I want to thank Francesco, Ellen, Matteo, Laura, Riccardo, and Aurora.

Iliana, I am immensely grateful for your presence. You've shown me that it's okay to be vulnerable and authentic. Thank you for revealing the real Valerio, whom you love deeply. Thank you for being there in front of BK, for supporting my decisions, and for being my family here. I love you.

Santiago, our friendship has been a remarkable journey, from chaotic beginnings to calling each other hermanas. I wouldn't have it any other way. You started as a closed book, but I gradually discovered the kind-hearted and diplomatic person you are. Thank you, Santiago, for your unwavering support, your companionship, and for accepting me, obnoxious quirks and all.

Ivan, never in my wildest dreams did I expect to meet someone like you. Thank you for believing in me when I couldn't, for your protective words and hugs and for showing me what I deserve.

Simone, my high school friend, you have always been by my side, and I trust you more than anyone else in the world. Thank you for never getting tired of me, for always being there, and for making me feel safe while confiding to you.

Ludovica, despite the fact that we have spent more time apart than together, my love for you knows no bounds. Thank you for listening to my dramas, even from the other side of the world. Thank you for always accommodating me, for never abandoning me, even when the distance was vast. Thank you for our *Giovedì spill the tea*, I always wish for more of them.

In conclusion, I would like to express my sincere gratitude to the *unexpected* itself, for it has been an unforeseen force that reshaped my path in ways I could never have imagined. The *unexpected* challenged my preconceptions, shattered my certainties, and then, in the midst of chaos, allowed me to rebuild them with newfound strength. It introduced me to remarkable individuals who became pillars of support and inspiration throughout my academic journey. These unforeseen relationships, the mentors, friends, and even the challenging moments, have been invaluable in shaping my growth and determination. I've learned that welcoming the *unexpected* can lead to some of life's most heartwarming and transformative moments, and for these cherished experiences, I am profoundly grateful.

To the unexpected.

And to the joy in it.

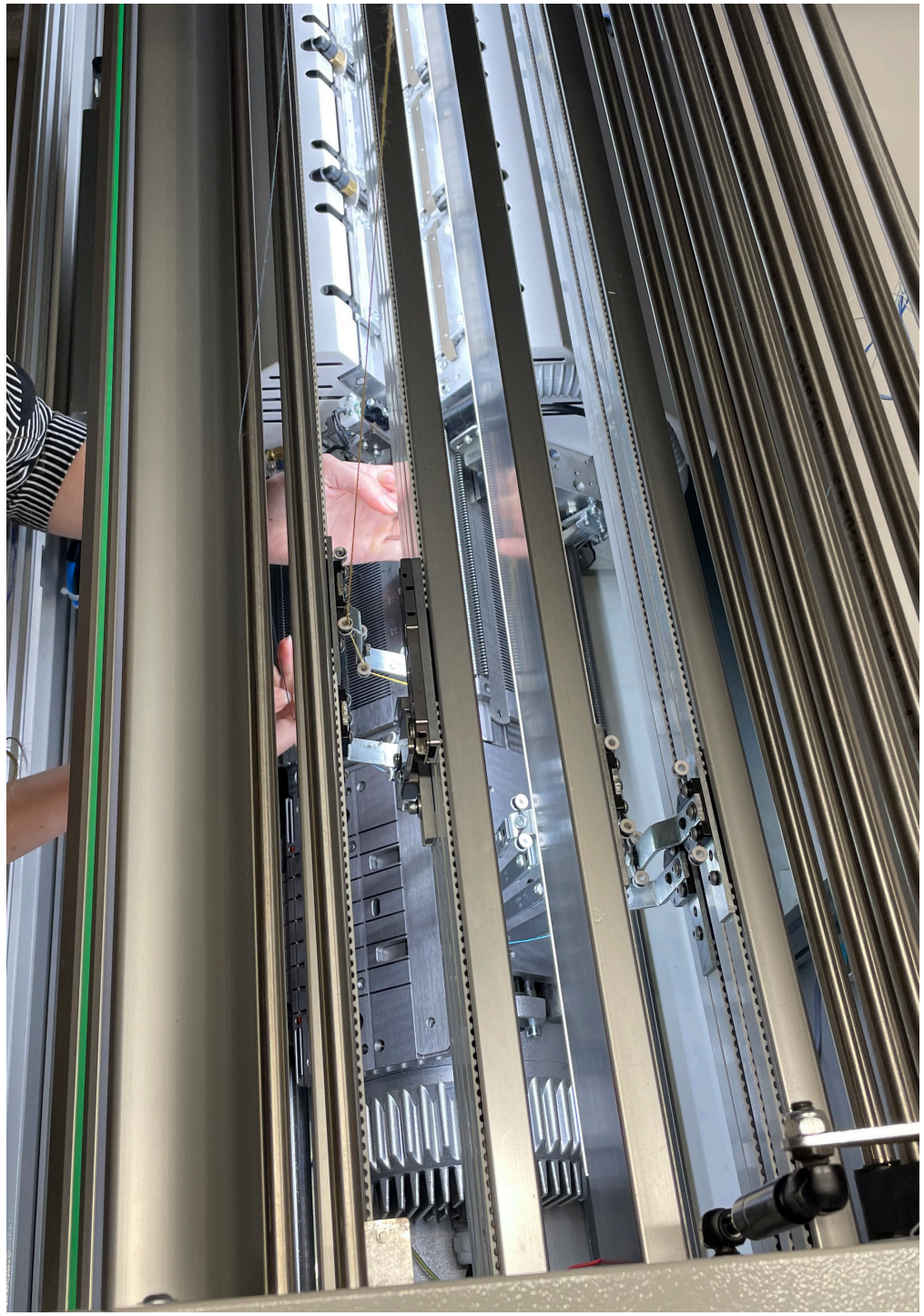

INTRODUCTION

This chapter aims to provide an introduction and context for the research presented in this thesis. The problem is identified and explained, then the overarching research question, the sub-questions, and the thesis structure is presented.

1.1 THE IMPORTANCE OF ADAPTIVE FAÇADES

Today, buildings in the European Union contribute to 40% of energy consumption and 36% of greenhouse gas emissions, primarily due to construction, usage, renovation, and demolition activities (European Commission, 2020). The effects of climate change can be seen in the rising frequency of heatwaves, droughts, and floods, but most notably in the overall increase of temperature worldwide (United Nations Department of Economic and Social Affairs, 2022).

Air conditioning and electric fans are increasingly prevalent, especially in hotter regions globally. These devices contribute to roughly 10% of total global electricity usage. The rising demand for cooling solutions is expected to result in a more than threefold increase in cooling requirements by 2050 (International Energy Agency, 2018). Elevated cooling demand contributes to environmental degradation, ultimately leading to higher temperatures, and thereby, necessitating even greater cooling measures.

In addition to serving structural, weathertightness, and building movement accommodation roles, façades encompass the crucial function of enhancing energy efficiency. They exhibit a capacity for substantial reduction in energy consumption by acting as an interface between the interior and exterior environments (Boswell, 2013). Within the building envelope, glazing systems remain the most vulnerable element concerning heat dissipation. The most straightforward approach might involve curtailing the window area, but this approach would compromise occupant comfort. Natural light is indispensable for the well-being and productivity of inhabitants, both in living and working environments. Conversely, expanding window area raises the potential for summertime overheating in living spaces (Jezierski & Zukowski, 2023).

Adaptive façades could be promising candidates to help reduce the energy demand of buildings during the use stage. In contrast to conventional static façades, adaptive façades can change their performance in response to changes in boundary conditions. (Attia, et al., 2018; Voigt, et al., 2022). The most effective designs to save energy are sunshades that lower the cooling energy demand by minimizing solar gains (Bui, et al., 2020; Al-Masrani et al., 2018; Loonen, et al., 2013) while increasing user comfort (Luna-Navarro, et al., 2023).

1.2 PROBLEM STATEMENT

The implementation of adaptive façades is hindered by their higher complexity and cost during the operational phase (Loonen, et al., 2013). Furthermore, despite being the most important to experts, weight, durability, complexity, and environmental impact are seldom covered in research (Voigt, et al., 2022). The potential gap between expert concerns and current research priorities creates a challenge for adopting adaptive façades in the construction industry (Attia, et al., 2018).

One method to address complexity involves exploring how adaptive facades can offer adaptability. In this context, "adaptability" refers to the ability of a system or structure to alter its configuration or behavior in response to changing conditions, requirements, or demands. Generally, adaptability can be achieved through either active systems, which require an external stimulus to activate, or passive systems that rely on material behavior and physical phenomena (Loonen, et al., 2013). Passive solutions have an advantage over active ones due to their operational simplicity with few components and the lack of high-tech electronic components (Böke, et al., 2022).

Amongst passive strategies, Shape Memory Alloys (SMAs) have been widely used in sunshade designs. These metals switch between two solid phases: the austenitic phase, existing at higher temperatures, and the martensitic phase, present at lower temperatures. A solid phase refers to a distinct arrangement of atoms or molecules within a material, characterized by its unique structure and properties (Yamauchi, et al., 2011). The solid phase change affects the mechanical properties of the metal, i.e., the modulus of rigidity, making them suitable candidates as sensors and actuators.

In addition, the role of textiles utilized in the development of sunshades is often unexploited. Aside from their primary function of providing shade, textiles can also exhibit tension-holding properties and serve as an active component in dynamic shading systems. Currently, no designs actively involve textiles in the mechanical system.

1.3 RESEARCH QUESTIONS

The main question this research answers is:

"How can we combine knitted textile and shape memory alloys to create an effective passive dynamic sunshade?"

The question arises from the gap identified in the world of SMA-based sunshade designs, as explained in Chapter 2, where the full potential of these innovative materials has yet to be grasped due to the persisting presence of numerous components. To minimize the number of components, textiles have been chosen as candidates to counteract the SMA while providing shade when needed. However, no examples are currently present, and the mechanical and building physics aspects of such a system must be investigated. These are: a) the mechanical relationship between the textile and the SMA that will provide enough movement to not continuously occupy the field of view, and b) the relationships that regulate the SMA temperature to provide an effective design.

To answer the overarching research question, the following sub-research questions have been formulated:

1. What are the characteristics of an effective dynamic sunshade?
2. How can the textile be designed to provide a sufficient range of movement for an effective operation?
3. How can the SMA spring be designed to accommodate the movement of the textile?
4. What are the primary factors influencing the temperature of the SMA spring?

1.4 THESIS STRUCTURE

This thesis is structured in eight chapters. Chapter 1 presented the context and the motivation for this work, followed by the question that arose during the problem statement. Chapter 2 provides a state-of-the-art of current passive systems with a focus on SMA and SMA-based sunshade designs. Chapter 3 presents the overarching methodology adopted to answer the research questions. Chapters 4, 5, and 6 present detailed methodologies, results, and discussions over the three main topics of this work. These are namely: effectiveness, mechanical design, and thermal behavior.

Chapter 7 dives into ideas for future designs aimed at increasing the efficiency of the system. Finally, chapter 8 concludes the work by reflecting on the presented research findings and looking to future work.

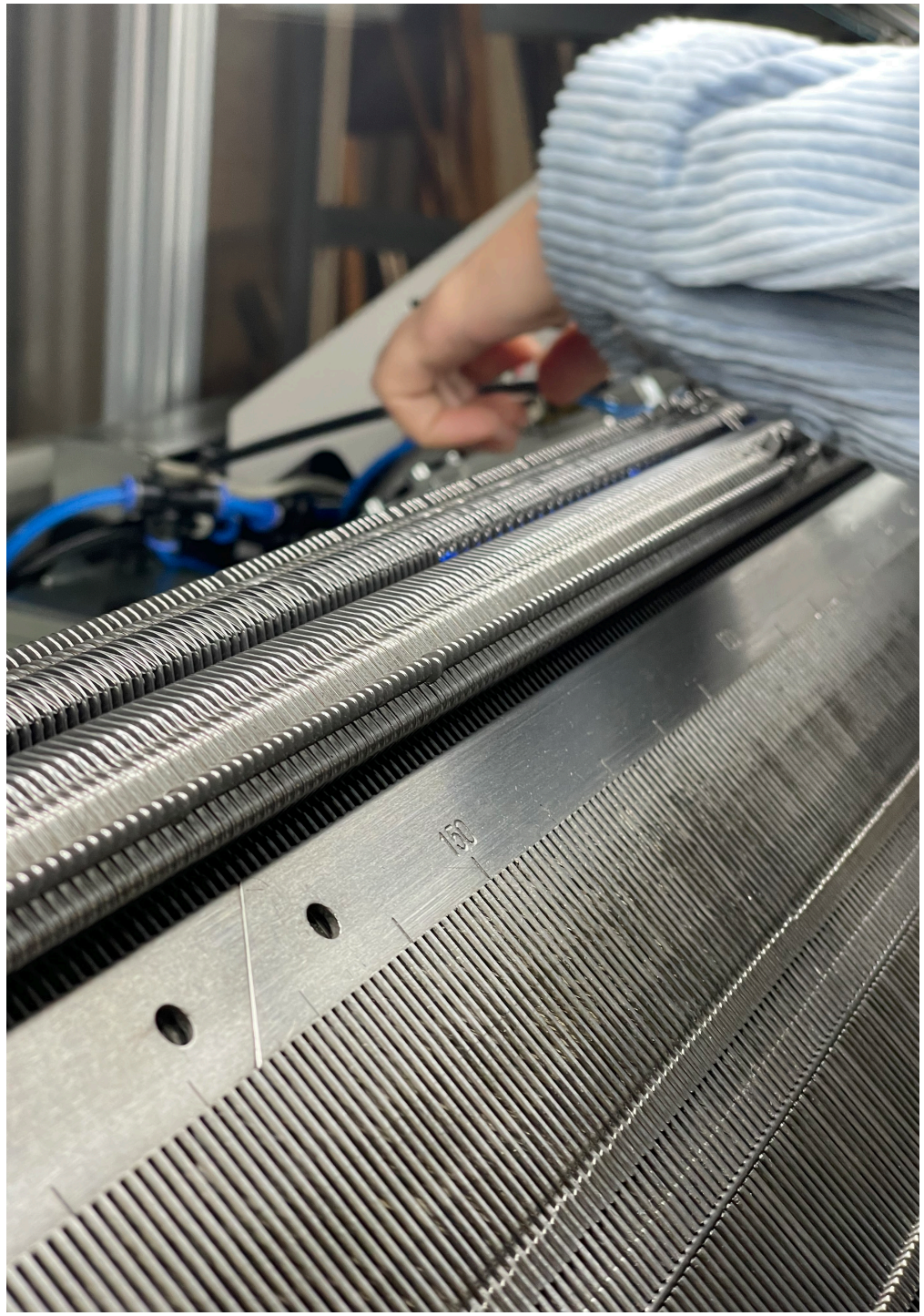

STATE-OF-THE-ART

This chapter discusses the latest developments in the topics mentioned in section 1.2. Section 2.1 outlines the challenges associated with adaptive façades. Section 2.2 highlights how passive solutions can resolve these difficulties and overviews current passive strategies for possible sunshade applications. Since this thesis concentrates on SMA actuators, section 2.3 explains how these metals operate. Section 2.4 discusses the current designs of SMA-based sunshades, while section 2.5 identifies textiles as potential options to play an active role in the mechanical design. Finally, section 2.6 summarizes the findings concluding the state of the art.

In this work, adaptive façades are those building envelopes characterized by (Loonen, et al., 2013):

> *"the ability to repeatedly and reversibly change some of its functions, features or behavior over time in response to changing performance requirements and variable boundary conditions, and does this with the aim of improving overall building performance."*

As the following review was aimed at finding the best passive solution for developing a system able to deliver dynamicity as to reduce solar gains a systematic review was performed with the following keywords: (passive or smart or intrinsic) and (materials or strategies or control) and (adaptive or dynamic or kinetic) and (facade or envelope or building skin).

2.1 BARRIERS TO THE ADOPTION OF ADAPTIVE FAÇADES

To identify the difficulties involved in the design of adaptive façades, Voigt et al. (2022) thoroughly analyzed existing literature and interviewed specialists in the façade sector. The study found that the primary subjects mentioned by professionals during interviews differed from those covered in literature. During the former, 40% of the experts mentioned weight, while just 2% of the literature that was examined covered this topic. The same is true for other topics, including durability, complexity, and environmental impact, which were mentioned by 25% of the experts in the interviews but were only addressed in 10%, 6%, and 9% of the analyzed literature, respectively.

A study by Mols et al. (2017) aimed to find the most suitable solution in terms of cost, complexity, thermal resistance, and aesthetic value, with the help of industry specialists in energy efficiency. Based on their findings, professionals ranked the complexity of construction and cost of ownership as the two most important factors, giving them a weight of 25% and 20%, respectively, on the weighing table out of 100%.

Similarly, Attia et al. (2018) report that many professional interviewees rank costs as the most crucial factor, followed by energy use and occupant satisfaction. The report also suggests creating and sharing an experimental dataset for adaptive façades, as well as encouraging further research into the circularity of the materials employed.

Through twenty-seven interviews with experts, a coding scheme, and quotations, Attia

et al. (2020) identify "comfort and well-being" as the most cited topic and "occupant interaction" as another one high on the frequency list. When designing modern façades, it's important to consider the complexity of the systems being used, as well as the costs associated with the components and their maintenance. However, it's worth noting that even with adaptive facades, traditional challenges such as building physics, tolerances, fire safety, and structural loads still need to be considered.

2.2 PASSIVE STRATEGIES FOR ADAPTIVE SHADING TECHNOLOGIES

There are two key methods for establishing adaptability: first, using a strategy that relies on material behavior and physical phenomena such as the phase change of materials, the hygroscopic properties of wood or the atomic arrangement of a material. Passive systems rely on smart materials that respond to and react to a specific environmental stimulus. The primary energy for the activation to begin comes from environmental resources. Due to its inherent actuation capabilities and the autonomy of its operation, Loonen et al. (2013) categorize this passive technique as intrinsic adaptation. The second strategy depends heavily on using automation technologies and digital control as high-tech solutions. According to Loonen et al. (2013), these systems can be classified as extrinsic because an external stimulus is necessary to cause modifications.

Böke et al. (2022) analyze two case studies to compare the key differences between active and passive systems. They showed that passive solutions have an advantage over active automated adaptive ones due to their operational simplicity with few components and the lack of high-tech electronic components. Furthermore, they conclude that the passive solutions rely on independence from a secondary energy source and are less sensitive to technical mistakes.

Considering the ease of operation associated with passive systems and the established capacity of sunshade designs to minimize cooling demands, the focus of the papers examined within this literature review was to identify the most appropriate passive solution for incorporation into sunshade design.

The findings on the various passive systems are summarized in table 2.1. The table only covers the most cited technologies for which different arguments were given. For each technology a subsection explains the main findings.

Table 2.1 Passive systems present in literature. Properties and applicability potential as sunshading elements in adaptive façades.

Passive system	Use location	Stimulus	Benefits for sunshade design	Limitations for sunshade design
PCM	Glazing [33], [54] Insulation [23], [52], [60], [88] Other [50], [74]	Heat	High thermal energy storage [33], [54]	Cost [60], [54] High embodied energy [60] Unever release of heat [33] Careful control of transition temperature [33], [54], [88] Large amount needed [88] Stimulus and response might not be related [27]
Wood	Lamellaes [27], [37] Double skin [56]	Humidity	Achieves dynamicity [37]	Small openings can lead to low acceptance [37]
Thermochromic	Glazing [13], [22], [29], [38], [47], [94]	Heat	Can reduce solar gains in summer while allowing them in winter [13], [22], [29], [38], [47], [] Transparency allows for a continuous view	Color [13], [47] Stability [13], [29] Toxicity [13] Hard to configure [13] Cost [29]

Passive system	Use location	Stimulus	Benefits for sunshade design	Limitations for sunshade design
SMA	Actuators [23], [32], [44], [52], [76], [78], [93], [94]	Heat	Low cost [32], [76], [78] Biocompatible [32], [76] Corrosion resistance [76] Simple to use [76] Lightweight [32], [76] Silent operations [32], [76] Electricity override [44]	Long cycle time [76] Temperature hysteresis [76] Low deformability [76]
SMP	Actuators [32], [78] Sunshading cells [95], [96]	Heat	Low cost [32], [78] Biocompatible [32], [78] High deformability [32], [78] Simple to use and produce [78] Silent operation	Sensible to UV corrosion [78] Stiffer at lower temperature makes it hard for reversible transformation to take place [95], [96]

2.2.1 PHASE CHANGE MATERIALS

Phase Change Materials (PCMs) are systems that are systems able to take advantage of the latent heat stored during the transition between the solid and liquid phases. The PCM melts at high temperatures, allowing for latent heat storage. The thermal energy is then released, and the ambient temperature rises when the outside temperature falls below a particular level (Lelieveld, 2013).

In recent research, Mohtashami et al. (2022) conducted a comprehensive review of technologies used in Adaptive Dynamic Building Envelopes (ADBEs). They classified Phase Change Materials (PCMs) and sunshades as non-active technologies. While PCMs were recognized for their advanced energy storage capabilities, their drawbacks included high costs, embodied energy, and limited usage. In contrast, sunshades were considered cost-effective but applicable primarily to windows.

In the quest to enhance the thermal performance of buildings, Goia et al. (2014) examined the integration of PCMs into glazing systems. They found that this approach showed promise for better summer performance but emphasized the need for fine-tuning transition temperatures and PCM mass. However, a significant portion of stored heat was observed to dissipate outdoors, particularly in cold weather.

Li et al. (2022) delved into the integration of PCMs within glazing envelopes, highlighting that most research tends to focus on enhancing either solar light or heat transmission, potentially leading to poor climate adaptation. They pointed out that insufficient heat transmission could disrupt the phase change process, resulting in inadequate lighting and reduced heat absorption capacity. Economic sustainability of these systems was also questioned.

In a review of free cooling systems using PCMs, Waqas and Din (2013) noted the potential advantages over traditional cooling methods but identified several challenges. These included partial solidification of PCMs within specified timeframes, low heat conductivity, and issues related to material quantity, which could be substantial for buildings.

Efforts to integrate PCMs into roofs (Kumar, 2022) and wind catchers (Seidabadi et al., 2019) have been explored. However, these studies are in preliminary stages and do not comprehensively address the limitations associated with PCM applications in these contexts.

Lastly, Cui (2020) reviewed passive switchable insulation systems, covering Mechanical Contact Switchable Insulation employing PCMs or Shape Memory Alloys (SMAs) and Phase-Change Switchable Insulation using non-condensable gas technology. These approaches offer potential solutions for enhancing building energy efficiency.

Figure 2.1a-b shows an example of PCMs and their applicability to glazing.

a b

Figure 2.1 a) Paraffin wax is one of the most commonly used PCMs (Wikimedia, 2023); b) PCMs installed inside double-glazed windows. (Building Green, 2023)

2.2.2 CHROMIC GLAZING

Another way to apply smart materials is in systems for adaptive glazing. Photo-chromic and thermo-chromic glazings are identified as strategies to improve user comfort while lowering energy consumption (Lelieveld, 2013). The formers change their transparency when stimulated by light, while the latter do so when the stimulus is temperature.

Current difficulties with VO2-based thermochromic glazing have been identified to be: balance between transition temperature, visible transmittance, and solar modulation ability, color achieved with the system, stability, which threatens durability, and toxicity (Cao et al. (2020); Cui et al.(2018)) as well as photodegradation and high cost of production (Fabiani & Pisello, 2021). The application of these technologies has been studied in double skin façades (Iken et al., 2019), colorful windows (Ke, et al., 2022), and in combination with Shape Memory Materials (SMMs) (Yoon, 2018).

Figure 2.2 represents the contrast between active and inactive states of thermochromic glazing. On the right side of the image, the thermochromic glazing is depicted in its darkened, activated state, which occurs in response to specific environmental conditions. In contrast, the left side shows the glazing in its clear and inactive state, highlighting the dynamic transformation these materials undergo based on external factors.

Figure 2.2 Active and inactive state of thermochromic glazing. (View, 2023)

2.2.3 HYGROSCOPIC PROPERTIES OF WOOD

Other attempts have been made to exploit different technologies and material properties, such as those of wood. Ibrahim et al. (2020) extended the passive actuation of adaptive systems based on these technologies to climates with high humidity and/or temperature fluctuations. Their findings demonstrate how when compared to mechanically actuated systems, programming the material can result in a simpler solution, saving energy and time. These adaptive systems find applications in sunshade designs, where apertures automatically close in response to specific humidity and temperature thresholds.

However, because many small apertures are introduced in the field of view, the systems appear daunting, and user acceptance research should be conducted. The hygroscopy of wood has also been used to achieve the hygrothermal comfort of a building through

retrofit strategies (López-Escamilla, et al., 2022). However, the study only focuses on the various possibilities for placing the double-skin retrofit but does not address its limitations. Figure 2.3 shows an example of a prototype that exploits the hygroscopic properties of wood.

Figure 2.3 Wood lamellae in HygroSkin prototype. (Adsttc, 2023)

2.2.4 SHAPE MEMORY MATERIALS (SMMS)

Juaristi et al. (2018) conducted a qualitative analysis of different auto-reactive materials for opaque façades where Shape Memory Materials scored the best overall in the categories analyzed. These were: adaptability range, velocity of adaptation, user control (overriding possibility), auto-reactiveness, and system decentralization.

Fiorito et al. (2016) propose using stimulus-responsive materials (SRMs) as sensors and actuators in adaptive shading designs. Between these, we can identify three alternatives: Shape Memory Alloys (SMAs) (figure 2.4a), Shape Memory Polymers (SMPs) (figure 2.4b), and Shape Memory Hybrids (SMHs) (Sun, et al., 2012).

Despite their advantages and disadvantages, there is a significant difference in the shape memory effect the different groups have. Upon heating up, all SRMs

"remember" a shape or configuration, but how they do this differs significantly. SMAs are used thanks to the reversible martensitic transition, which allows the metal to be bent at temperatures lower than its activation temperature and then restored when heated (figure 2.5).

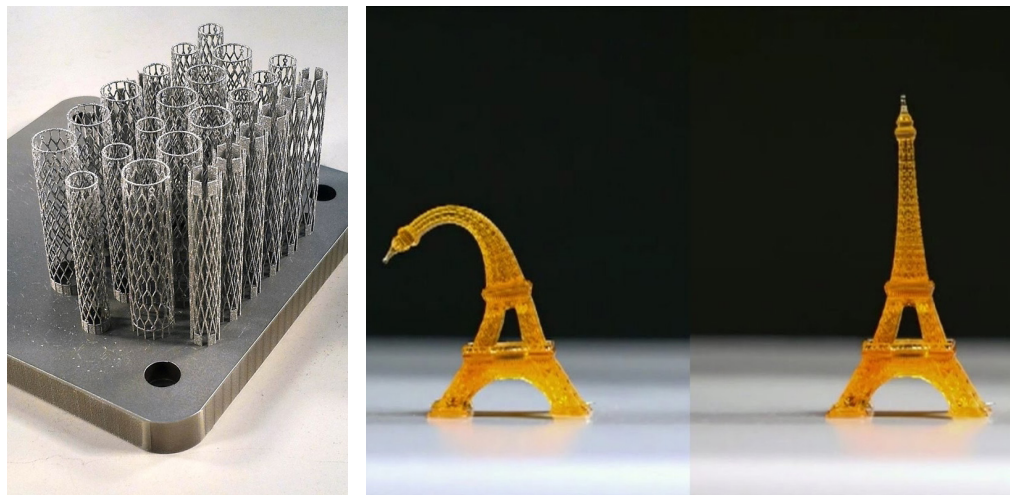

a b

Figure 2.4 a) SMAs used for cardiovascular stents in the biomedical field (Cloudfront, 2023); b) Example of SMPs recovery. (Sculpteo, 2023)

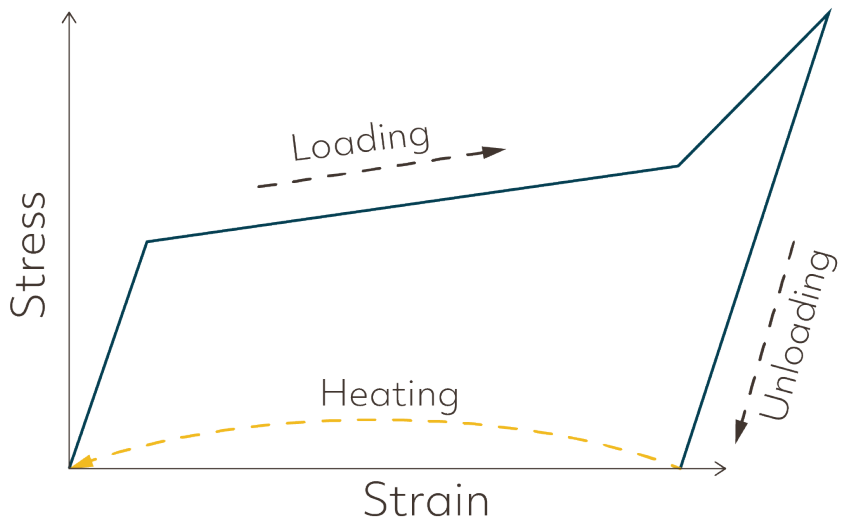

Figure 2.5 Shape memory effect in SMAs. The plastic strain remained after the unloading is recovered through the heating of the alloy. (adapted from Sun et al. (2012))

SMPs and SMHs, on the other hand, can be deformed above the activation temperature and become stiffer below it. Once heated, the substance returns to its original shape. This fundamental distinction is evident in figure 2.6, where the stiffness as a function of temperature is compared. Due to this distinction, SMA is more suited for adaptive sunshades since the triggering action (such as solar radiation) heats the material and activates its shape memory effect by raising the stiffness and stress upon recovery.

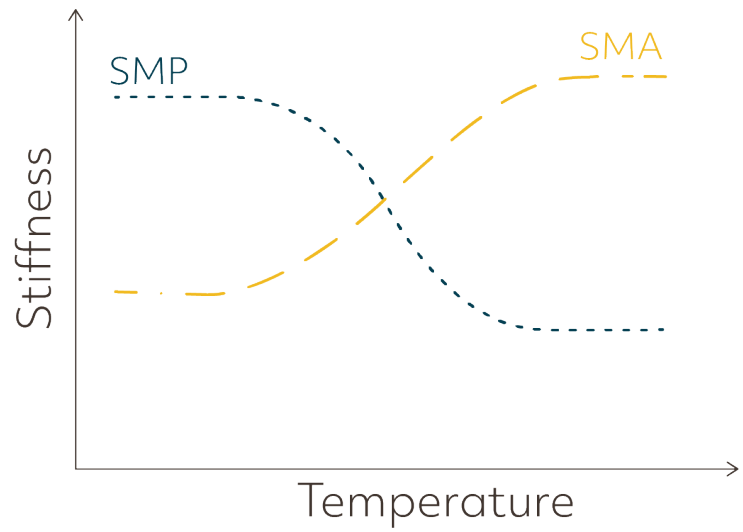

Figure 2.6 Change of stiffness in thermo-responsive SMMs upon heating. (adapted from Sun et al. (2012))

Soother et al. (2020) examined the difficulties of employing SMA-based actuators. According to the study, this technology has been widely used due to the low cost, biocompatibility, flexibility, high corrosion resistance, and simplicity of use of the material. Furthermore, the light weight results in a high force-weight ratio, which results in silent operation and components that can absorb unexpected axial forces. The authors acknowledge these materials' limits regarding absolute force and the long cycle time to heat up and cool down. Another concern is the difference in activation temperature between the heating and cooling phases, which causes temperature hysteresis that is difficult to control. In a study comparing SMA actuators and Artificial-intelligence (AI) kinetic control, Yi & Kim (2021) found that the former could replace the latter. However, indoor building conditions must be carefully considered since the response time is not instantaneous.

SMPs have been studied as possible sunshade designs as simple circular cells (Yoon, (2019); Yoon & Bae, (2020)), but the authors report the instability of the SMP during manufacturing and operation as well as more studies on the reversible movement, which has not been solved.

2.2.5 STUDIES THAT INCLUDE OTHER SOLUTIONS

Together with the hygroscopic properties of wood lamellae, El Houda & Mohamed (2018) also identify thermo-bimetal, a metal composed of two metals with different expansion coefficients, and thermo/photo-chromatic ink, which becomes lighter during hot days and dark during cold one, as possible passive adaptive strategies.

In their review of smart materials for possible façade application, Juaristi et al. (2018) identify both active and passive technologies. Between the last ones, the study identifies thermochromic, photochromic, and thermotropic glazings as technologies whose color could be difficult to apply in the urban context, and thermobimetals, heat-sensitive plastics, Shape Memory Materials, CO2-responsive Polymers, and hydrogel actuators. These last ones are said to be impossible to override, and their possible façade performance was not yet explored. However, Ji et al. (2022) studied a passive cooling fabric inspired by skin sweating designed by the deposition of a thermoresponsive hydrogel on cotton, showing promising results for developing passive cooling materials designs.

From this, it can be concluded that SMAs hold great promise to be part of a passive sunshade as their drawbacks do not threaten the former's functioning. The low deformability can be solved by implementing a series of springs, while the long cycle time does not create a problem as the response does not have to be immediate for thermal purposes in facades. Thermal hysteresis depends on the composition of the material and will be addressed in a later section.

2.3 FUNCTIONING OF SHAPE MEMORY ALLOYS

Shape Memory Alloys are popular materials because of their unique shape memory effect (SME) and superelasticity (SE). In the first phenomenon, the metal can restore its shape at a specific temperature, known as the activation temperature; in the

second, the alloy can be bent or stretched to a larger extent that normally elastic metals before returning to its original shape when unloaded. Both behaviors are caused by a process known as martensitic transformation (figure 2.7).

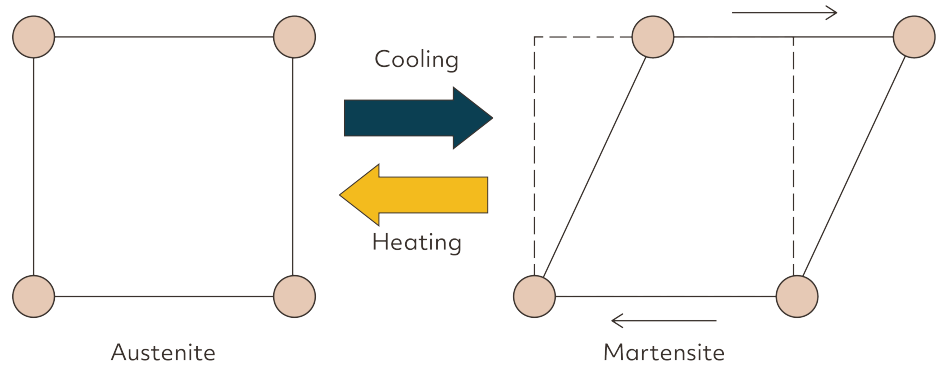

Figure 2.7 Schematic illustration of change in unit cell shape during martensitic transformation. The atoms shift into the martensitic phase which has lower crystallographic symmetry. (Adapted from Yamauchi et al., 2011)

The crystal structure changes into a phase with decreased crystallographic symmetry after being cooled below the martensitic transformation temperatures from the high-temperature phase. The austenitic phase, is the high-temperature phase, while the martensitic phase, also known as martensite, is the result of the martensitic transformation. This transition takes place within a particular range of temperatures. Four transformation temperatures are usually considered valuable: martensitic transformation start temperature (Ms), martensitic transformation finish temperature (Mf), reverse transformation start temperature (As) and reverse transformation finish temperature (Af). These are shown in figure 2.8

The material can be easily bent because the martensite phase is easily deformed by twinning. When the bent material is heated above Af, the martensite changes back to austenite, and the sample returns to its original shape. When the metal is cooled below the martensitic transformation temperature or heated above the reverse transformation temperature, the shear modulus of the SMA changes. The latter is significantly higher in the high-temperature phase (austenite) than in the low-temperature phase (martensite). In Ti-Ni alloys, for example, the shear modulus of the martensite phase is around 8000 MPa, whereas that of the parent phase surpasses 20000 MPa. (Yamauchi, et al., 2011)

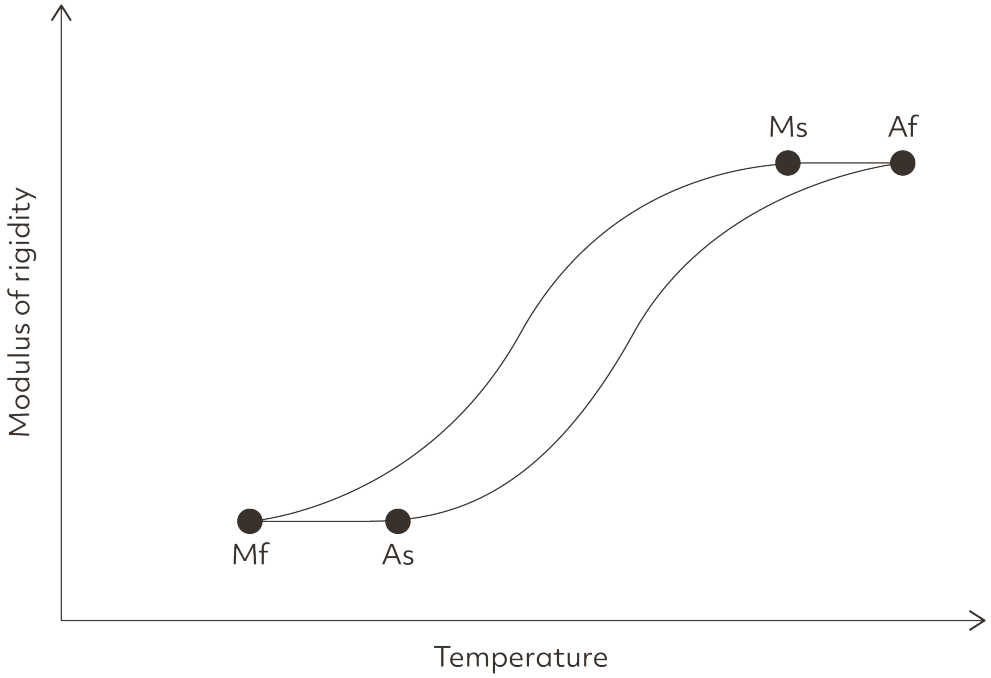

Figure 2.8 Dependence of the modulus of rigidity of SMA to the four transformation temperatures. (Adapted from Yamauchi et al., 2011)

Other possible compositions have different activation temperatures and mechanical properties. Table 2.2 lists these ranges and their range of operating temperatures.

Table 2.2 Comparison of operational temperatures and thermal hysteresis of studied composition of shape memory alloys. (adapted from (Yamauchi, et al., 2011))

Material	Use temperature [°C]	Thermal hysteresis [°C]
TiNi-Fe, Co, Cr	[-20, 40]	2-3
TiNi	[20, 80]	2-3
TiNi-Cu	[40, 100]	10-15
Ti-Nb	[-80, 220]	-

Furthermore, controlling the transition temperature poses challenges. Even a minor 0.1% variation in composition can lead to a significant shift in transition temperature, approximately 10°C for TiNi alloys and up to 40°C for Ti-Nb alloys (Yamauchi et al., 2011). Commercially available SMAs often come in discrete steps of approximately 5°C, spanning the range from 17°C to 35°C, as observed in products from Kellogg's Research Labs (2023) and PeierTech (2016).

According to Yamauchi et al. (2011), using springs could be implemented to address the SMA's minor contraction state. The primary benefit of such a shape is the large stroke that this design can achieve compared to a simple wire (figure 2.9). The graphic depicts how the two bodies respond to a 1.0% strain. As a result, the actuator can move farther when in the shape of a spring without getting bigger in the axial direction.

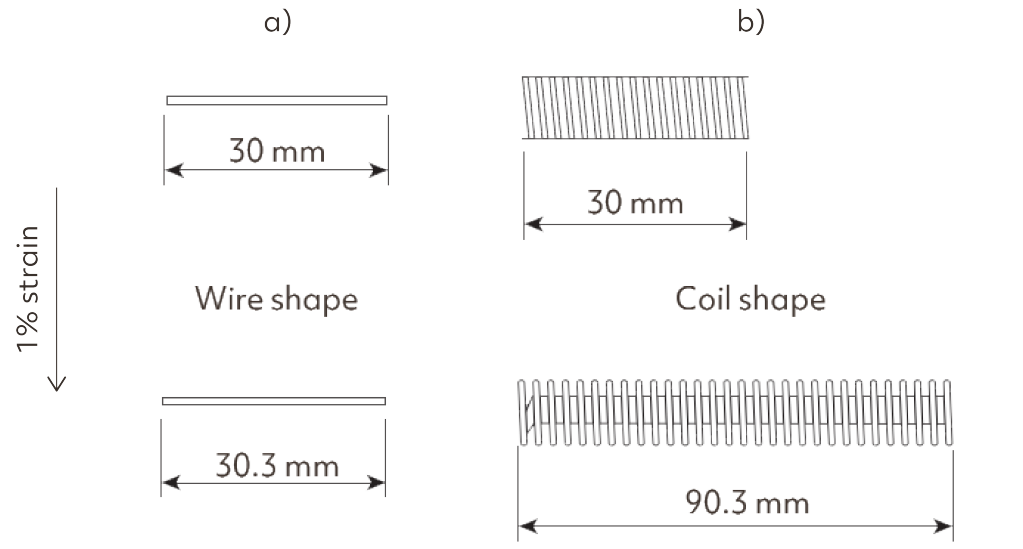

Figure 2.9 Comparison of strokes of SMAs between a) Wire shape and b) Coil shape.For a 1% strain recovery the coil is able to recover more stroke than the wire. (Yamauchi, et al., 2011)

Sun et al. (2012) also demonstrate the many actuator types that can be used with SMA. These comprehend one that recovers its initial condition with the help of an external force (figure 2.10.A). Other possibilities include using a spring to return the system to the unsolicited state (figure 2.10.B) or another SMA at a different activation temperature (figure 2.10.C).

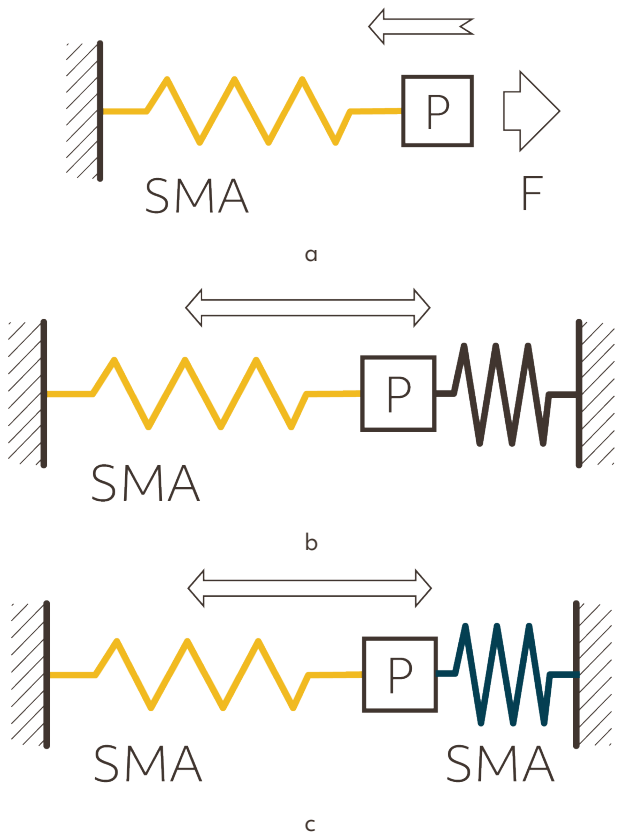

Figure 2.10 Three basic types of SMA actuators. a) One-way actuator, where the force counteracts the SMA which is going to bring the system back to its original state; b) biased actuator, where the spring counteracts the SMA and the system switches between two states; c) two-way actuator; where two different SMAs make the system switch between different states. (Adapted from (Sun, et al., 2012))

2.4 CURRENT SMA-BASED SUNSHADE DESIGNS

Current SMA-based sunshade designs found in literature are summarized in table 2.3, along with the developments made towards their implementation and their drawbacks. After this, each solution is analyzed individually in an effort to identify the gap present within this field.

In this table, "secondary spring" refers to a secondary mechanical spring that counteracts the SMA when in its martensitic state. The mechanical analogy is depicted in figure 2.10B.

Table 2.3 Characteristics of the SMA-based designs found in literature. Applicability potential and counteracting force.

Design reference	Advantages	Limitations	Counteracting Force
(Pesenti, et al., 2018)	Origami shapes increases otherwise limited movement	Occupies field of view constantly Only proof of work built	Secondary spring
(Mansourizadeh, et al., 2021)	Has the ability to open fully	Complex mechanical system	Secondary spring
(Kim, et al., 2023)	Built prototype	Occupies field of view constantly Complex mechanical system	Secondary spring
(Grinham, et al., 2014)	Built full scale	Occupies field of view constantly Complex mechanical system	Secondary spring
(Yi, et al., 2020)	Easily deployable	Occupies field of view constantly Still relies on current	Secondary spring
(Vercesi, et al., 2020)	Black box patent	Occupies field of view constantly Complex mechanical system	Secondary spring
(Denz, et al., 2021) Wave	Built full scale	Occupies field of view constantly Complex mechanical system	Tension
(Denz, et al., 2021) Mesh	Built full scale	Occupies field of view constantly Complex mechanical system	Weight
(Ingpuls, et al., 2022)	Product in the market Simple to use	Relies on external force No specifications given	Secondary spring

Pesenti et al. (2018) present the use of SMAs as sensors and actuators in a design based on the Japanese art of Origami. The difficulty posed by the SMA's limited contraction state inspired this design, as origami shapes can intensify the otherwise limited movement thanks to their geometric properties. Yet, due to its complicated geometrical features, the proposed design still seems difficult to maintain during the façade's lifetime (figure 2.11).

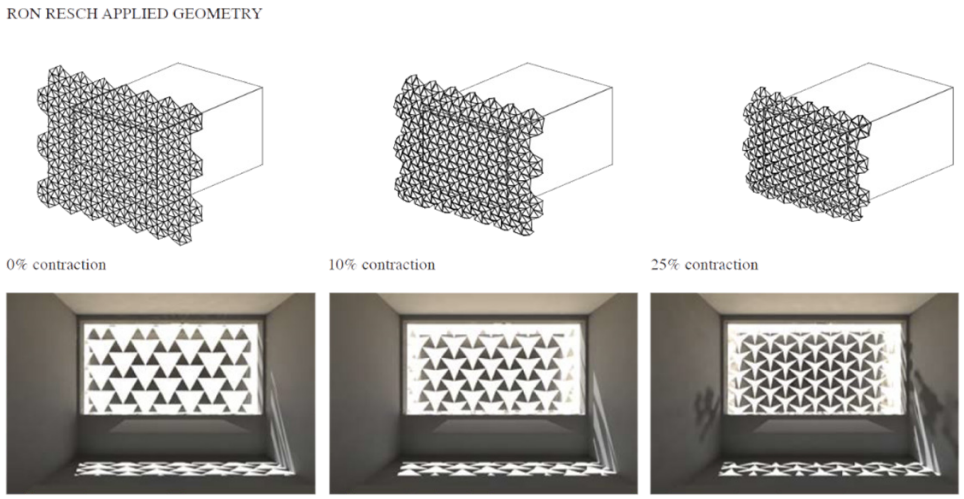

Figure 2.11 Axonometric view and perspective view from the interior of RRA100B0 shading for the three contraction states. (Pesenti, et al., 2018)

On the other hand, another factor to consider is the sunshade's architectural impact on the façade. The sunshade in the proposed design ultimately dictates the outer façade's aesthetic, making it less appealing to architects who might want a different aesthetic. The interior view is another aspect of the design that stands out clearly, and it should be investigated to comprehend how the occupants respond to the many small apertures.

Mansourizadeh et al. (2021) developed a novel shading mechanical system activated by Nitinol springs that get triggered by absorbing the sun's energy. While the mathematical model developed can be used to size the spring, the design still looks intricate, with numerous components and moving parts (figure 2.12).

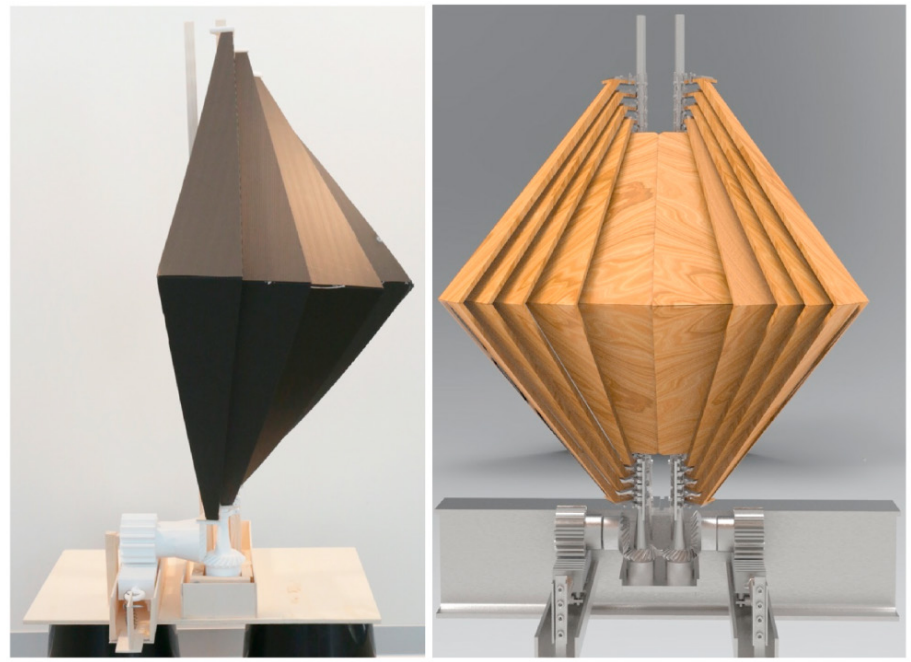

Figure 2.12 Fully closed state of the mechanical system. (Mansourizadeh, et al., 2021)

Kim et al. (2023) studied an adaptive shading façade module by combining pneumatic elastomer and SMA actuators. While they achieved shape-changing capabilities and structural stability, the design's maximum opening area is still limited to approximately 20% (figure 2.13).

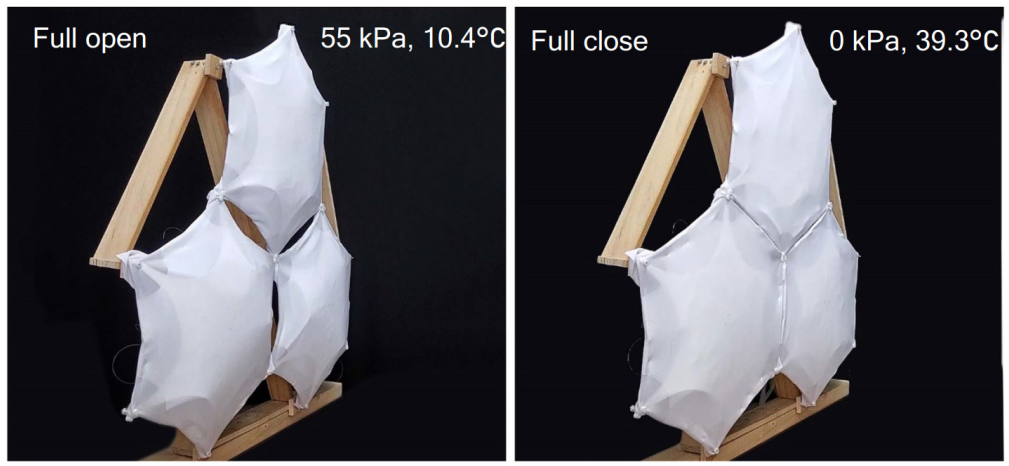

Figure 2.13 Building scale prototype model. (Kim, et al., 2023)

Grinham et al. (2014) developed a kinetic shading device similar to that of sunblinds. The system, however, has been only tested generally as a proof-of-concept, and it has to be constantly in front of the window, occupying the field of view at all times (figure 2.14).

Figure 2.14 States of the system developed. (Grinham, et al., 2014)

Yi et al. (2020) designed a user-fabricable 3D-printed kinetic shading device that is actuatable by a geared DC motor or an SMA actuator. The prototype demonstrated the solutions' effectiveness in controlling room temperature. Still, the authors recognize the limitations regarding the difficulty of fabrication and the complete automation of the design with the sole SMA actuator. Furthermore, the design still presents limited movements (Figure 2.15).

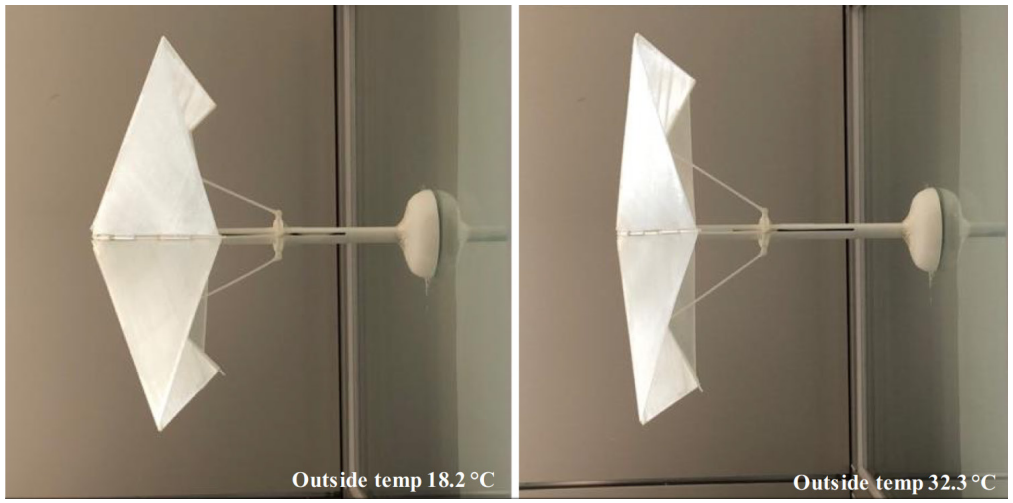

Figure 2.15 Stroke of the system. (Yi, et al., 2020)

Vercesi et al. (2020) patented a design based on an SMA spring inside a black box connected to a system (figure 2.16) that rotates shades (figure 2.17). Concerns can be raised about the degree to which the patented system simplifies things. The cost and complexity of system maintenance might dramatically rise with such a design and small parts. The user's approval of this system should also be carefully examined as it introduces unique geometries into the field of view.

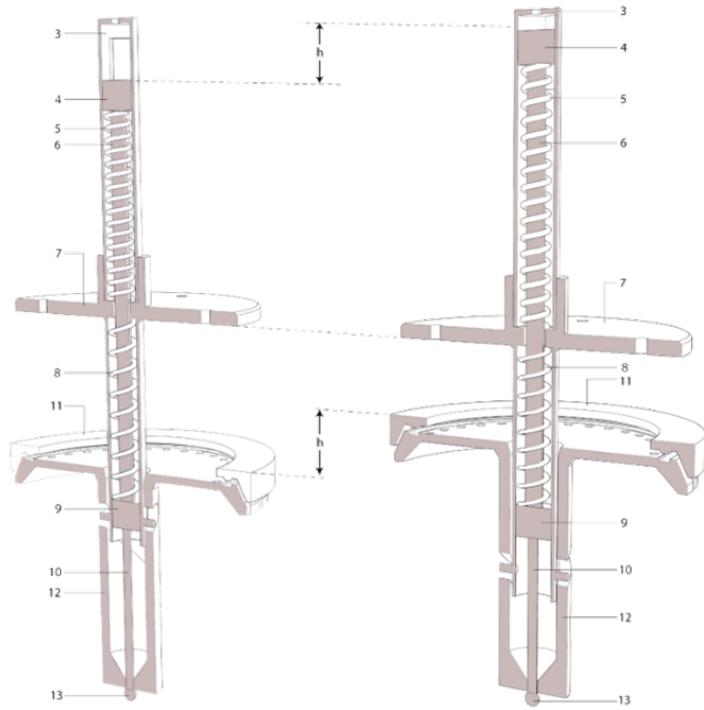

Figure 2.16 The top connection detail "PATENT WP2018116102-A1." (Vercesi, et al., 2020)

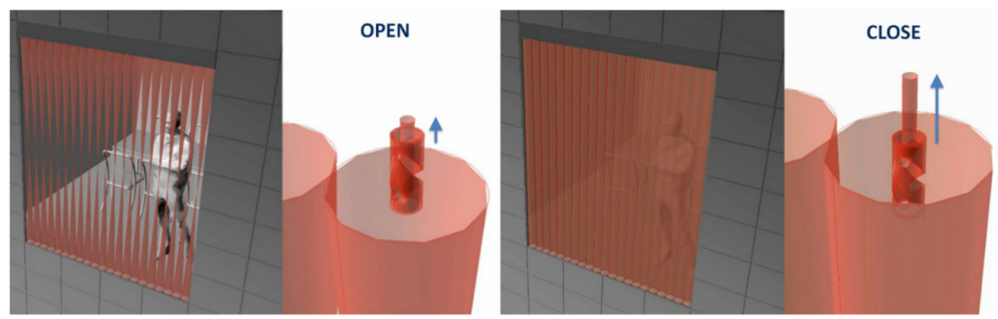

Figure 2.17 System conceptual appearance in open and closed state. (Vercesi, et al., 2020)

It is also possible to return the system to its initial state without employing a spring. To specify all conceivable combinations of designs, Denz et al. (2021) presented a matrix with all possible combinations and developed two for additional testing and modeling. These two methods used the internal tension of the lamellas and weight of the textile, ADAPTEX Wave (figure 2.18a) and ADAPTEX Mesh (figure 2.18b), respectively, to restore the SMA to its original shape. The issues of costs and complexity have yet to be fully resolved, although the systems appear promising and have been tested on both small and real-scale models. In contrast to ADAPTEX Mesh, which blocks the outside view and complicates the design in terms of maintenance, ADAPTEX Wave has many parts and seems moderately susceptible to weather conditions.

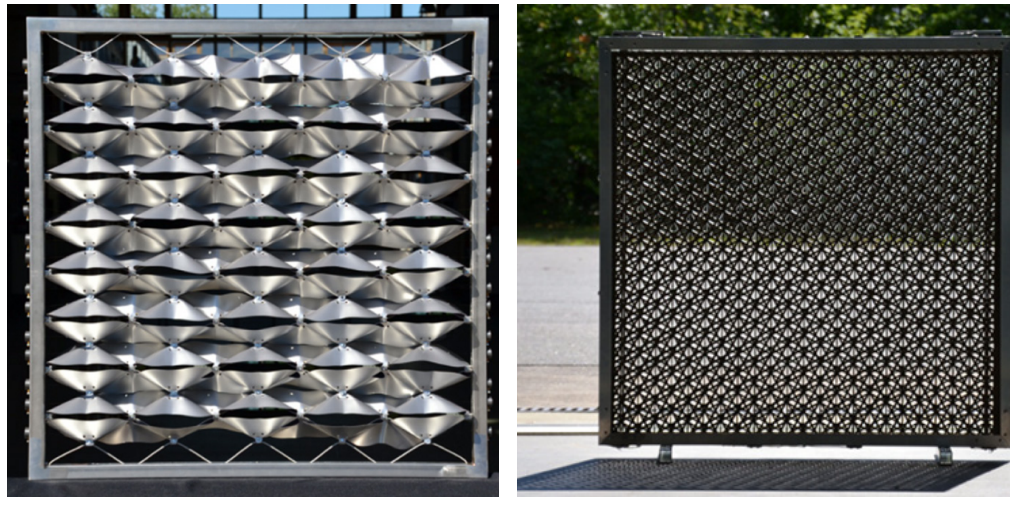

a b

Figure 2.18 a) Demonstrator of ADAPTEX wave within a constructional frame. b) Demonstrator of ADAPTEX mesh within a constructional frame. (Denz, et al., 2021)

On the market, a solution using SMAs and textiles is already present (Ingpuls, 2022). Many benefits, such as quiet operation, low cost, no electric motor, and easy installation, are mentioned, but no specifications are given.

All the designs presented are composed of smaller components to compensate for their limited stroke and/or have intricate mechanical designs or secondary springs to counteract the SMA. The ones using smaller parts always interfere with the users' field of view. In contrast, the ones counteracted by mechanical systems do not fully exploit the benefits of SMAs to reduce the mechanical complexity of the designs. Only the designs from ADAPTEX use other types of force. Namely, ADAPTEX Wave

counteracts the cold SMA with the tension built in the lamellas and ADAPTEX Mesh with the weight of the hanging textile.

2.5 TEXTILE AS A BIASING SUN SHADING MEMBER

In literature, examples have not been found using textiles as biasing members. The reason for these materials to be possible candidates as biasing members for an SMA actuator resides in their nature. Specifically, these materials can hold tension, thereby the force able to counteract the SMA spring while stretching considerably, enabling the system to have a large stroke, not covering the field of view at all times.

Tensioned textiles have been used as sun protection devices in a wide range of applications, such as awnings, canopies, roller blinds, and tensile structures (figure 2.19a-d). These can be manufactured by weaving, braiding, knitting, and non-weaving (Fangueiro & Soutinho, 2016).

a

b

c

d

Figure 2.19 a) Awning for sun protection mechanically activated (Markilux, 2023); b) Tensed canopy used as protection against the sun (Base Structures, 2023); c) Close up of a roller blind (Umbra Shading, 2023); d) Tensile structure creating shade (Panjetani Build Well, 2023).

2.6 CONCLUSIONS

Amongst passive strategies, Shape Memory Alloys are the ones that present the most benefits when it comes to sunshade design. This is thanks to their low cost, non-toxicity, corrosion resistance, and mechanical behavior. The latter is based on the martensitic transformation process, which makes the metal go from a malleable martensitic phase to a rigid austenitic phase that “remembers” a shape.

Although these materials promise to deliver adaptability and simplify the mechanical complexity of designs, current solutions are still comprised of many small components that interact with each other. This represents a threat to the lifespan of the system. Furthermore, most proposed designs always occupy the field of view, never allowing for an unobstructed view of the outside.

Finally, most SMA-based systems rely on a secondary spring as a biasing member, making it difficult for the designs to get simpler with fewer components. Textiles have the potential to solve these issues due to their ability to hold tension and deform significantly. However, no examples are currently present, and the mechanical and building physics aspects of such a system must be investigated.

METHODOLOGY

This chapter presents the overall methodology used to answer the research questions in chapter 1.3.

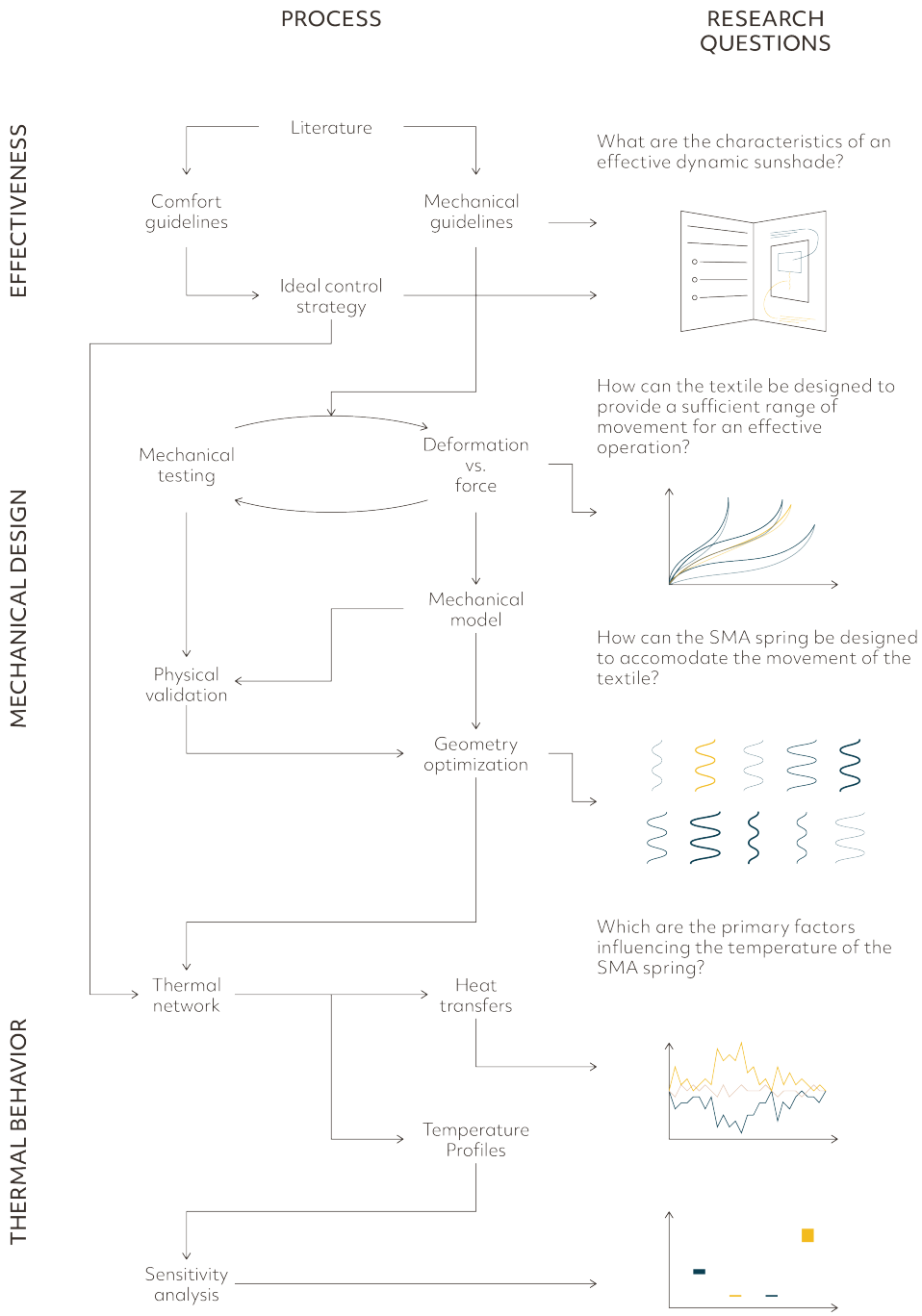

Figure 3.1 Scheme of the overall methodology adopted in this thesis.

Figure 3.1 shows the workflow adopted in this thesis.

To define what makes a dynamic sunshade effective, a short review of the functions that these systems need to have has been carried out. These were divided into two categories. The first concerned thermal and visual comfort guidelines, while the second concerned mechanical guidelines (i.e., complexity and system's dynamicity). From the comfort guidelines, it was possible to define an ideal control strategy using a case study in a Grasshopper script.

The mechanical guidelines helped with the definition of the mechanical design. The latter results from an iterative process of producing and testing specimens thanks to CNC (Computerized Numerical Control) knitting. From each specimen, force-deformation curves were constructed. These helped with the next iteration of specimens and with the construction of the final mechanical model.

The mechanical model was an analytical tool to validate the constructed physical model. This made optimizing the spring geometry for a given textile possible.

A nodal thermal network was built, given the optimized geometry and the ideal control strategy from the first part. From this, it was possible to get the heat transfers involved with the SMA spring and the temperature profiles of every system component.

The latter helped to conclude the work with a sensitivity analysis of the main design parameters of the system on the temperature reached by the SMA spring.

EFFECTIVENESS

This chapter deals with the first sub-research question:

"What are the characteristics of an effective dynamic sunshade?"

To define what an effective design is, this chapter is divided into four sections. Section 1 deals with typical sunshade requirements for the indoor climate. Section 2 describes an ideal control strategy for visual and thermal comfort. Section 3 defines benchmarks for the mechanical system. Finally, section 4 summarizes the results and defines "effective."

4.1 EFFECTIVENESS OF SHADINGS AS WELL-SUITED MULTI-DOMAIN ENVIRONMENTAL PERFOMANCE

During our life, we spend around 90% of our time indoors (European Commission, (2003), United States Environmental Protection Agency, (2021)). As a result, maintaining proper Indoor Environmental Quality has become essential. The latter can be divided into four main categories: thermal comfort, luminous quality, air quality, and acoustic quality (CIBSE, 2022).

While façades influence all these aspects as they are the barrier between the outdoor and the indoor environment (Boswell, 2013), a solar control device, e.g., a sunshade, mainly influences the first two. In particular, different criteria have been identified as relevant for evaluating solar-control systems (Kuhn, 2017). The ones for the indoor environment have been summarized in figure 4.1.

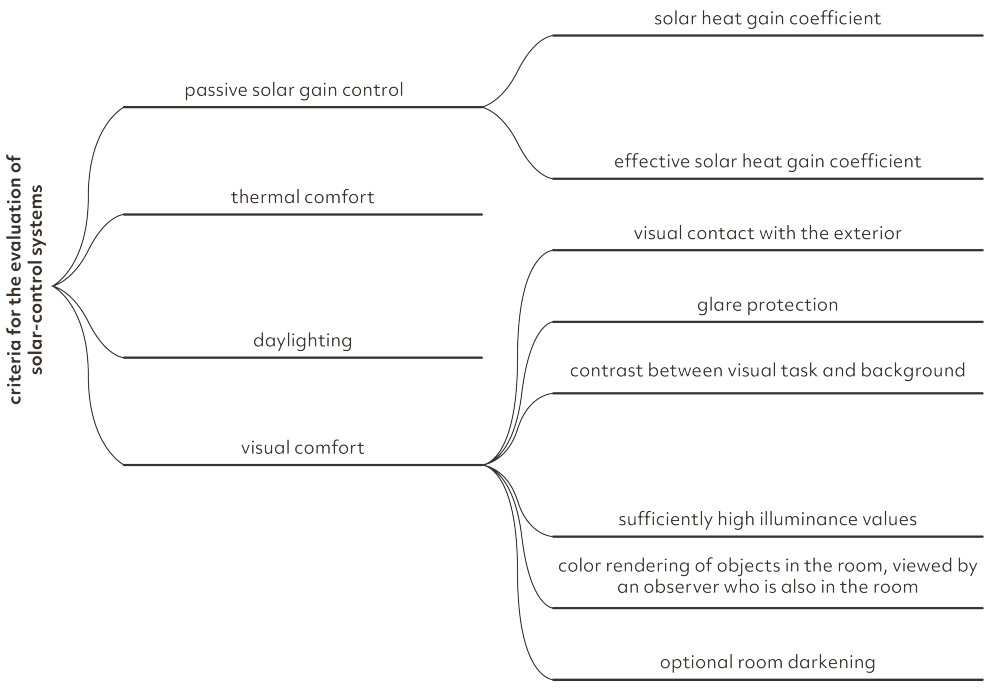

Figure 4.1 Performance evaluation criteria for solar-control systems (Adapted from (Kuhn, 2017)).

It can be noted that there are numerous requirements a sunshade can have. This work aims to develop a system that can reduce the energy demand while maintaining the field of view unobstructed when inactive. Therefore, this work will be focused on maintaining thermal comfort and visual contact with the exterior.

The definition of thermal comfort is given by NEN-EN-ISO 7730 (2005):

"that condition of mind which expresses satisfaction with the thermal environment."

The same norm specifies three thermal environments (A, B, and C) in increasing Predicted Percentage Dissatisfied (PPD). The latter is a quantitative prediction of the percentage of thermally unsatisfied users who are either too cold or too warm. The operative temperature is used to comply with one of the specific thermal environment and is used as an indicator of thermal quality. The operative temperature is a weighted average between air temperature and internal mean radiant temperature and it is governed by the formula (NEN-EN-ISO 52017-1, 2017):

(eq. 4.1)

$$\theta_{int;op} = f_a \cdot \theta_{int;a} + (1 - f_a) \cdot \theta_{int;mr}$$

Where:

$\theta_{int;op}$ is the operative temperature [°C];

f_a is the fraction that the air temperature contributes to the operative temperature [-];

$\theta_{int;a}$ is the temperature of the internal air [°C];

$\theta_{int;mr}$ is the mean radiant temperature, which is the weighted average of the internal surface temperatures [°C].

The acceptable operative temperature interval depends on environmental conditions (e.g. air speed and relative humidity) and on the occupants (e.g. metabolic rate and clothing insulation) of a particular space. Figure 4.2 shows the intervals for a standard office.

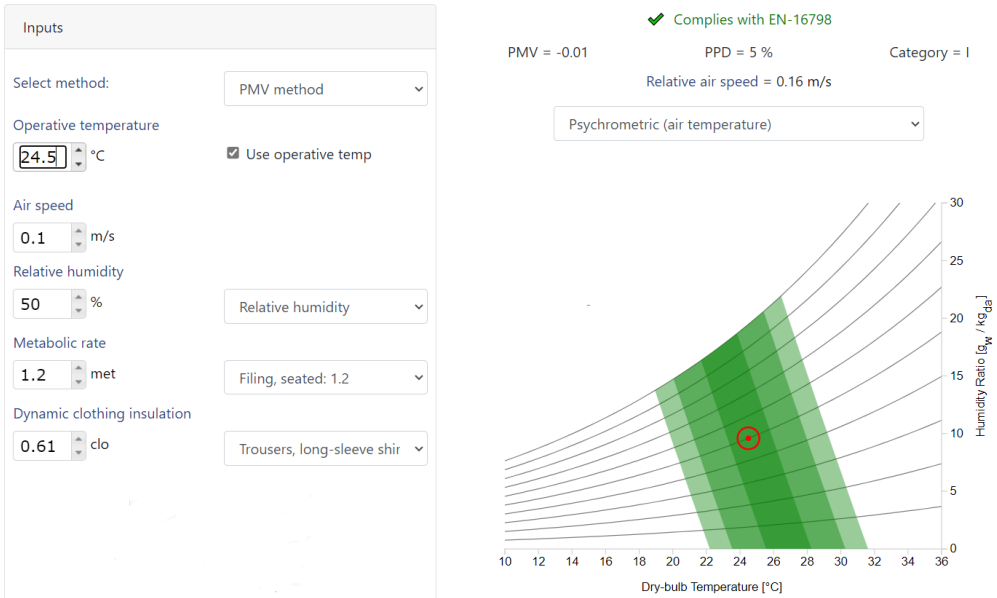

Figure 4.2 Input parameters and comfort range for a typical office. (Tartarini, et al., 2020)

To limit operative temperature, solar gains have to be restricted. Thermal comfort is affected by the presence of sunshades in three ways:

- operative temperature get influenced by the solar gains, which depend mainly on window size and total solar energy transmittance g_{tot};
- higher local values of $\theta_{int;op}$ are probable due to direct sun exposure on the inner surface of the glazing or of the sunshade. To quantify this effect, the secondary internal heat transfer factor $q_{i,tot}$ is used;
- people or surroundings can be prevented from being irradiated directly. This is quantified by the direct-direct solar transmittance $\tau_{e,n\text{-}n}$. (NEN-EN 14501, 2021)

To quantify the effect of the solar protection device, performance classes are defined based on these three parameters (Table 4.1).

It is possible to calculate these quantities knowing the properties of the solar protection device and the glazing to which it is applied.

Kuhn (2017) points out that no generally accepted metric quantifies visual contact with the exterior. However, the author concludes that such metrics should consider the view area and image quality. The latter can be influenced by color rendering,

sharpness, and reducing the disturbance of contrast by haze (e.g. when white fabrics scatter light).

Table 4.1 Classification of sunshades based on influence on thermal comfort. (adapted from (NEN-EN 14501, 2021))

Class	Influence on thermal comfort				
	0	1	2	3	4
	Very little effect	Little effect	Moderate effect	Good effect	Very good effect
g_{tot}	g_{tot} ≥0,50	0,35≤g_{tot}<0,50	0,15≤g_{tot}<0,35	0,10≤g_{tot}<0,15	g_{tot}<0,10
$q_{i,tot}$	$q_{i,tot}$ ≥0,30	0,20≤$q_{i,tot}$<0,30	0,10≤$q_{i,tot}$<0,20	0,03≤$q_{i,tot}$<0,10	$q_{i,tot}$<0,03
$\tau_{e,n\text{-}n}$	$\tau_{e,n\text{-}n}$ ≥0,20	0,15≤$\tau_{e,n\text{-}n}$<0,20	0,10≤$\tau_{e,n\text{-}n}$<0,15	0,05≤$\tau_{e,n\text{-}n}$<0,10	$\tau_{e,n\text{-}n}$<0,05

4.2 IDEAL CONTROL STRATEGY

Defining a unique ideal control strategy for all the world's buildings is impossible. This is because of different climatic requirements, geometries, room parameters, and functions. For this reason, a case study was built and tested to check for the ideal control strategy in a typical office geometry in Rotterdam, NL.

4.2.1 METHODOLOGY

The case study was built in Grasshopper, simulated with Honeybee and EnergyPlus, and the results were postprocessed with MATLAB. The office followed the geometry of the BESTEST room described in ANSI/ASHRAE (2007), illustrated in figure 4.3. The analysis period was set to the three months of June, July and August, taken as the period where cooling is most necessary.

The walls, ceiling, and roofs were modeled as adiabatic surfaces as an assumption of adjacent rooms at the same temperature. The opaque part of the South façade was modeled with an R-Value of 4.7 m2K/W. Double glazing was assumed for the window, and the properties were taken from Guardian Glass (2023), summed in table 4.2.

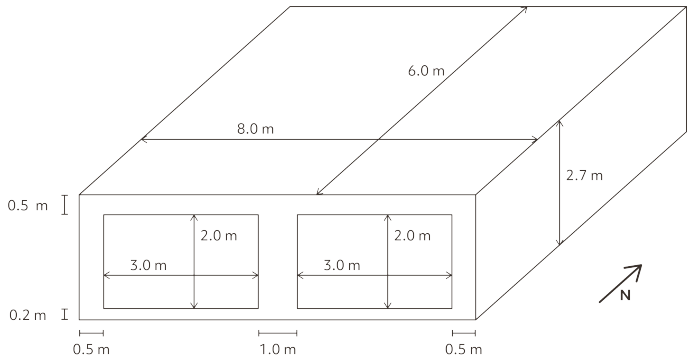

Figure 4.3 BESTEST room case geometry.

Table 4.2 Properties of the glazing for the simulation

Property	Value	Unit
U-Value	2.8	W/m^2K
Solar heat gain coefficient	0.77	-
Visible transmittance	0.819	-

Knowing the material used for the blind, it was possible to derive some properties (i.e., thickness, conductivity, permeability, distance from glazing). For the solar transmittance, a value of 0.05 was assumed to simulate a state between "good" and "very good" from table 4.1. To maximize its efficiency, the blind was placed outdoors. Table 4.3 contains a summary of the blind's properties. However, it is important to note that for a more accurate simulation, the properties of the blinds should be studied with field testing.

Table 4.3 Properties of the blind for the simulation

Property	Value	Unit
Thickness	0.002	m
Solar transmittance	0.005	-
Reflectance	0.5	-
Infrared transmittance	0	-
Emissivity	0.5	-
Conductivity	0.15	W/mK
Distance to glass	0.10	m
Lateral openness	0	-
Air permeability	0.001	-

The schedules for people, lightning, infiltration, and ventilation were taken from the EnergyPlus library "SmallOffice." The schedule for heating and cooling was built from the occupancy schedule and modified with a fixed setpoint for heating (19°C) and for cooling (24°C)

Four different groups of scenarios were run and explored:

1. Blind down all the time (comprised of 1 scenario);
2. Blind up all the time (comprised of 1 scenario);
3. Blind controlled with the outdoor temperature setpoint (comprised of 12 scenarios);
4. Blind controlled with the solar radiation setpoint(comprised of 12 scenarios).

The range of variables explored is presented in table 4.4.

Table 4.4 Variables explored in the simulation. Range and step adopted.

Variable explored	Min. value	Max. value	Step
Out. T. Setpoint	19 °C	30 °C	1 °C
Rad. Setpoint	50 W/m^2	600 W/m^2	50 W/m^2

For each of the 26 scenarios, the simulation gave three outputs:

1. Number of hours with the blind down: This was considered an essential measurement to account for visual contact with the exterior and ensure that the blind would be activated only when necessary.
2. % of hours in thermal discomfort: The thermal comfort boundary was taken from the typical office scenario illustrated in figure 4.2. The maximum operative temperature was set to 26.15°C and the minimum to 22.5°C.
3. Cooling load: To analyze and minimize the cooling needed.

The two scenarios with blinds always up and always down served as benchmarks for the cooling load and opening hours of the other control strategies. Among the other 24 scenarios the two most optimal ones have been selected by looking at the graphs of the solution. In this case, most optimal refers to the ones that balance most cooling demand and opening hours. Both selections followed the knee-point method, which aims at finding the point which is a solution that represents an ideal compromise among multiple conflicting objectives. For its identification, two approaches have

been used due to the different shapes of the curve of solutions. For the shades controlled by solar radiation the “maximum distance” method explained by Liang et al. (2018) was adopted. For the shade controlled by outdoor air temperature the knee point was identified visually due to the shape of curve formed by the solutions (see figure 4.4B).

4.2.2 RESULTS

Figure 4.4A-B show the result in terms of cooling demand and opening hours of the blinds controller by solar radiation and the ones controlled by outdoor air temperature.

Figure 4.5 shows the application of the maximum distance method to the curve formed by the solar radiation solutions. The picked scenario is the one characterized by a solar radiation threshold of 200W/m2.

The results from these two scenarios together with the two benchmark scenarios are summed up in table 4.5.

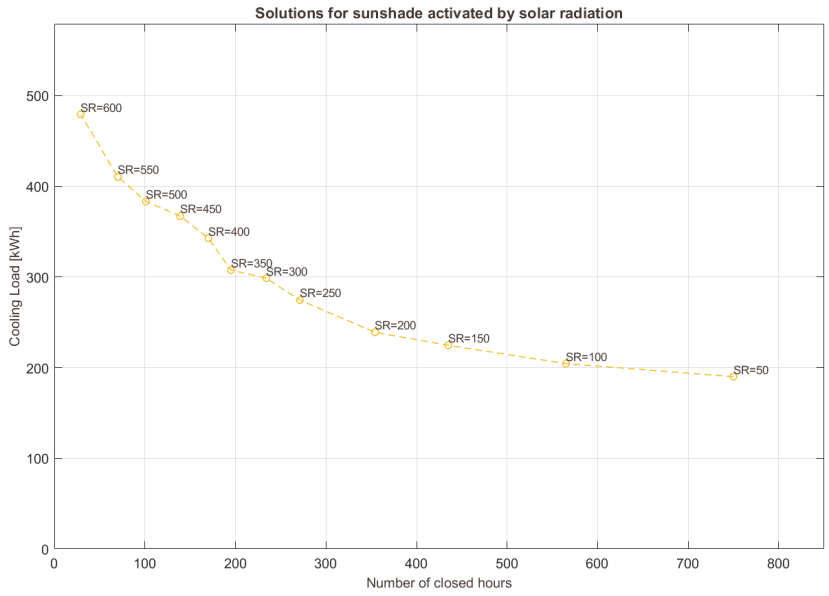

a

Figure 4.4 Cooling loads and number of closed hours for the different control strategy. a) Scenarios controlled by solar radiation.

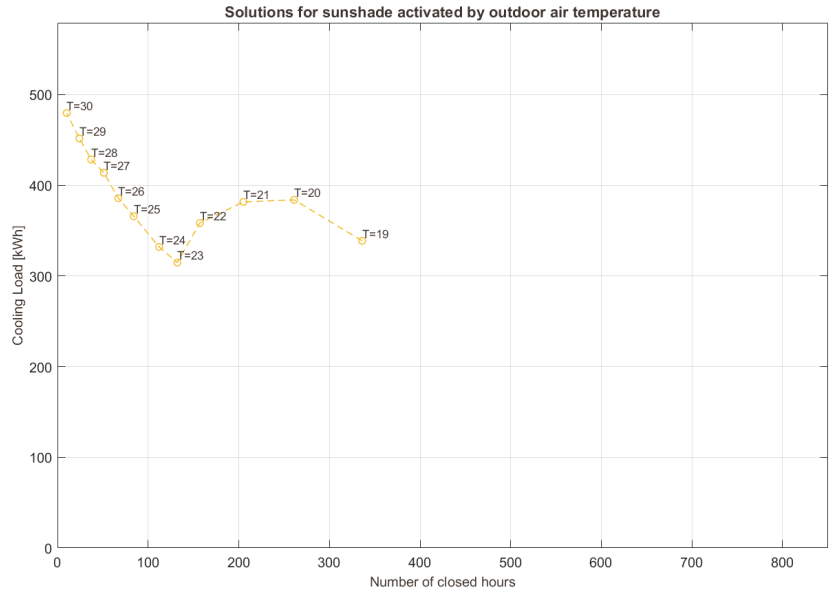

b

Figure 4.4 Cooling loads and number of closed hours for the different control strategy. b) Scenarios controlled by outdoor air temperature.

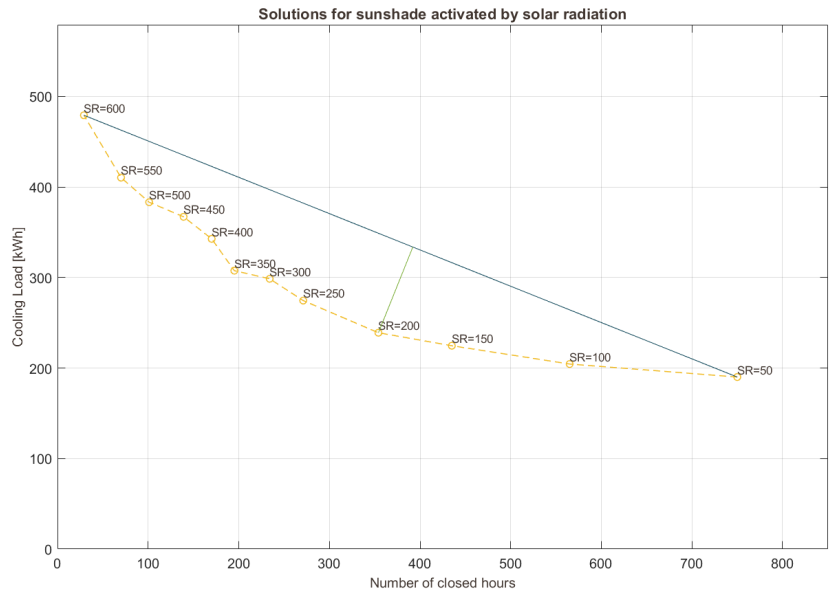

Figure 4.5 Maximum distance knee-point detection method. The blue line connects the extreme solutions and the distance between each solution and the line is calculated. The green line represent the furthest distance which represent the knee-point solution.

Scenario	Radiation Stp. [W/m²K]	Out. T. Stp. [°C]	N. of hours closed	% of hours in thermal discomfort	Cooling load [kWh]
All down	-	-	1122	8.2	199.72
All up	-	-	0	16.8	382.90
Optimal SR	200	-	354	5.9	239.02
Optimal T	-	23	132	18.8	314.86

Table 4.5 Results from the benchmark scenarios and the optimal scenario.

Figures 4.6a-f show the operative temperature, activation time and temperature of the glazing of the two optimal scenarios during the analysis period. Higher peaks of operative temperature are observed in the scenario controlled by outside air temperature with respect to the one controlled by solar radiation. Moreover, in the latter, operative temperature is more distributed throughout the day. The activation time in the scenario controlled by solar radiation is rather constant through the 3 months analyzed and the blind is activated only in the timespan between 9 AM and 5 PM. On the other hand, the activation regulated by outdoor air temperature only happens for a few days each month and for time spans that go from 8 AM to 10 PM. The glazing in both scenarios shows similar profiles but in the scenario controlled by solar radiation the temperatures are lower with respect to the one controlled by solar radiation.

Figures 4.7a-f represent the temperature of the glazing and the solar gains of the room in the scenarios controlled by outdoor air temperature for a threshold of 21°C, 23°C and 27°C. The three scenarios have similar profiles both in terms of glazing temperature and solar gains. However, while the scenario controlled at 21°C and the one at 23°C block almost the same amount of radiation, the one controlled at 27°C blocks less. The temperature of the glazing however, presents slightly less peaks in the 23°C scenario compared to the 21°C and the 27°C ones.

Figure 4.6 Results of the grasshopper simulation for the two optimal scenarios. a) Operative temperature during the analysis period for the optimal scenario with blinds controlled by solar radiation (200 W/m2); b) Operative temperature during the analysis period for the optimal scenario with blinds controlled by outdoor air temperature (23°C); c) Activation time during the analysis period for the optimal scenario with blinds controlled by solar radiation (200 W/m2); d) Activation time during the analysis period for the optimal scenario with blinds controlled by outdoor air temperature (23°C); e) Glazing temperature during the analysis period for the optimal scenario with blinds controlled by solar radiation (200 W/m2); f) Glazing temperature during the analysis period for the optimal scenario with blinds controlled by outdoor air temperature (23°C);

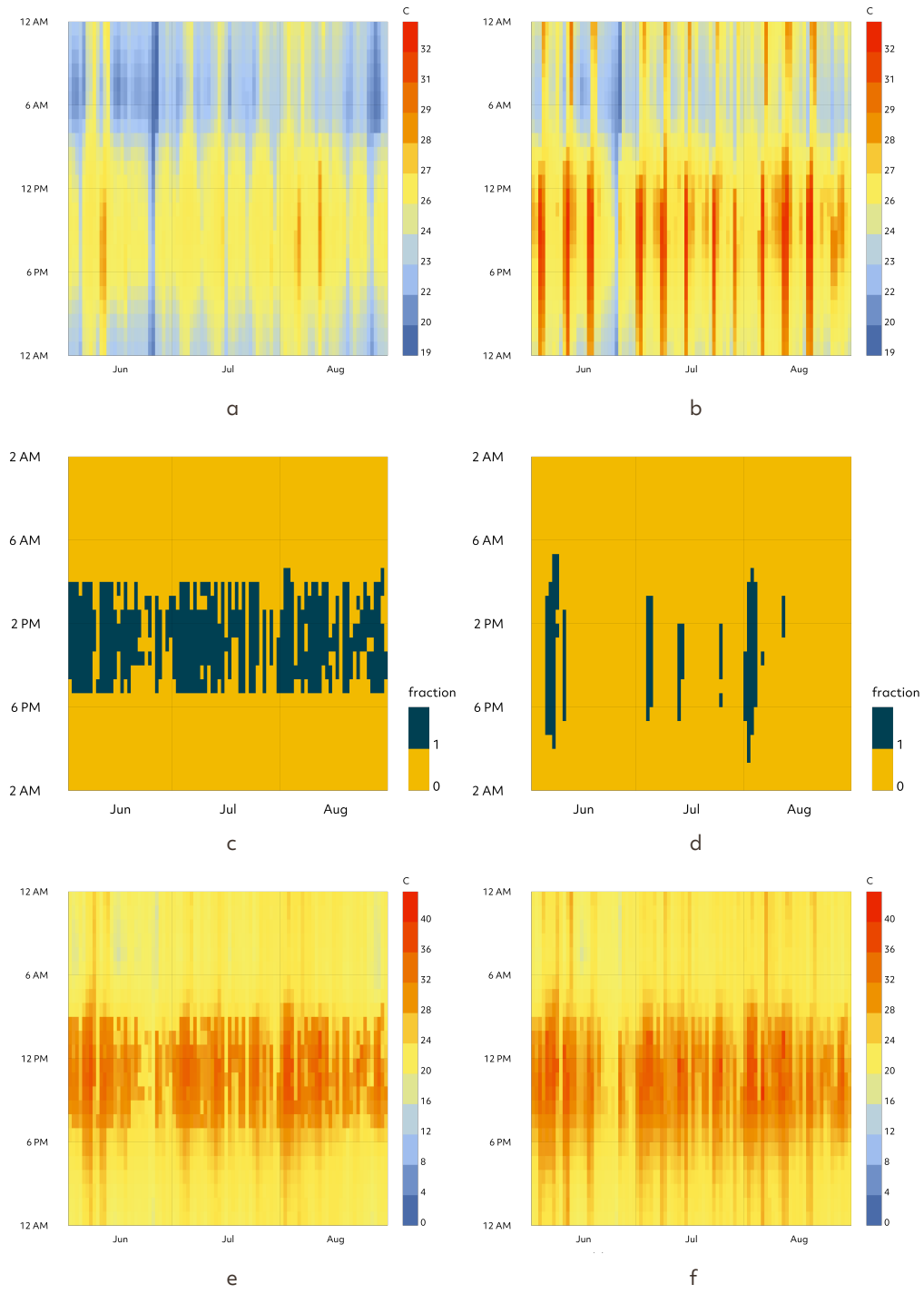

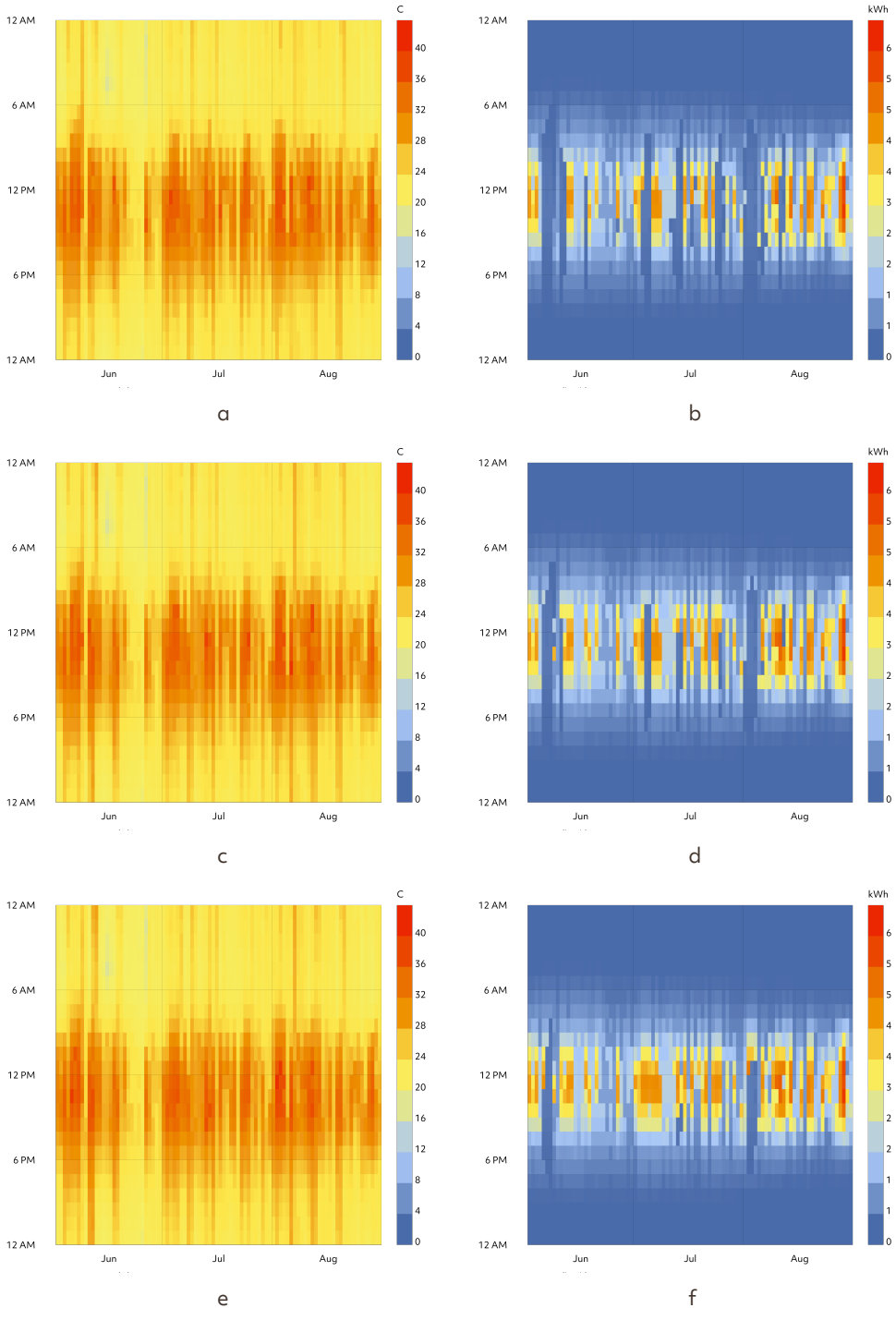

Figure 4.7 Results of the simulation for the scenarios controlled by outdoor air temperature close to the optimal solution. a) Glazing temperature during the analysis period for the scenario with blinds controlled by solar radiation (21°C); b) Solar gains during the analysis period for the scenario with blinds controlled by outdoor air temperature (21°C); c) Glazing temperature during the analysis period for the scenario with blinds controlled by solar radiation (23°C); d) Solar gains during the analysis period for the scenario with blinds controlled by outdoor air temperature (23°C); e) Glazing temperature during the analysis period for the scenario with blinds controlled by solar radiation (27°C); f) Solar gains during the analysis period for the scenario with blinds controlled by outdoor air temperature (27°C);

Figure 4.8 shows the solar gain in the optimal scenario controlled by solar radiation. Compared to the solar gains of the other scenarios, the ones of the optimal scenario controlled by solar radiation are much lower. These do not go above 2kWh for every hour of the analyzed period compared to the peaks of up to 6kWh of the scenarios controlled by outdoor air temperature.

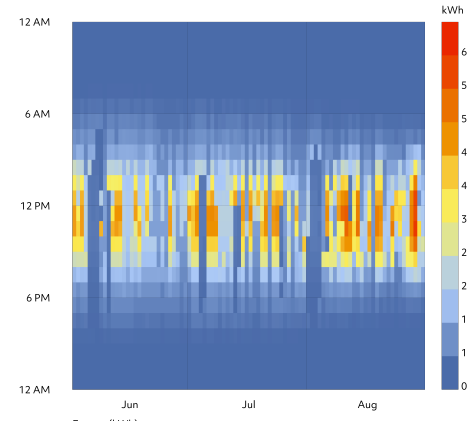

Figure 4.8 Solar gains of the room with the blind controlled by solar radiation with a threshold of 200 W/m2

4.2.3 DISCUSSION

For the scenarios controlled by solar radiation, an optimal solution was identified thanks to the knee point detection method based on maximum distance from the line that connects the two extreme solutions. This solution is considered a good trade-off between the two competing interests of reducing cooling demand and maximizing opening hours. It is noticeable how increasing the opening hours does not lead to a much bigger save in terms of cooling demand. Comparing this optimal scenario with the scenarios with blinds always down, it is noticeable that by decreasing the opening hours to one third we obtain only a 20% increase in cooling demand. Furthermore, the thermal comfort is better maintained in the optimal scenario due to more contained operative temperature (figure 4.6a) thanks to the mitigation of the solar loads (figure 4.8).

The optimal scenario driven by outdoor air temperature produced a counterintuitive curve where the cooling demand rises even when the blinds are closed more. This can be explained from figures 4.7a-f. From the glazing there are two main heat transfers: a temperature driven one (given by convection and radiation between the room and the glazing) and the solar gains. The former is represented in figure 4.7a/c/e with the temperature of the glazing. The solar gains are represented in figure 4.7b/d/f. The 23°C scenario mitigates more solar gains with respect to the 27°C one. The temperature of the glazing is also reduced in the former with respect to the latter. This leads to less loads into the room which then translate to less cooling demand. The 21°C scenario does not block much more than the 23°C one but compared to the latter it leads to higher glazing temperatures. This is because when the blind gets activated the heated glazing is not able to release its heat and warms up even more, leading to higher temperature driven heat transfers with the inside and therefore higher cooling loads.

When comparing the two optimal scenarios, it is noticeable that:

- In the solar radiation driven on there are no major peaks of operative temperature compared to the one driven by outdoor air temperature. This leads to more acceptance in terms of thermal comfort and less cooling loads.
- The temperature of the glazing in the case of blind controlled by solar radiation is lower compared to that of the scenario controlled by outdoor air temperature. This suggests that the temperature of the glazing is more dependent on the incoming solar radiation rather than on the heat transfers with the outside.

- The activation time of the solar radiation driven one is higher but better localized with respect to the one driven by outdoor air temperature. This causes the glazing to not reach high temperatures due to solar radiation and to therefore not overheat the environment with secondary gains due to the temperature driven heat transfers with the inside environment.

4.2.4 CONCLUSIONS

This study helped understand that it is possible to achieve an acceptable indoor thermal environment while lowering the cooling load and maintaining good contact with the exterior. However, it also highlighted the importance of choosing the most effective control strategy. The scenario controlled by solar radiation performed better in terms of thermal comfort and contact with the exterior by increasing the cooling load with a 20% increase with respect to the always down scenario. On the other hand, the scenario with blinds controlled by outdoor air temperature lowered the cooling load by 18% and decreased thermal comfort. When comparing the two optimal scenarios, the one controlled by solar radiation provides 222 more hours with closed blinds with respect to the one controlled by outdoor air temperature. However, the former present less hours in thermal discomfort and 23% less in terms of cooling loads. Given this it is possible to conclude that the scenario controlled by solar radiation proved to be more effective in terms of energy, thermal comfort and visual contact with the exterior, scoring best among the scenarios considered.

4.3 MECHANICAL EFFICIENCY

It is possible to translate the visual contact with the outside as a mechanical requirement. In section 4.2, the control strategy aimed at minimizing the number of hours the sunshade was closed. However, the blind must open up as much as possible when inactivated. For this reason, the system's stroke should be a target of optimization when developing its components.

With this, a mechanical system should also be simple during operation to maximize its lifetime and reduce maintenance. No general and widely accepted definition of "complexity" (Sporns, 2007) exist. However, Simon (1996) suggested defining complex systems as those that are:

> *"made up of a large number of parts that have many interactions."*

From this definition, we can conclude that a sunshade system comprises the least number of components with the least interactions between them and its mechanical designed is aimed at maximixing its opening area.

4.4 SUMMARY

In this chapter, the various aspects that make an effective design have been considered. Exploring multiple scenarios highlighted the importance of choosing the correct control strategy for a specific room in a particular climate. For the case study, solar radiation should activate the sunshade when it exceeds 200 W/m2. Even though no unanimous definition of complexity exists, the number of components and their interactions influence the complexity of a system.

In conclusion, an effective sunshade is controlled by an ideal control strategy that must be tailored to reduce cooling demand, maintain thermal comfort, and maximize opening hours. The mechanical design should minimize components and their interaction while allowing maximum stroke.

MECHANICAL DESIGN

This chapter describes the experimental work performed to assess the structural behavior of the counterAKT system. Section 1 introduces the design of the system. Section 2 guides through the mechanical testing performed to characterize the textile. This section aims at answering the second sub-research question:

"How can the textile be designed to provide a sufficient range of movement for an effective operation?"

Section 3 deals with the design of the spring and aims to answer the third sub-research question:

"How can the SMA spring be designed to accommodate the movement of the textile?"

Section 4 summarizes and concludes the previous sections.

5.1 THE COUNTERAKT

One of the objectives of this work was to reduce the mechanical complexity of passive dynamic sunshades. As stated in section 4.4, this translates to reducing the number of components and their interaction. This is the design principle of counterAKT (Active Knitted Textile), the first system where the textile actively participates in the mechanical system. This design (figure 5.1) reduces the number of components to only two elements. Two essential parts that combine various functions make up the entire design. The textile binds the whole structure together, works as the actuator's counteracting member, and can provide shade. On the other hand, the shape memory spring is the sensor and actuator that pulls the textile down, activating the system when needed.

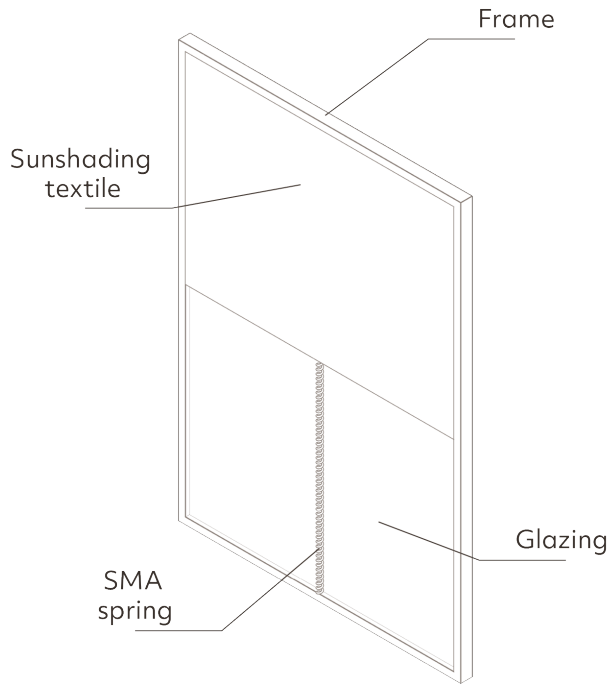

Figure 5.1 Scheme of the counterAKT system

In parallel, the counterAKT is designed to maximize its stroke, allowing for the most visual contact with the exterior. To optimize the performance of the counterAKT, it is crucial to accurately determine and appropriately size the mechanical properties of both components.

5.2 TEXTILE CHARACTERIZATION

The textile used in the counterAKT must exhibit two distinct mechanical behaviors: it must be capable of undergoing significant deformation when subjected to the activated SMA spring, and it must generate a pullback force capable of returning the spring to its original state. Previous research has attempted to predict the mechanical response of knitted textiles using a range of methods, including finite element analysis (Vassiliadis, et al., (2006), Dinh, et al., (2018)), mathematical models (Choi & Lo, 2003), analytical simulations (Weeger, et al., 2018), and experiments (Choi & Lo, (2006), Umar, et al., (2016)). However, the mechanical response of knitted textiles is influenced by numerous parameters, making it challenging to accurately predict their behavior without conducting physical tests. Indeed, in the literature, every model presented required a physical counterpart to validate the analysis. Therefore, experimental validation is necessary to accurately determine the mechanical behavior of the textile in the counterAKT, as the response of the textile is highly dependent on its unique composition and characteristics. In addition, modeling and simulation techniques, such as Finite Element Analysis, require significant time and effort to achieve a specific performance, which is not feasible within the scope of this thesis.

Therefore, physical testing of textile mechanical properties was chosen to be the correct methodology. The testing objective was to identify the ideal combination of textile parameters to enable the textile to achieve two key performance criteria. First, the textile had to stretch significantly when subjected to a known force. Secondly, the fabric had to return to its starting position when partly unloaded, as the force from the inactive SMA spring never reaches zero. To assess this, the experiment was designed to measure the deformation of the textile specimen under a known force to evaluate its ability to achieve the desired mechanical behavior. In light of this, two different tests were conducted on the samples to understand their behavior:

1. Lateral Load (LL) – Performed by placing the two containers on each side of the textile and loading them progressively.
2. Lateral Load with Guide (LLG) – Performed similarly to the LL, guiding the textile through the lateral metal bars and eventually adding an elastic (LLEG).

5.2.1 METHODOLOGY

The textile's deformation and recovery ability were measured using the experimental setup in figure 5.2. The setup comprised of:

1. A measuring testing frame (40 cm x 60 cm) (figure 5.2.A) was constructed from 5 wooden elements screwed together to accommodate the textile to stretch in the designated hooks (figure 5.2.B). A measuring tape was attached to the side of the vertical posts to assess the deformation of the specimen during the experiment (figure 5.2.C). Two metal guides were mounted to experiment with impaired lateral deformation (figure 5.2.D).
2. Dead loads – comprised of (2) containers that could fit weights. The containers and the weights were changed when further testing was done to achieve more force. Load case 1: containers of 0.0185 kg (figure 5.2.E) and weights of 0.0183 kg (figure 5.2.F) (total weight with 2 containers with 12 weights each: 0.4762 kg). Load case 2: containers of 0.082 kg (figure 5.2.G) and weights of 0.0265 kg (figure 5.2.H) (total weight with 2 containers with 14 weights each: 0.906 kg).
3. Textile specimen – with varying parameters as described in section 3.2.2. (figure 5.2.I)

The testing of each textile followed a strict order of operations. First, the textile was placed on the hooks, and the resting length was measured (figure 5.3.A). Guides were inserted if the test involved restricted lateral deformation (figure 5.3.B). Following the setup, the specimens were progressively loaded, and the achieved deformation was measured (figure 5.3.C) until the max length (set to 40 cm) or the max load was reached. Subsequentially, the textiles were progressively unloaded, and the residual deformation was measured (figure 5.3.D).

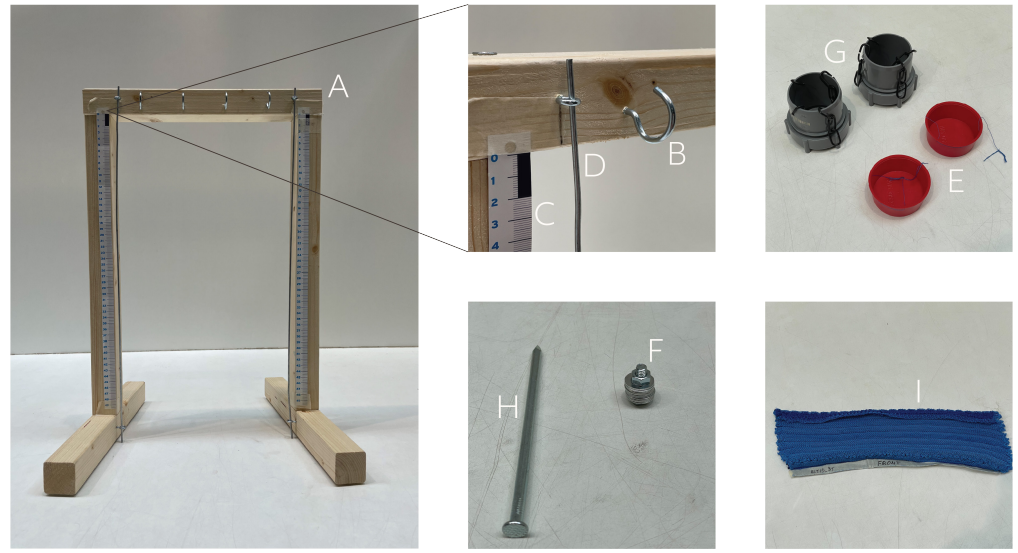

Figure 5.2 Components for the mechanical testing. A) Wooden frame built for testing; B) Resting hooks for the textiles; C) Measuring tape; D) Metal guides for the llg tests; E) Containers for load case 1; F) Weights for load case 1; G) Containers for load case 2; H) Weights for load case 2; I) Example of a specimen for the test.

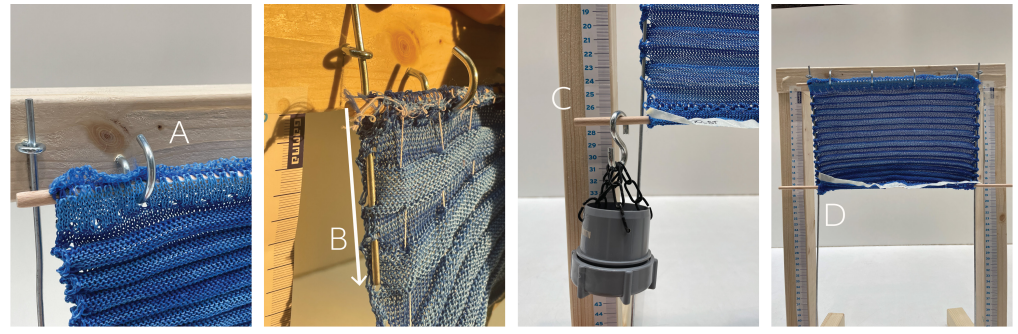

Figure 5.3 Steps for the tests. A) Positioning of textile on resting hooks; B) Insertion of metal guide in case of llg through the holes; C) Progressive loading and measurement of deformation; D) Measure of residual deformation.

5.2.2 MATERIALS

The fabrication of the textiles followed an iterative process based on the findings of the previous step. In this work, the specimens have been divided into three groups depending on which yarns were used during production for comparative results. The specimens have been fabricated using a 10.2-gauge flatbed knitting machine.

The used yarns are presented in table 3.1:

Table 5.1 Yarns used during fabrication.

Material	Abbreviation	Color	Used in group
Polyester	PES	Blue	1, 3
50% Elastane 50% Polyamide	EL	White	1, 2

While the PES yarn was chosen as it was readily available in TU Delft and already proven suitable for knitting (Popescu, 2019), the EL yarn was found online and ordered from a shop specialized in sewing materials.

To understand the design behind the specimens tested, it is important to understand the base principles behind an industrial knitting machine. A knitting machine uses a series of needles that move back and forth to create interlocking loops of yarn. The machine has two flatbeds that hold the fabric in place and a carriage that moves the needles across the fabric. As the carriage moves, the needles pick up the yarn and knit it into the fabric, creating the desired pattern (figure 5.4).

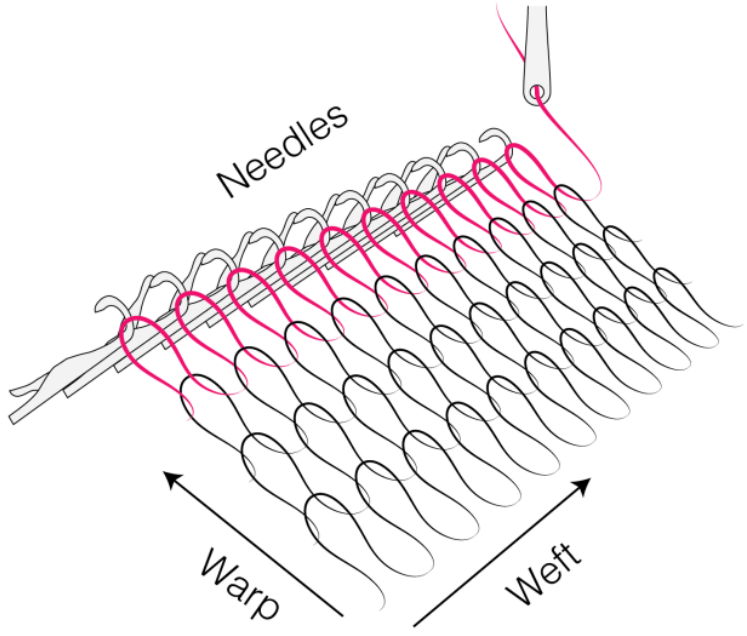

Figure 5.4 Industrial flat-bed knitting machine typical needle-bed layout: array of needles creating loops course-wise by pulling yarn fed by a yarn guide. Note that this is a scheme of a single bed in the machine, two of these are facing each other. (image from (Popescu, 2019))

It is possible to reach different textile configurations by varying parameters during the knitting process. In this work, the knitting pattern adopted by the machine during production is referred to as the "architecture of the knit" or "knit architecture." In the samples tested, two main knit architectures have been used and combined: the alternating single jersey, also referred to as "ALT" (figure 5.5.A), and the double jersey, also referred to as "RIB" (figure 5.5.B).

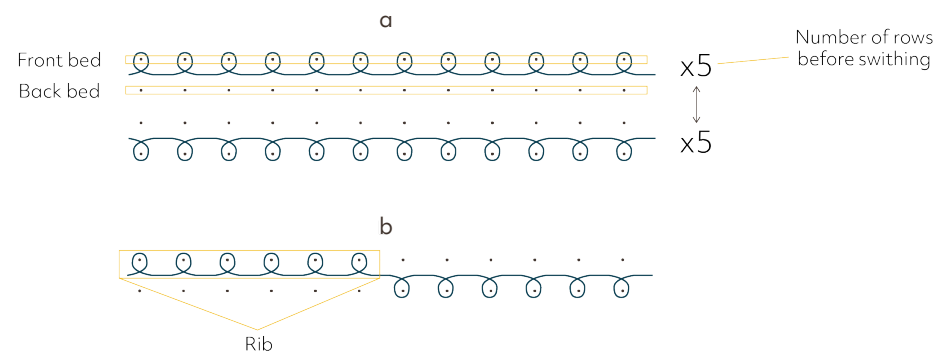

Figure 5.5 Knit architectures explored within this thesis: a) ALT design, the number of rows before switching could be 5, 10, 15, b) RIB design, in the figure, a rib is composed of 6 loops, but in the thesis we explored other options (see table 3.2-4).

Both patterns exploit the natural curvature the knitting process gives to the textile. In the ALT design, the curvature is given by the pulling action of the two single-needle beds knitting alternatively during the process. The resulting geometry presents rows knitted in the front bed that want to curve in the opposite direction in contrast with the ones knitted in the back bed due to the pulling action of the needles, creating an accordion-like structure in the warp direction (figure 5.6.A). On the other hand, the RIB knit architecture exploits the pulling action generated from the natural tendency of loops to pull inwards toward each other. Tension is created by having some loops generated on one bed, forming a rib, and some on the opposite one. This generates an accordion-like structure in the weft direction (figure 5.6.B). The two curving designs have been chosen as they can curl up when not tensioned, occupying little space and becoming planar when loaded.

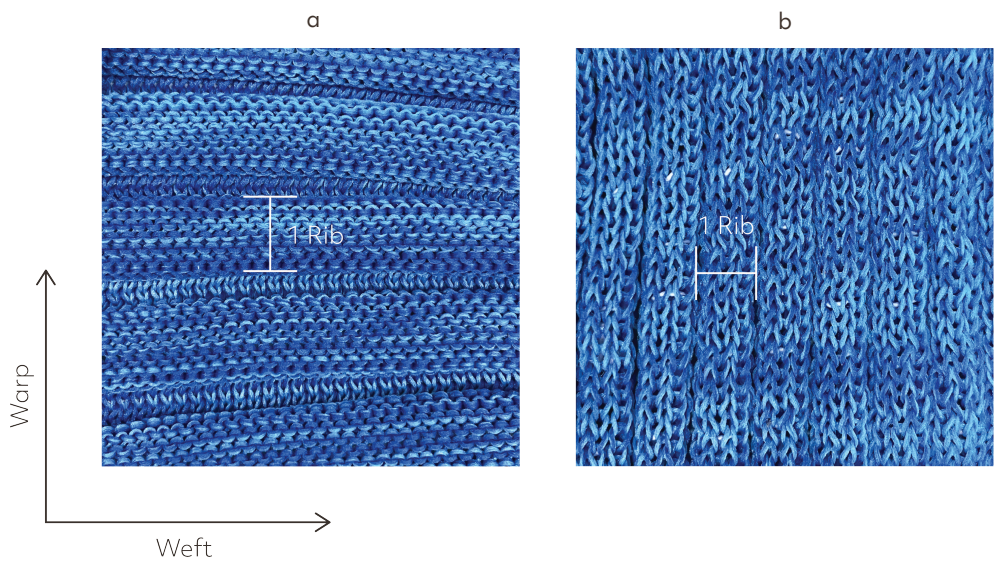

Figure 5.6 Close-up of the different fabrics. a) ALT design with ribs in the warp direction, b) RIB design with ribs in the weft direction.

The parameters explored within this work are different for the two knit architectures. The ALT designs explored the number of rows knitted on one bed before moving the textile to the opposite bed. The number of needles used to create a rib varied in the textiles using the RIB architecture. In both designs, the number and type of yarns were changed. Finally, the EL yarn was inserted as an inlay in the third group of textiles, while the PES yarn was used to create the main pattern. For this final variant, the resting length and the number of inlays varied throughout the specimens. The inlay was inserted by hand after producing the main textile for the ALT design. It could be straight or follow a zig-zag pattern (figure 5.7). The inlay was inserted during production but tensioned afterward for the RIB design. The specification for each textile specimen can be found in tables 5.3-5, where textiles have been grouped based on the yarn used during fabrication.

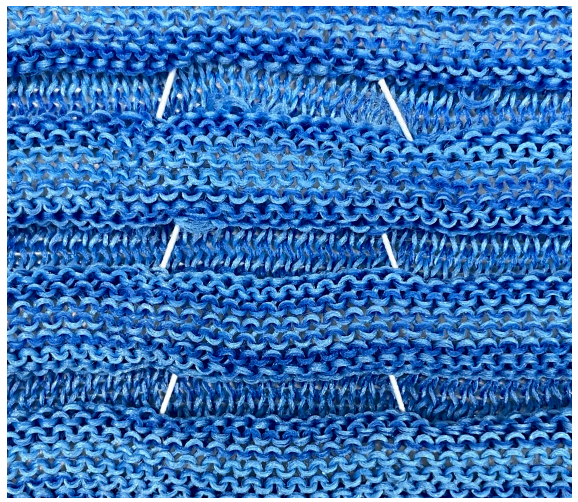

Figure 5.7 Elastic inlay in zig-zag pattern inside ALT design

Table 5.2 Specimens produced using the PES thread. Properties regarding the knit architecture together with the loading conditions.

Name	Knit architecture	Number of plies	Loading type	Load direction	Number of loops
ALT5_4T	ALT (5 rows before switching)	4 PES	LL, LLEG	Warp	120 (weft) 210 (warp)
ALT10_3T	ALT (10 rows before switching)	3 PES	LL, LLEG	Warp	120 (weft) 210 (warp)
ALT10_4T	ALT (10 rows before switching)	4 PES	LL, LLEG	Warp	120 (weft) 210 (warp)
ALT10_5T	ALT (10 rows before switching)	5 PES	LL, LLEG	Warp	120 (weft) 210 (warp)
ALT10_6T	ALT (10 rows before switching)	6 PES	LL,	Warp	120 (weft) 210 (warp)
ALT15_3T	ALT (15 rows before switching)	3 PES	LL, LLEG	Warp	120 (weft) 210 (warp)

Table 5.3 Specimens produced using the EL thread. Properties regarding the knit architecture with the loading conditions.

Name	Knit architecture	Number of plies	Loading type	Load direction	Number of loops
ALT10_ET	ALT (10 rows before switching)	1 EL	LL	Warp	60 (weft) 105 (warp)
ALT10_ET_W	ALT (10 rows before switching)	1 EL	LL	Warp	120 (weft) 55 (warp)
ALT10RIB3_ET_W	ALT (10 rows before switching) RIB (3 needles rib)	1 EL	LL	Warp Weft	120 (weft) 55 (warp)
RIB1_ET_W	RIB (1 needle rib, skip 1)	1 EL	LL, LLG	Warp	120 (weft) 55 (warp)
RIB2_ET_W	RIB (1 needle rib, skip 2)	1EL	LL, LLEG	Warp	120 (weft) 55 (warp)

(*) Every ALT design was made by skipping one needle as the elastic yarn was too tight and would get tangled in the machine. In the RIB designs, this was prevented by skipping one or more needles between a rib and the next one.

Table 5.4 Specimens produced using the PES thread with the EL interlay. Properties regarding the knit architecture with the loading conditions.

Name	Knit architecture	Number of plies	Loading type	Load direction	Number of loops
ALT_10_PET_1	ALT (10 rows before switching)	4 PES 10 EL (10.3 cm)	LL	Warp	120 (weft) 210 (warp)
ALT_10_PET_2	ALT (10 rows before switching)	4 PES 10 EL (14.2 cm) diag.	LL	Warp	120 (weft) 210 (warp)
ALT_10_PET_3	ALT (10 rows before switching)	4 PES 10 EL (14.4 cm) diag.	LL	Warp	120 (weft) 210 (warp)

Name	Knit architecture	Number of plies	Loading type	Load direction	Number of loops
ALT_10_PET_4	ALT (10 rows before switching)	4 PES 8 EL (14.4 cm) diag.	LL	Warp	120 (weft) 210 (warp)
ALT_10_PET_5	ALT (10 rows before switching)	4 PES 6 EL (14.4 cm) diag.	LL	Warp	120 (weft) 210 (warp)
RIB_10_PET_1	RIB (5 needles rib)	4 PES 10 EL (12.2 cm)	LL	Weft	100 (weft) 90 (warp)
RIB_10_PET_2	RIB (5 needles rib)	4 PES 16 EL (16.6 cm) diag.	LL	Weft	140 (weft) 180 (warp)
RIB_10_PET_3	RIB (5 needles rib)	4 PES 14 EL (16.6 cm) diag.	LL	Weft	140 (weft) 180 (warp)
RIB_10_PET_4	RIB (5 needles rib)	4 PES 12 EL (16.6 cm) diag.	LL	Weft	140 (weft) 180 (warp)
RIB_10_PET_5	RIB (5 needles rib)	4 PES 10 EL (16.6 cm) diag.	LL	Weft	140 (weft) 180 (warp)

5.2.3 RESULTS

Figure 5.8.A-F presents the results divided by loading type and yarn used. The results are graphed in loading (brighter) and unloading (lighter) curves of the textiles during the experiments. The specimens not tested under the LLG conditions were produced without holes for the guide to run through, making them unfeasible to test under this condition. It is important to remark that the vertical axis represents the load per each side of the textile. To find the total force the textile was subject to the value on the y-axis should be multiplied by a factor of 2.

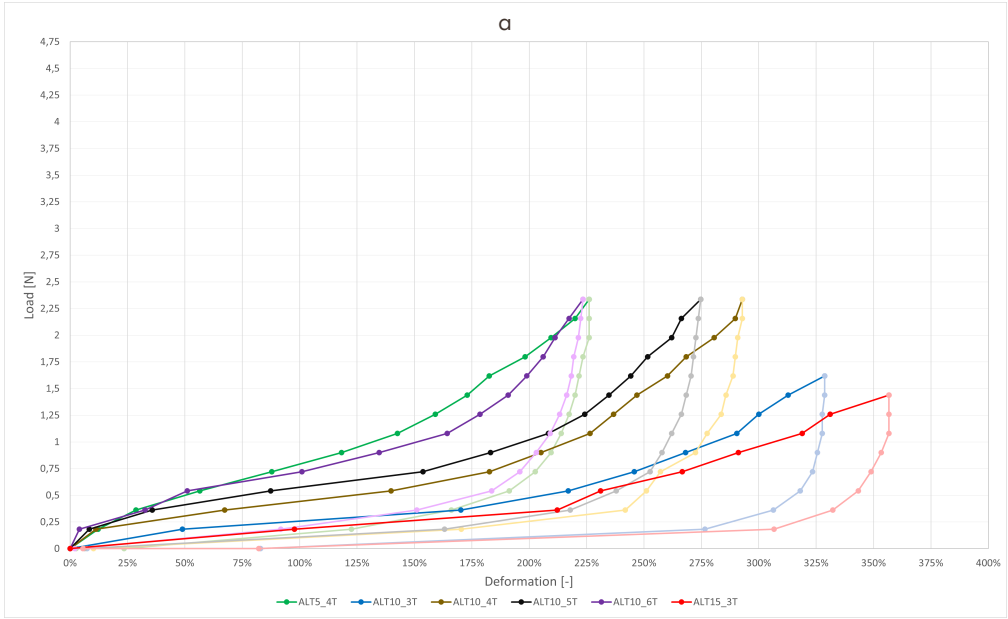

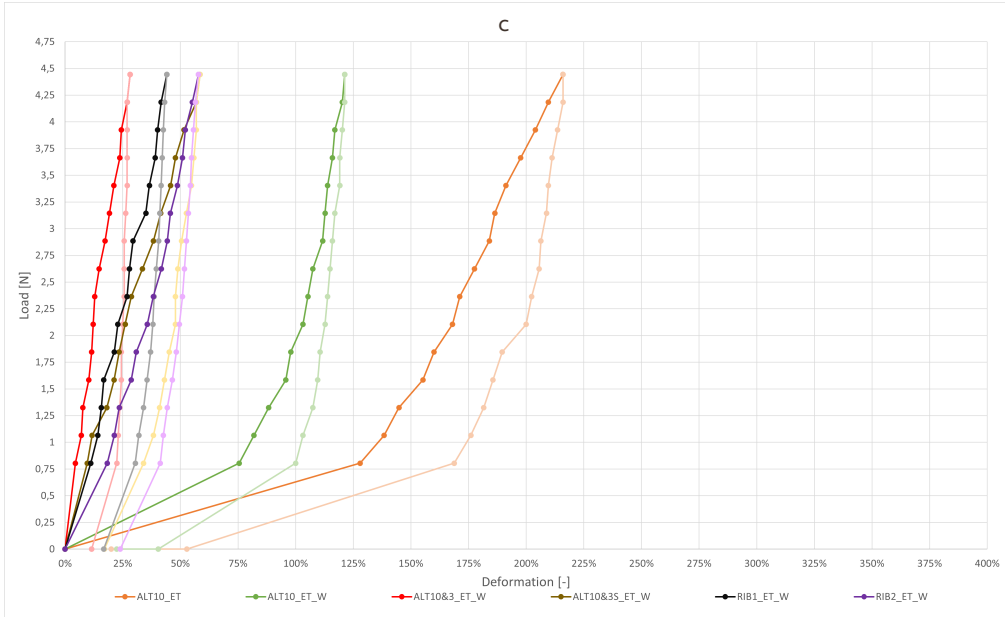

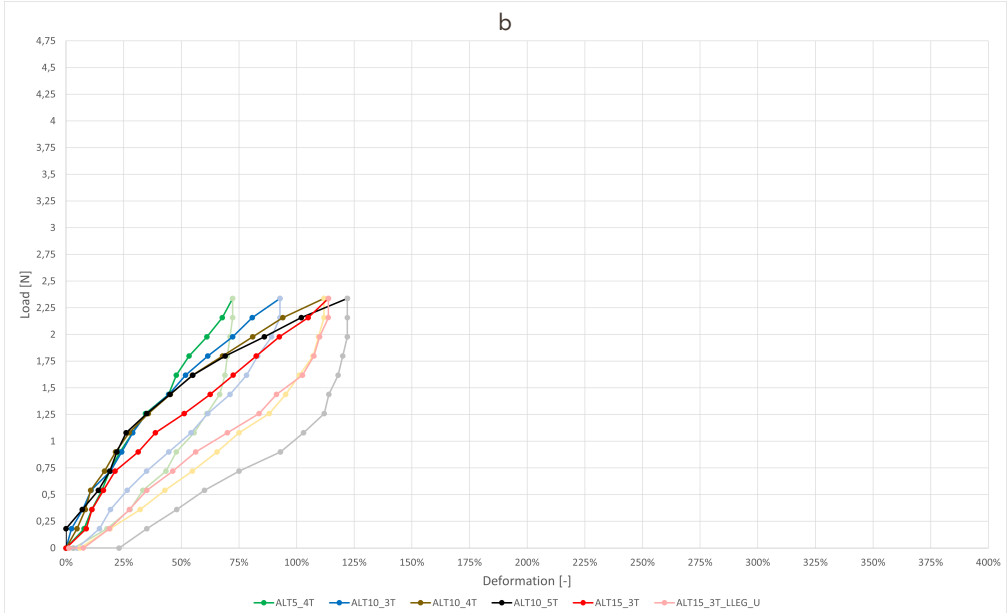

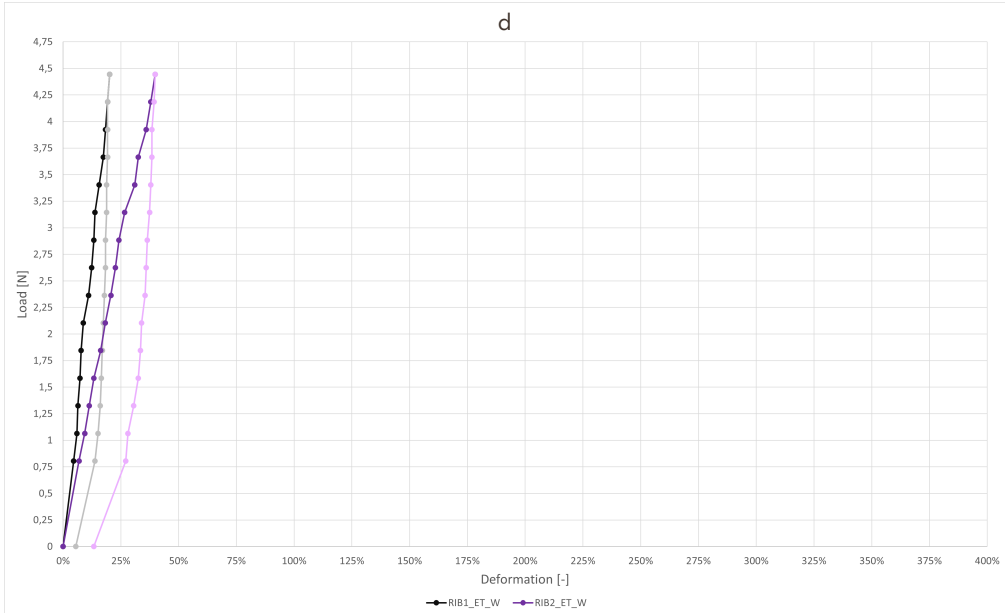

Figure 5.8 Results from the different tests. a) PES group under LL; b) PES group under LLEG.

Figure 5.8 Results from the different tests. c) ET group under LL; d) ET group under LLG.

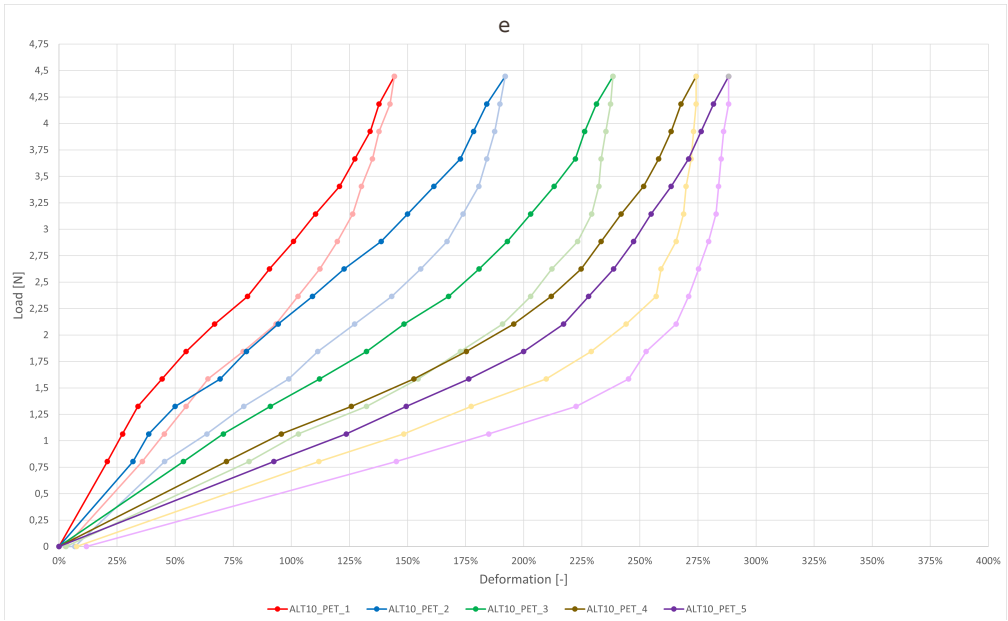

Figure 5.8 Results from the different tests. e) PES+ET ALT group under LL; f) PES+ET RIB group under LL.

The first experiments concerned only the PES textiles with alternating geometry without lateral restriction from the guides. The tests showed the most significant deformation among the specimens (up to circa 350% for the ALT15_3T) but an inability of the samples to go back to the original shape when unloaded partly (see figure 3.3.D). Furthermore, the study of the different parameters showed different trends. Namely:

- Adding more yarns increases the stiffness of the textile, leading to less deformation for an equivalent load;
- Adding rows before switching knitting beds leads to more deformation for an equivalent load.

The metal guides on the side were added together with commercial elastic bands to give the textile more pullback strength and prevent them from deforming laterally. The metal guides would keep the sunshade with straight edges (figure 5.9.A-B). At the same time, the stress generated from the prevented lateral deformation would also stiffen the textile, much like when a concrete column is jacketed with metal constraints (figure 5.9C).

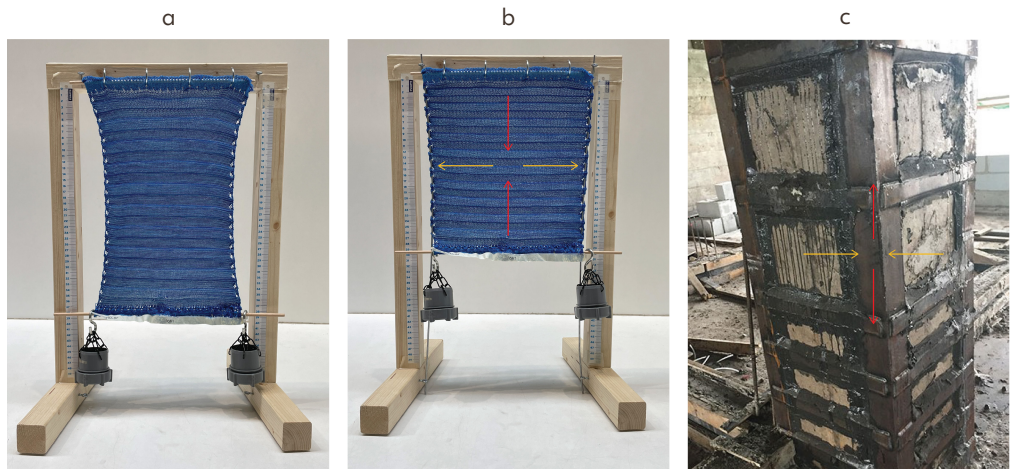

Figure 5.9 Effect of the metal guides on the textile. a) Lateral shrinking due to Poisson forces, b) Prevented lateral deformation of the textile due to the extra stresses generated by the guides (yellow) and the Poisson-induced stresses (red) that make it stiffer, c) Analogy with concrete column jacketing (Constro Facilitator, 2023)

The results from the LLEG tests show increased stiffness as the same specimens get much less deformed when the metal guides are inserted, but the gap between the loading and the unloading is still remarkable. This is mainly due to the additional friction generated between the textile and the guides, which stops the specimen from retracting once unloaded. Furthermore, it is noticed that all the specimens show a similar behavior until the load arrives at 1.32 N. This can be attributed to the addition of the elastic, which plays the most important role in the deformation when the geometry is still not tensioned.

In general, it was noted that even though the yarn of the specimen was made of PES, the textile behaved like an elastomer in loading and unloading (figure 5.10).

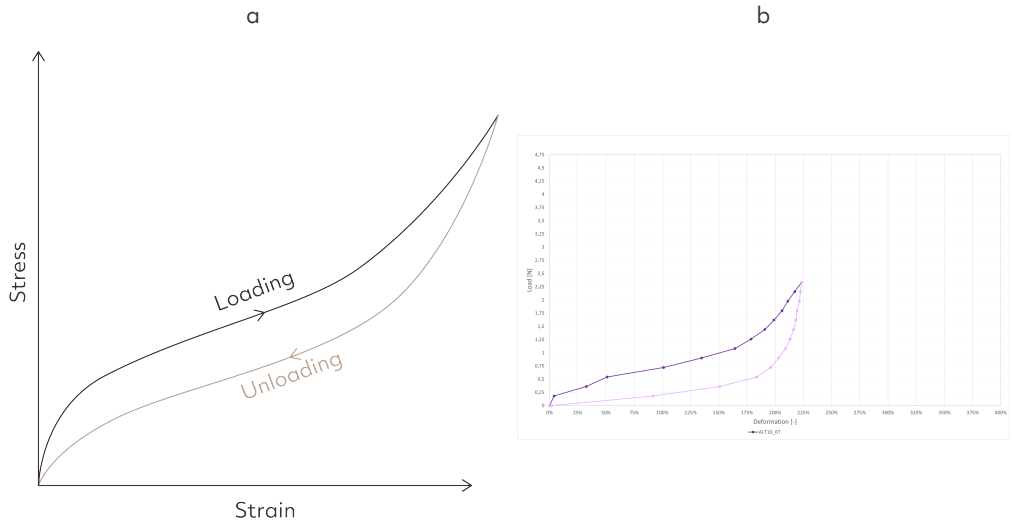

Figure 5.10 Similarity between the typical elastomer curve (a) and one of the specimens (b)

The second group of textiles showed stiffer behavior when compared to the first group. Only a little difference is observed throughout the specimens except for the two ALT10 designs, where a large deformation is achieved initially. The LLG test was carried out only for the two RIB specimens but did not achieve largely different results compared to the LL test. Furthermore, elastic hysteresis is still observed but more contained than in the first group.

Finally, the performance of the third group of textiles can be collocated between the two previously described groups. The PES+EL textiles show a great range of behaviors even though the knit architecture of the PES part was kept the same throughout the

specimens, except for the RIB10 design. Therefore, the significant difference between the specimens can be attributed to the EL part, where different trends were observed. Namely:

- Lowering the number of elastic inlays leads to more deformation and more elastic hysteresis, leading the sample to a behavior similar to the one observed in the first group of textiles;
- Increasing the length of the elastic inlays while creating a zig-zag pattern leads to more deformation

5.2.4 DISCUSSION

The tests showed that the three groups present very different behaviors. However, the combination of the PES and EL yarns in the last group shows the most promising deformation and spring-back results. The reason for this lies in the results from the two previous groups. PES-only textiles can deform a lot under a progressive load, making them excellent at covering large areas when tensioned and small ones when resting. Combining this property with the reduced elastic hysteresis from the second group gives the specimen the ability to have enough force to raise the system back to its original shape while keeping a large deformation. Furthermore, it was found that the LLG test worsens the performance of the textiles as it adds friction between the textile and the metal bar.

Amongst the specimens of the third group, the RIB10_PET1, and the ALT10_PET2 are the ones that behave the best as they present an acceptable level of deformation (above 175%) and are still capable of bringing the system back to the original position. However, more iterations could be performed while varying the starting length of the elastic yarns, their number, and the pattern they follow along the length of the specimen. Furthermore, other types of elastics could be tested with the same geometry to understand the material's influence on the textile's performance.

Generally, the difference between the loading and unloading curves in an elastomer is caused by elastic hysteresis, which is attributed to the energy dissipated due to the material internal friction (Illinois Tool Works Inc., sd). It is plausible that the friction between every textile loop diminishes its capability of returning to its original preloaded geometry.

It is essential to notice the different responses between ALT10_ET and its wide version ALT10_ET_W. While the only difference between the two specimens is the number of loops in the weft and warp direction, their behavior varies significantly, with the first one achieving more than 200% deformation and limited recovery and the latter slightly below 125% with a more emphasized recovery. This highlights that the textile response is subject to size and should therefore be studied more deeply on a real scale to size the system.

Overall, the results show that designing a textile capable of undergoing significant deformation and recovering a big part of its original state when partly unloaded is possible. However, the deformation achieved within this work is still limited to below 200% if one wants to achieve enough spring back force and low residual deformation. Furthermore, the elastic hysteresis has been dealt with partly, but varying the parameters of the third group could lead to better results. Additionally, it is important to notice that the two knit architectures explored within this work only cover a small portion of the many customizations that one can achieve with knitting, and even within these two, the parameters changed were limited to a couple of iterations. Finally, the elastic inlays of the third group have been tensioned by hand in post-production, not making the solution suitable for large-scale, serialized applications.

5.3 SMA SPRING DIMENSIONING

Unlike textiles, SMA springs have less degree of customization in terms of geometry and mechanical properties. This has allowed the formulation of known laws that characterize the behavior of these objects (Yamauchi, et al., 2011). This brief section presents the process of sizing the SMA spring. The proposed analytical model was validated by testing a real spring with known geometry with the RIB_10_PET_1 textile.

5.3.1 METHODOLOGY

Figure 5.11 and table 5.5 show the parameters involved in the design of a spring.

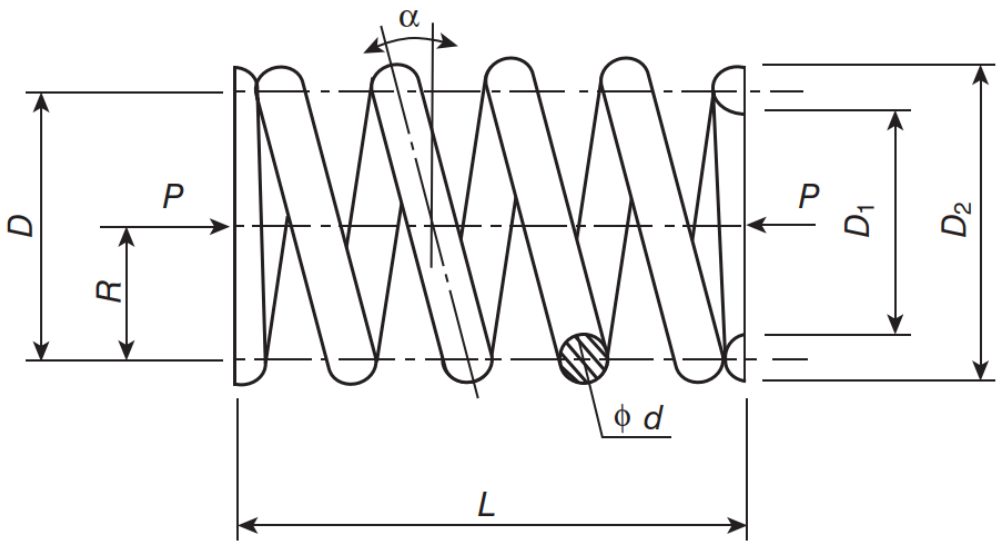

Figure 5.11 Scheme of the main geometrical properties to define a spring. (from: (Yamauchi, et al., 2011))

Table 5.5 Parameters used for springs in figure 5.11 and equations 5.1-3 (Adapted from (Yamauchi, et al., 2011))

Symbol	Meaning	Unit
d	Wire diameter	mm
D_1	Inside coil diameter	mm
D_2	Outside coil diameter	mm
D	Mean coil diameter $D = (D_1+D_2)/2$	mm
N	Total coils	-
n	Active coils	-
L	Free length	mm
P	Load	N
δ	Deflection	mm
τ	Shear stress	MPa
γ	Shear strain	%
G	Shear modulus	MPa
C	Spring index	-
k	Spring constant	N/mm

These are governed by the following equations (Yamauchi, et al., 2011):

(eq. 5.1)
$$\delta = \frac{8PD^3n}{Gd^4}$$

(eq. 5.2)
$$\gamma = \frac{\delta d}{\pi n D^2}$$

(eq. 5.3)
$$G = \frac{\tau}{\gamma}$$

Using these, it was possible to derive an algorithm to calculate the optimal shape of a spring given the loading and unloading curve of the textile obtained through the previous test. With optimal, it is intended a profile that maximizes the stroke of the system while not exceeding the strength of the SMA during deformation. A scheme of the script is given in figure 5.12.

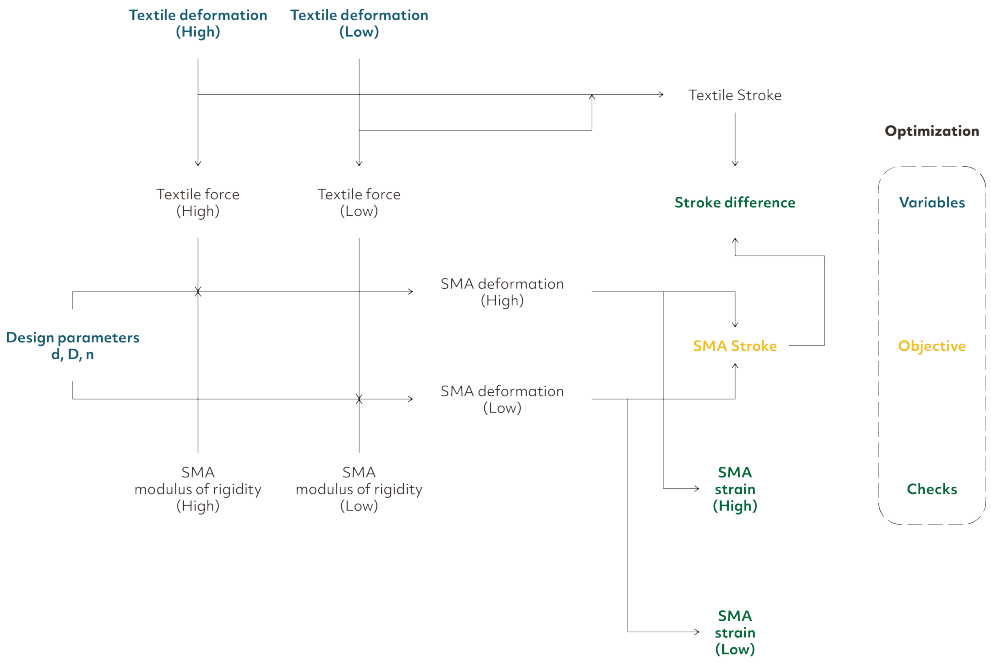

Figure 5.12 Scheme behind algorithm to size the spring. The variables are highlighted in blue, the objective in yellow and the checks for a valid solution in green.

The first step consisted of collecting the data from the textile and the possible interval for each geometric parameter. In the equations above, this means determining P, D, n, d, and G. P is the load to which the spring is subjected and depends on the type of textile and its deformation. By linearizing the curves obtained from testing, we get an equation of the kind: $ax+b$, where a and b will depend on the textile specimen and x is the deformation of that particular textile. The result will give us the tension the textile was exerting in that specific state, i.e., the load P on the SMA spring (figure 5.13).

D, n, d ranged from the option available from an online supplier of SMA springs, but the script could be easily changed to accommodate more variants. Finally, G was assumed equal to 8000 MPa in the low-temperature (Martensite) phase and 20000 MPa in the high-temperature (Austenite) phase. The value in the martensitic phase was then changed to 3600 MPa after the physical validation.

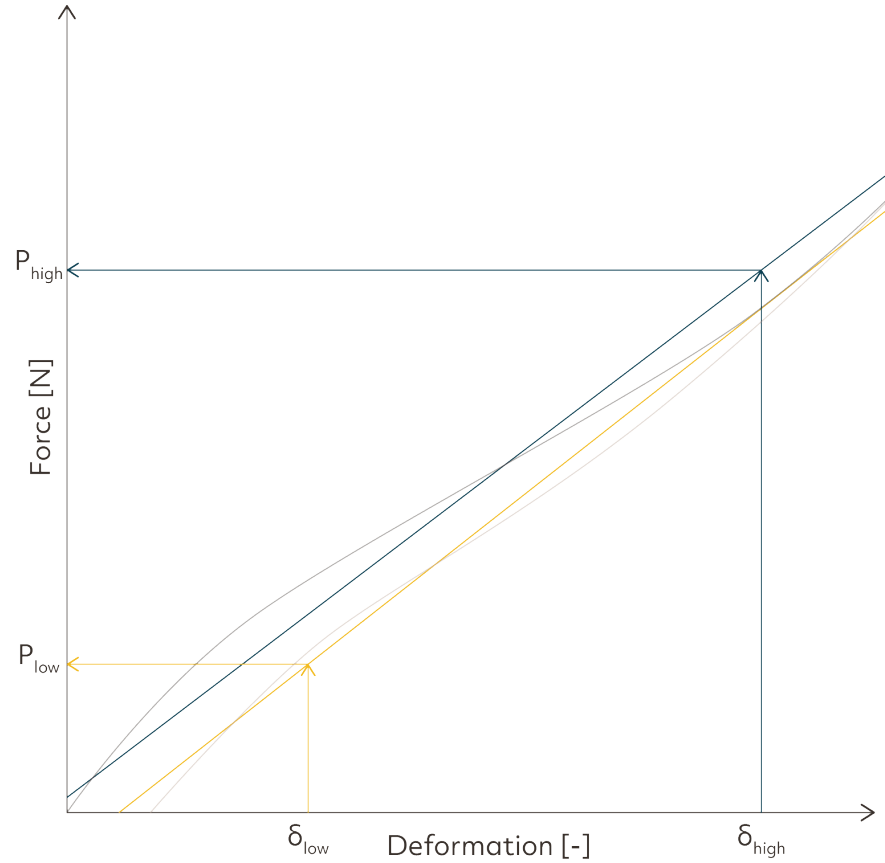

Figure 5.13 Logic to get the force exerted by the textile knowing its deformation.

Knowing D, n, d, P, and G, the deflection δ was calculated for both SMA phases. Knowing the deflection and the geometrical parameters, the strain was calculated, and after that, the stress. Validation was done by inserting the known values in the script and comparing the output deflection with actual measurements.

The script would then optimize the spring by varying its geometrical parameters and the input deformation of the textile. Varying the latter meant changing the force the SMA was subject to.

The optimization was an SOO (Single Objective Optimization) aimed at maximizing the stroke of the textile. However, some checks were implemented by the use of a penalty function. The penalty function is an algorithm presented in Appendix A that checks that a particular variable enters within a range of admissible values. If it does not, it applies a penalty to the objective variable of the optimization.

In this specific script, it was implemented to prevent the SMA from undergoing plastic deformation, and that the stroke of the textile was similar to that of the SMA spring. This last check can be considered a congruence check to verify that both components are moving similarly. If it was not implemented, the spring and the textile could have different strokes, an impossible situation in the actual working of the system. Furthermore, a check on the system's dimensions was implemented. Table 5.6 summarizes the values used in the penalty test and their acceptability range.

Table 5.6 Values to check in the penalty function and admissible range.

Value to check	Min Value	Max Value
System's dimension (High)	0 mm	400 mm
System's dimension (Low)	0 mm	400mm
Difference between strokes	-20 mm	20 mm
Shear stress (High)	0 MPa	400 MPa
Shear stress (Low)	0 MPa	400 MPa

5.3.2 RESULTS

The results from the physical testing and the validation run in the script produced discrepant results. The results are summed up in table 5.7.

Table 5.7 Results from the two methods assuming a modulus of rigidity of 8000MPa for the martensitic phase (low).

Method	Deflection High	Deflection Low	Stroke
Analytical	45.23 mm	56.91 mm	11.68 mm
Experiment	~ 45 mm	~ 121 mm	~ 76 mm

After changing the modulus of rigidity of the martensitic phase to 3600 MPa, the analytical results matched the measurements. These are presented in table 5.8.

Table 5.8 Results from the two methods assuming a modulus of rigidity of 3600MPa for the martensitic phase (low).

Method	Deflection High	Deflection Low	Stroke
Analytical	45.23 mm	126.47 mm	81.24 mm
Experiment	~ 45 mm	~ 121 mm	~ 76 mm

After 4810 runs, the optimization algorithm with the new modulus of rigidity reached convergence, and the results are presented in table 5.9.

Table 5.9 Results after the convergence of the optimization.

Textile	d [mm]	D [mm]	N [-]	δtextile_h	δtextile_l	S [mm]	Stroke/L0
RIB10_PET1	2	25.4	30	180%	75%	97	131%

The analytical result shows that it is possible to achieve a stroke above 100% of the original length of the textile.

5.3.3 DISCUSSION

The model was validated by changing the modulus of rigidity of the spring to 3600 MPa. This value is plausible only when the shape memory alloy contains copper (Yamauchi, et al., 2011). However, this property is influenced by many parameters, such as composition, training temperature, and manufacturing technique.

However, assuming these values are plausible if the spring is ordered from the same manufacturer, the script produced promising results regarding the system's stroke. The system did not meet the 200% benchmark, but this can be attributed to the textile side, which cannot deform and spring back enough.

5.4 SUMMARY

In this chapter, the mechanical design of the counterAKT system was presented. Even though the system did not achieve the 200% benchmark, the results regarding the system's stroke are promising. However, more work can be done on the textile and spring sides to deliver a complete working system.

For what concerns the textile, research should look into the following:

- Varying the architecture of the knit parameters such as number, type, and resting length of elastic threads in designs similar to the ones in group three to achieve more deformation without losing the spring back force;
- Varying the parameters in the PES architecture of the knit (rows between the bed switch, amount of needles used for a single rib, number, and material of threads) and understand their influence on the overall performance;
- Finding ways to inlay the elastic during production in the ALT design and tension it in the RIB one;
- Studying ways to reduce the friction between the fabric and the metal guides in the LLG scenario, as this could bring benefit to the recovery capability of the system;
- Understanding and characterizing bigger scale models as the size of the specimen has been identified to be a determining factor in the latter's performance.
- SMA research instead should focus on the following:
- Determining the properties of SMAs a priori, without the need for mechanical testing and validation;
- Standardizing ways of production to deliver products with similar characteristics with properties available to the designers;

However, for what concerns the counterAKT system, further research should look into the interaction between the two elements and combine the findings of both materials to end with a fully working system.

THERMAL BEHAVIOR

This chapter aims to answer the last sub-research question:

"What are the primary factors influencing the temperature of the SMA spring?"

This chapter presents the thermal characterization of the shading - SMA spring system in cooling season. Section 1 introduces the methodology adopted. Section 2 presents the results from the analysis, while section 3 discusses them. Finally, section 4 summarizes and concludes the chapter.

6.1 METHODOLOGY

As the primary goal of a sunshade is to reduce solar gains, the system's efficiency is tested during a summer day characterized by high levels of solar radiation. Specifically, considered as the summer day with the highest peak of solar radiation This means analyzing the SMA spring's temperature and the latter's drivers.

Figure 6.1 presents the flowchart for the methodology used in this chapter.

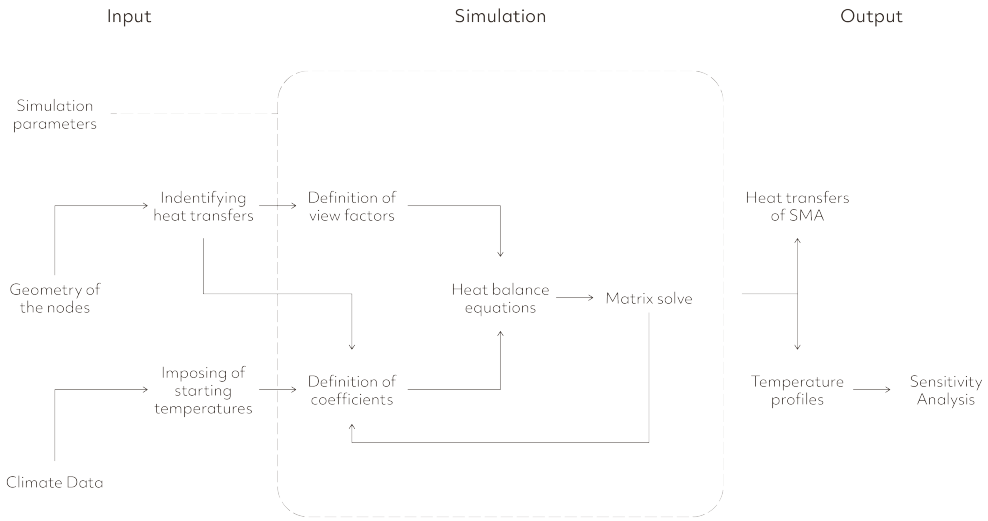

Figure 6.1 Workflow followed for the thermal analysis.

First, the simulation parameters such as the timestep and the number of hours to analyze is specified. The geometry of the nodes is set and the heat transfers between them are identified. The climate data is then loaded and duplicated based on the timestep selected. Every node is imposed with starting temperature equal to the first air temperature given by the weather file.

The simulation calculates the view factors and the heat transfer coefficients and builds the equations based on them. It then solves for the temperature of each node.

With the temperature of each node it is possible to calculate and plot the temperature profiles over the timespan selected and the heat transfers involved at every timestep. From the temperature profile of the SMA spring a sensitivity analysis is then implemented.

The simulation was performed for a period of 10 hours (3:00 – 22:59) on a the 17th of July in Rotterdam (NL). The hourly weather data was taken from the Typical Meteorological Year for Rotterdam (Climate.OneBuilding., 2023). The weather file comprised air temperature, solar radiation on the South façade, wind speed, downward longwave radiation, and global horizontal radiation. For this data refer to appendix B. The analysis was carried out by using timesteps of 15 minutes, therefore the weather data was considered constant throughout the same hour.

Five major assumptions were made to simplify the real-life situation and create the thermal model, as previously shown in figure 5.1. In particular, the first assumption was to model the system with two states: open state (SMA is in its martensitic phase) shown in figure 6.2A, and a closed state (SMA is in its austenitic phase) as show in figure 6.2B.

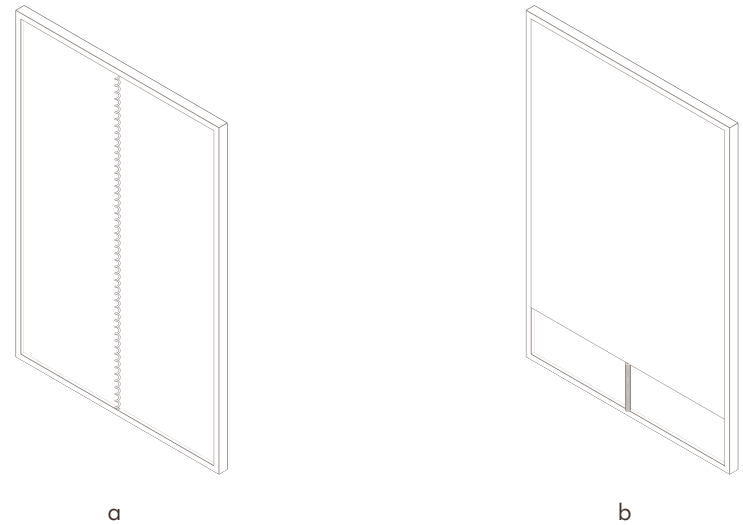

Figure 6.2 Two states of the counterAKT system. a) Inactive, fully open; b) Active, closed.

This assumption holds in the case that the system works as an ideal one. This implies that the fabrics is completely raise by the action of the elastic inlay, with the open state providing a clear, unobstructed view of the outside. As shown in chapter 5, this is npt the case in the current design. Furthermore, this assumption implies that the system is not subject to temperature hysteresis, instead, the SMA's rigidity modulus is assumed to be a step function of temperature (figure 6.3).

Another assumption made concerns the geometry of the SMA spring. To simplify the

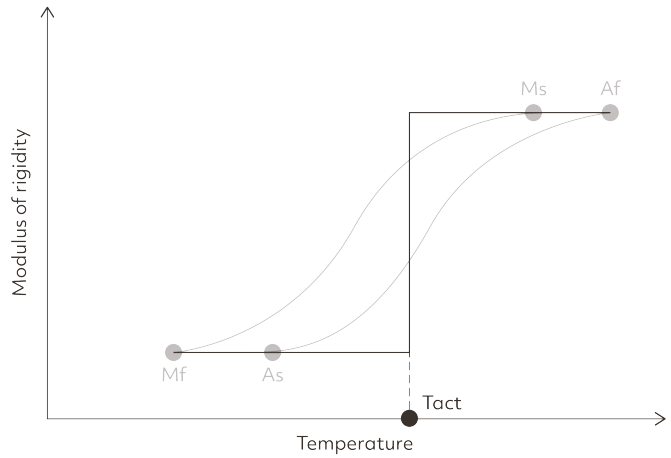

Figure 6.3 Assumption on the stiffness of the SMA spring. The four transformation temperatures explained in chapter 2.3 become one activation temperature named Tact.

modeling regarding view factors and heat transfer coefficients, the spring has been modeled as a hollow cylinder with an external radius equal to the coil radius and an inner radius equal to the coil radius minus the wire diameter. The length of the cylinder is set to the length of the spring (figure 6.4).

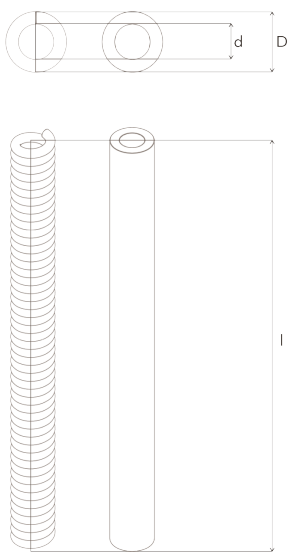

Figure 6.4 Assumption on geometry of the spring, modelled as a hollow cylinder.

Furthermore, the window frame has not been considered as it was deemed to not play a significant role in the heat transfers of the spring. The thermal network of the two states and the assumed geometries is represented in figure 6.5.

All the heat transfer coefficients that required a temperature difference (ΔT) in their formula have been calculated with an explicit method, which means that the ΔT at a specific timestep t was calculated with the temperatures at the previous timestep (t-1). Together with this, the radiation with the outside environment was calculated according to Zhao et al., (2023) with this method.

The explicit method is favored for its ease of implementation as it takes into account the previous timestep, whereas the implicit method focuses on the subsequent one. However, the explicit method can lead to instability if the timestep is not selected small enough since it doesn't account for the future state's influence, causing errors to accumulate rapidly and lead to numerical instability (Patankar, 1980). Please refer to appendix B for the calculation of the radiative and convective heat transfer coefficients, the dimensions of the objects of the nodes, the constants assumed, the sky and ambient equivalent temperature, and the view factors adopted in this model.

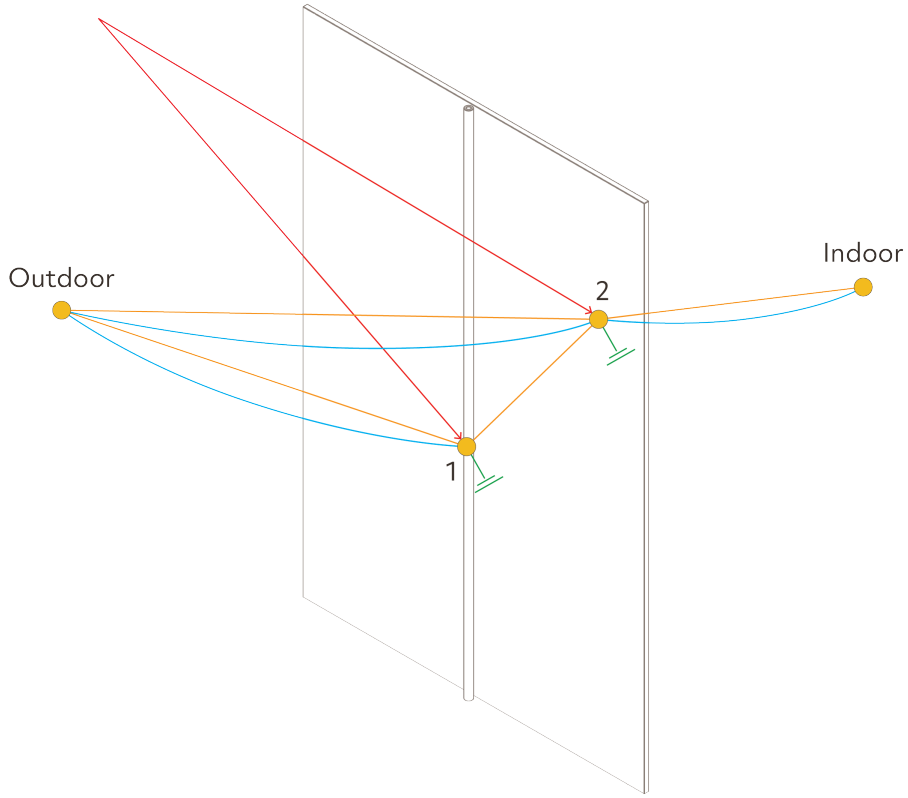

Solar radiation

Radiation

Convection

Accumulation

a

Figure 6.5 Modelled geometries and thermal networks. a) 3D of fully open state.

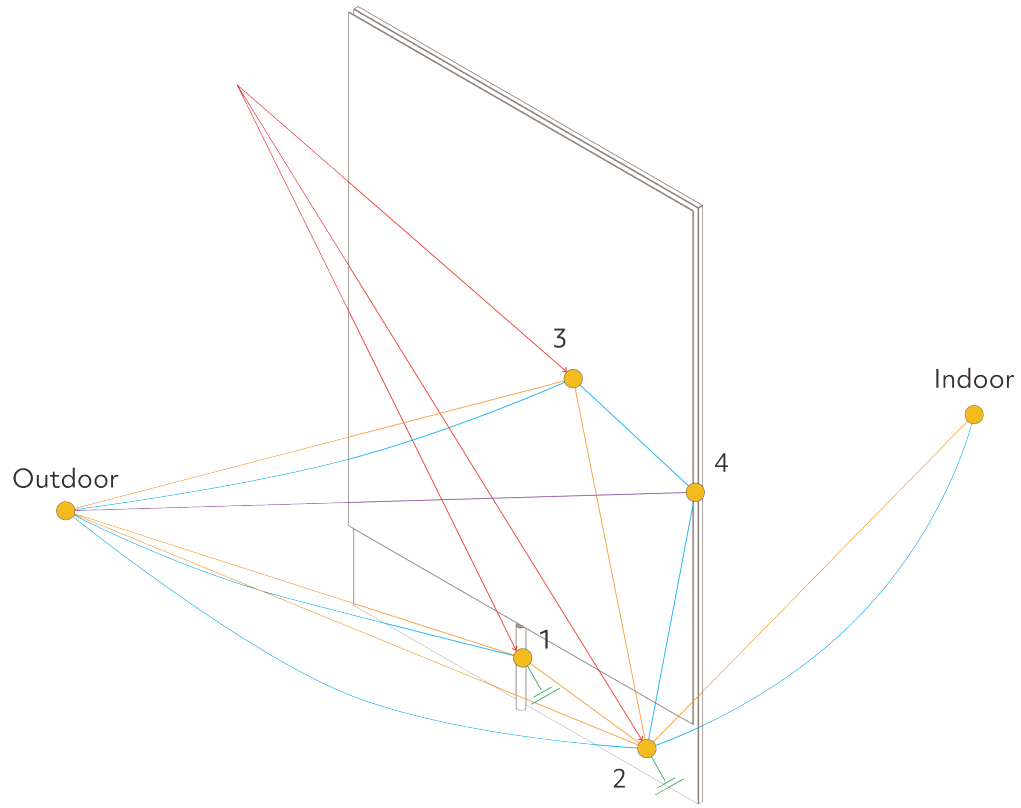

Solar radiation

Radiation

Convection

Accumulation

Advection

b

Figure 6.5 Modelled geometries and thermal networks. b) 3D of closed state.

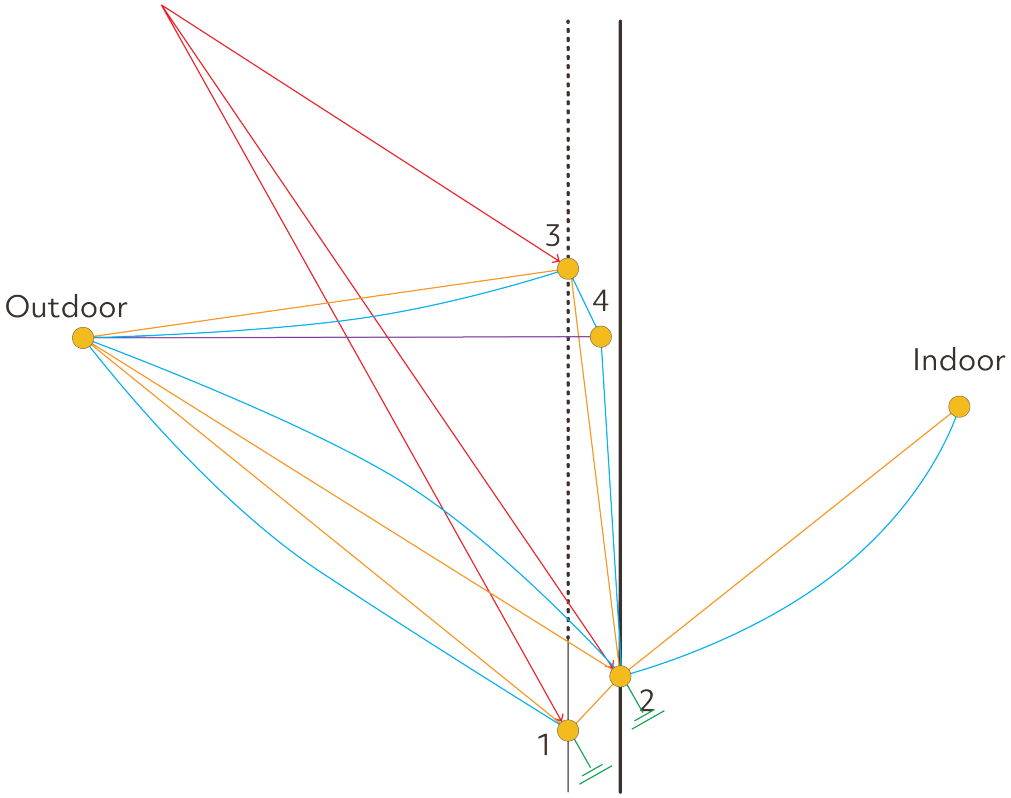

Figure 6.5 Modelled geometries and thermal networks. c) 2D of closed state.

6.1.1 DESCRIPTION OF THE THERMAL MODEL:

The symbols, their meaning, and their unit used in the following equations are listed in table 6.1.

Table 6.1 Meaning and unit of the symbols used in equations 6.1-38

Symbol	Meaning	Unit
Q	Heat	W
α	Heat transfer coefficient	W/m²K
A	Surface area	m2
T_i	Temperature of node i	K
σ	Stefan-Boltzmann constant	W/m²K⁴
ε	Emissivity	-
$F_{i\text{-}j}$	View factor from node i to node j	-
Qz	Solar radiation	W/m²
m	Mass	kg
Cp	Specific heat capacity	W/kgK
ρ	Density	kg/m³
V	Volumetric flow rate	m³/s
M	Solving matrix	W/K
B	Known vector	W

Node 1 – SMA spring

Figure 6.6a-b show the SMA spring's thermal network.

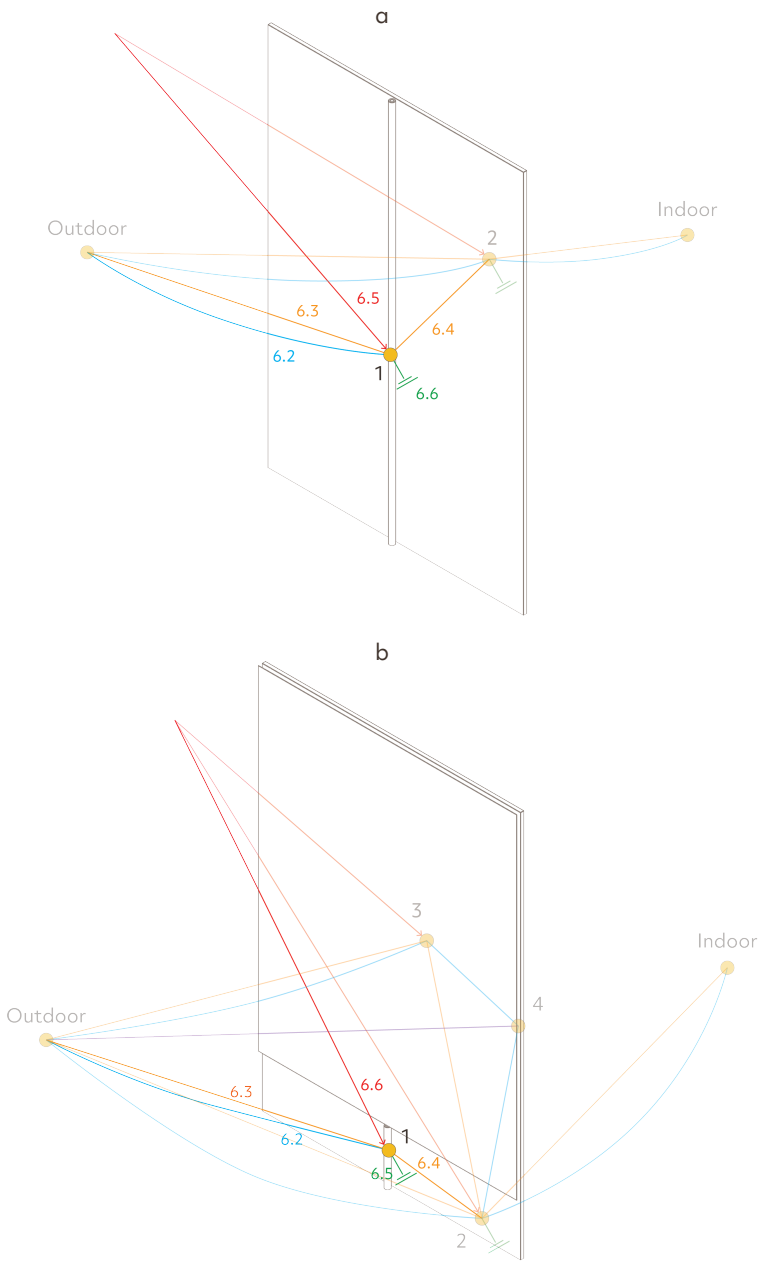

Figure 6.6 SMA spring's thermal network. a) Open state; b) Closed state.

The thermal balance for the SMA spring in both states is governed by the following equation:

(eq. 6.1) $$Q_{convection\_outside} + Q_{radiation\_outside} + Q_{radiation\_glazing} + Q_{solar} = Q_{accumulation}$$

Where:

$Q_{convection\_outside}$ is the heat transfer by convection with the outside air calculated using:

(eq. 6.2) $$Q_{convection\_outside} = \alpha_{conv\_spring} * A_{spring} * (T_o - T_1) \quad [W]$$

$Q_{radiation\_outside}$ is the heat transfer by radiation with the outside environment calculated using:

(eq. 6.3) $$Q_{radiation\_outside} = \sigma * \varepsilon_1 \left(F_{1-sky} \left(T_{sky}^4 - T_1^4 \right) + \left(1 - F_{1-sky} \right) \left(T_{ae}^4 - T_1^4 \right) \right) * A_{spring} \quad [W]$$

$Q_{radiation\_glazing}$ is the heat transfer by radiation with the glazing calculated using:

(eq. 6.4) $$Q_{radiation\_glazing} = \alpha_{rad\_spring\_glazing} * A_{spring} * F_{1-2} * (T_2 - T_1) \quad [W]$$

Q_{solar} is the heat transfer by solar radiation calculated using:

(eq. 6.5) $$Q_{solar} = \varepsilon_{spring} * A_{spring} * F_{1-outside} * Q_z \quad [W]$$

$Q_{accumulation}$ is the accumulated heat calculated using:

(eq. 6.6) $$Q_{accumulation} = m * C_p * (T_1^t - T_1^{t-1})/dt \quad [W]$$

α_{conv_spring} has been calculated for natural and forced convection due to wind, and then the highest number has been taken as the coefficient as it would represent the worst-case scenario. This is because the system's goal is to be activated by solar radiation and not be driven by the outdoor temperature.

Node 2 – glazing

The thermal balance for the glazing changed from the low temperature (figure 6.7.a) to the high temperature (figure 6.7.b-c) stage.

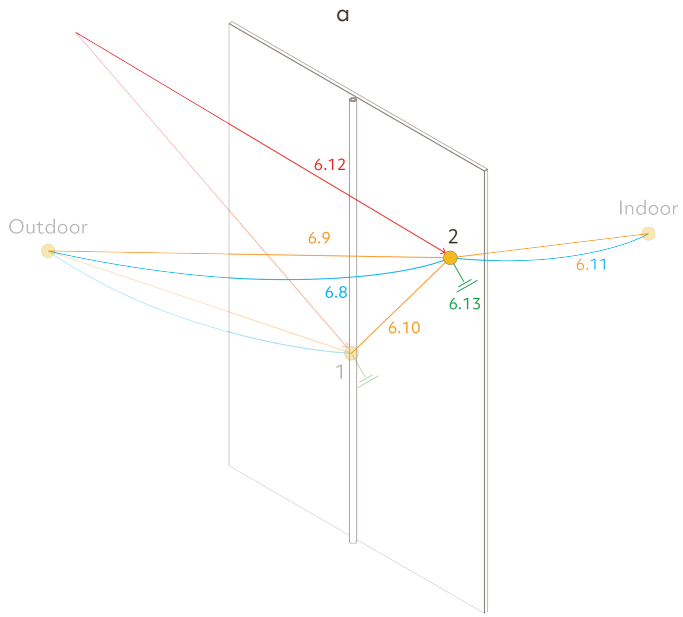

Figure 6.7 Glazing's thermal network. a) Open state.

In the open state, it was governed by the equation:

(eq. 6.7)
$$Q_{convection\_outside} + Q_{radiation\_outside} + Q_{radiation\_spring} + Q_{convection\_radiation\_inside} + Q_{solar} = Q_{accumulation}$$

Where:

$Q_{convection\_outside}$ is the heat transfer by convection with the outside air calculated using:

(eq. 6.8)
$$Q_{convection\_outside} = \alpha_{conv\_flat} * A_{glazing} * (T_o - T_2) \quad [W]$$

$Q_{radiation\_outside}$ is the heat transfer by radiation with the outside environment calculated using:

(eq. 6.9)
$$Q_{radiation\_outside} = \sigma * \varepsilon_2 \left(F_{2-sky} \left(T_{sky}^4 - T_2^4 \right) + \left(1 - F_{2-sky} \right) \left(T_{ae}^4 - T_2^4 \right) \right) * A_{glazing} \quad [W]$$

$Q_{radiation\_spring}$ is the heat transfer by radiation with the glazing calculated using:

(eq. 6.10)
$$Q_{radiation\_spring} = \alpha_{rad\_spring\_glazing} * A_{glazing} * F_{2-1} * (T_1 - T_2) \quad [W]$$

$Q_{convection\_radiation\_inside}$ is the heat transfer by radiation with the glazing calculated using:

(eq. 6.11)
$$Q_{convection\_radiation\_inside} = \alpha_{inside} * A_{glazing} * (T_i - T_2) \quad [W]$$

Q_{solar} is the heat transfer by solar radiation calculated using:

(eq. 6.12)
$$Q_{solar} = \varepsilon_{glazing} * A_{glazing} * F_{2-outside} * Q_z \quad [W]$$

$Q_{accumulation}$ is the accumulated heat calculated using:

(eq. 6.13)
$$Q_{accumulation} = m * C_p * (T_2^t - T_2^{t-1})/dt \quad [W]$$

Figure 6.7 Glazing's thermal network. b) 3D of Closed state; c) 2D of closed state

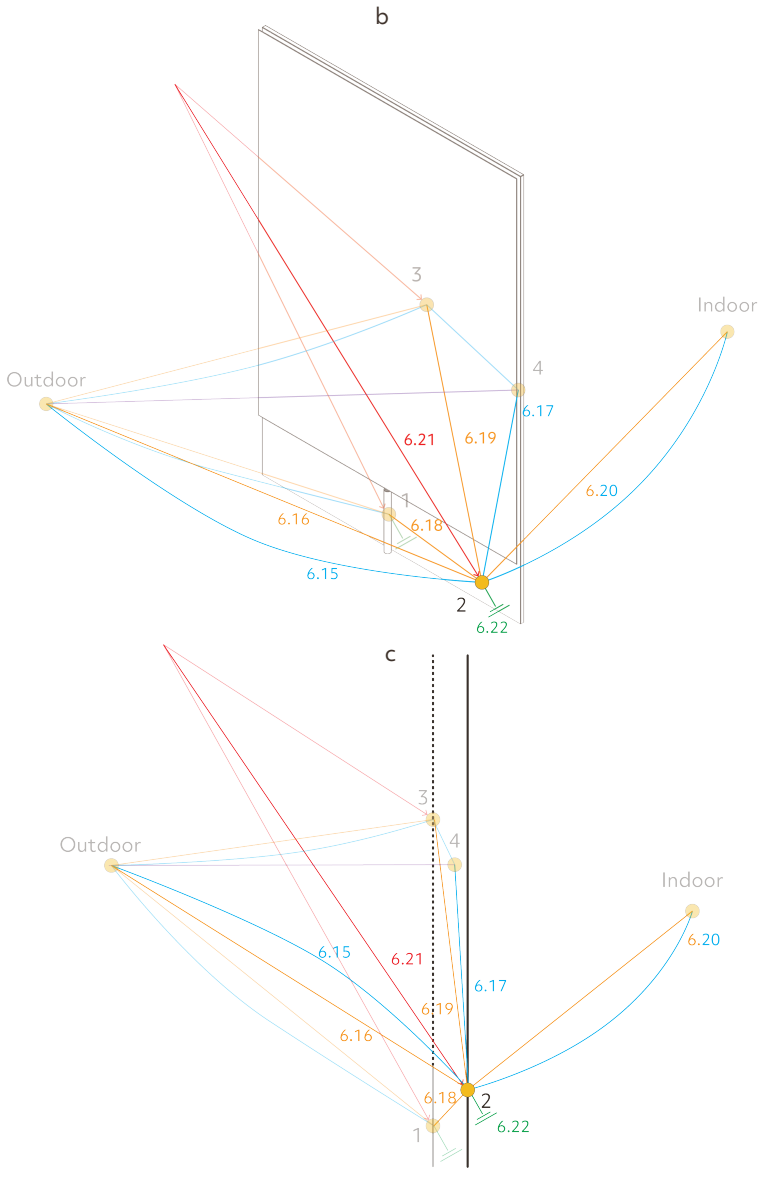

In the activated state with the blind down, the governing formula was:

$$Q_{convection\_outside} + Q_{radiation\_outside} + Q_{convection\_cavity} + Q_{radiation\_spring} + Q_{radiation\_textile} + Q_{convection\_radiation\_inside} + Q_{solar} = Q_{accumulation} \quad \text{(eq. 6.14)}$$

Where:

$Q_{convection\_outside}$ is the heat transfer by convection with the outside air calculated using:

$$Q_{convection\_outside} = \alpha_{conv\_flat} * A_{glazing}^{uncovered} * (T_o - T_2) \quad [W] \quad \text{(eq. 6.15)}$$

$Q_{radiation\_outside}$ is the heat transfer by radiation with the outside environment calculated using:

$$Q_{radiation\_outside} = \sigma * \varepsilon_1 \left(F_{2-sky} \left(T_{sky}^4 - T_1^4 \right) + \left(1 - F_{2-sky} \right) \left(T_{ae}^4 - T_1^4 \right) \right) * A_{glazing}^{uncovered} \quad [W] \quad \text{(eq. 6.16)}$$

$Q_{convection\_cavity}$ is the heat transfer by convection with the cavity air calculated using:

$$Q_{convection\_cavity} = \alpha_{conv\_cavity\_glazing} * A_{glazing}^{covered} * (T_4 - T_2) \; [W] \quad \text{(eq. 6.17)}$$

$Q_{radiation\_spring}$ is the heat transfer by radiation with the glazing calculated using:

$$Q_{radiation\_spring} = \alpha_{rad\_spring\_glazing} * A_{glazing}^{uncovered} * F_{2-1} * (T_1 - T_2) \quad [W] \quad \text{(eq. 6.18)}$$

$Q_{radiation\_textile}$ is the heat transfer by radiation with the outside environment calculated using:

$$Q_{radiation\_textile} = \alpha_{rad\_textile\_glazing} * A_{glazing}^{covered} * F_{2-3} * (T_3 - T_2) \; [W] \quad \text{(eq. 6.19)}$$

$Q_{convection\_radiation\_inside}$ is the heat transfer by radiation with the glazing calculated using:

$$Q_{convection\_radiation\_inside} = \alpha_{inside} * A_{glazing} * (T_i - T_2) \quad [W] \quad \text{(eq. 6.20)}$$

Q_{solar} is the heat transfer by solar radiation calculated using:

$$Q_{solar} = \varepsilon_{glazing} * A_{glazing}^{uncovered} F_{2-outside} * Q_z + \varepsilon_{glazing} * A_{glazing}^{covered} F_{3-2} * f_{textile} * Q_z \quad [W] \quad \text{(eq. 6.21)}$$

$Q_{accumulation}$ is the accumulated heat calculated using:

$$Q_{accumulation} = m * C_p * (T_2^t - T_2^{t-1})/dt \quad [W] \quad \text{(eq. 6.22)}$$

In this last set of equations, the area of the glazing has been divided into a covered area and an uncovered one. The former was set equal to the area of the textile as it is the portion that does not face the outdoors immediately.

Node 3 – Textile

Figure 6.8a-b show the textile's thermal network.

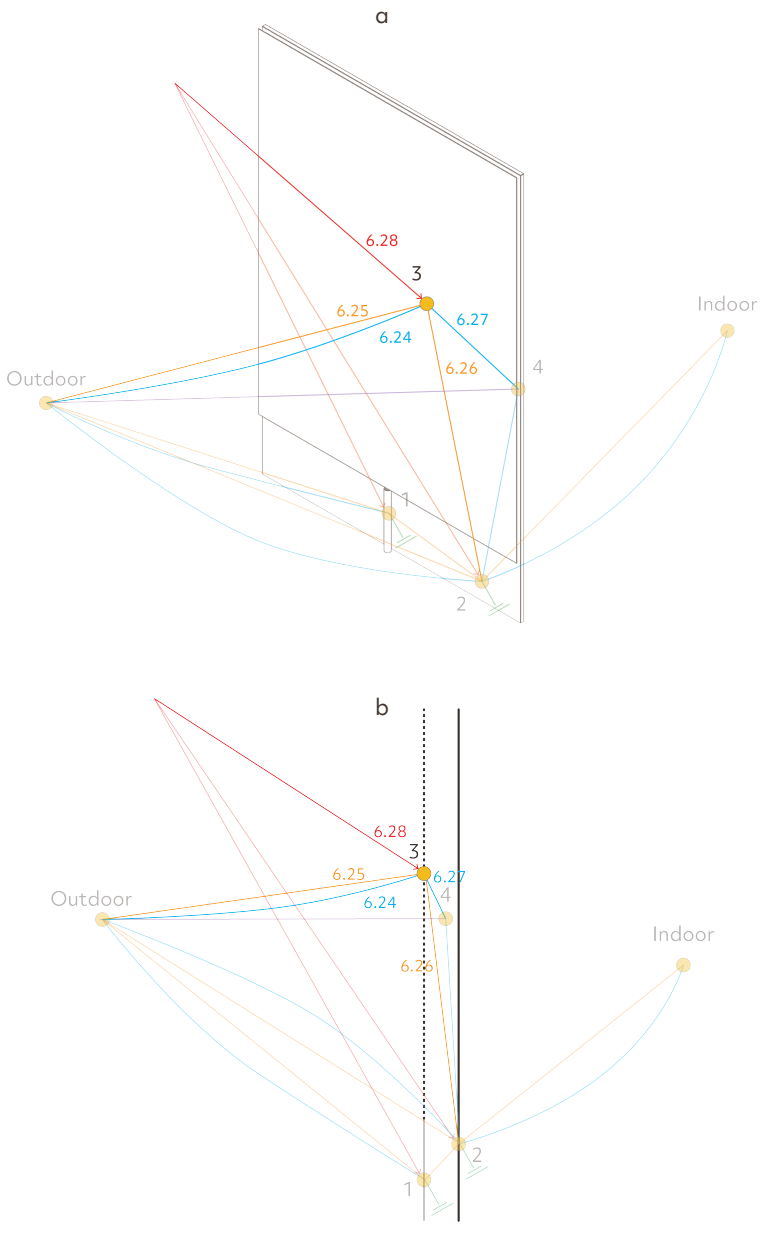

Figure 6.8 Textile's thermal network. a) 3D view; b) 2D view

The thermal balance for the textile was only considered for the closed stage and was governed by the following:

(eq. 6.23) $$Q_{convection\_outside} + Q_{radiation\_outside} + Q_{radiation\_glazing} + Q_{convection\_cavity} + Q_{solar} = 0$$

Where

$Q_{convection\_outside}$ is the heat transfer by convection with the outside air calculated using:

(eq. 6.24) $$Q_{convection\_outside} = \alpha_{conv\_flat} * A_{textile} * (T_o - T_3) \quad [W]$$

$Q_{radiation\_outside}$ is the heat transfer by radiation with the outside environment calculated using:

(eq. 6.25) $$Q_{radiation\_outside} = \sigma * \varepsilon_3 \left(F_{3-sky} \left(T_{sky}^4 - T_3^4 \right) + \left(1 - F_{3-sky} \right) \left(T_{ae}^4 - T_3^4 \right) \right) * A_{textile} \quad [W]$$

$Q_{radiation\_glazing}$ is the heat transfer by radiation with the glazing calculated using:

(eq. 6.26) $$Q_{radiation\_glazing} = \alpha_{rad\_textile\_glazing} * A_{textile} * F_{3-2} * (T_2 - T_3) \quad [W]$$

$Q_{convection\_cavity}$ is the heat transfer by convection with the cavity air calculated using:

(eq. 6.27) $$Q_{convection\_cavity} = \alpha_{conv\_textile\_cavity} * A_{textile} * (T_4 - T_3) \quad [W]$$

Q_{solar} is the heat transfer by solar radiation calculated using:

(eq. 6.28) $$Q_{solar} = \varepsilon_{spring} * A_{spring} * Q_z \quad [W]$$

Node 4 – Cavity

Figure 6.9a-b show the cavity's thermal network.

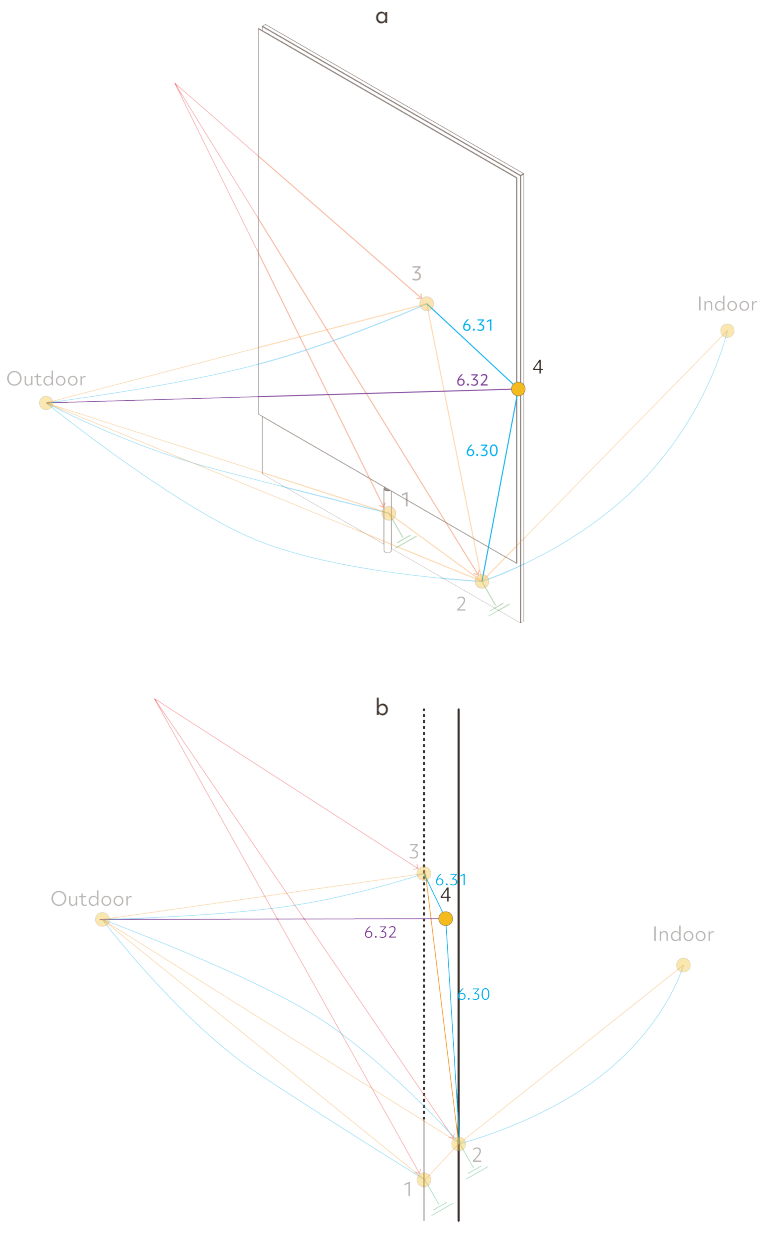

Figure 6.9 Cavity's thermal network. a) 3D view; b) 2D view

The thermal balance for the cavity was only considered for the closed stage and was governed by the following:

(eq. 6.29)

$$Q_{convection\_glazing} + Q_{convection\_textile} + Q_{advection} = 0$$

Where

$Q_{convection\_glazing}$ is the heat transfer by convection with the glazing calculated using:

(eq. 6.30)

$$Q_{convection\_glazing} = \alpha_{conv\_glazing\_cavity} * A_{glazing} * (T_2 - T_4)\ [W]$$

$Q_{convection\_textile}$ is the heat transfer by convection with the textile calculated using:

(eq. 6.31)

$$Q_{convection\_textile} = \alpha_{conv\_glazing\_textile} * A_{textile} * (T_3 - T_4)\ [W]$$

$Q_{advection}$ is the heat transfer by advection with the outside air calculated using:

(eq. 6.32)

$$Q_{advection} = \rho_{air} * \dot{V}_{air} * Cp_{air} * (T_o - T_4)\ [W]$$

Governing equations

By combining the previously mentioned equations in each node we obtain:

Node 1 – SMA spring

$$\alpha_{conv\_spring} * A_{spring} * (T_o - T_1) + \sigma * \varepsilon_1 \left(F_{1-sky}(T_{sky}^4 - T_1^4) + (1 - F_{1-sky})(T_{ae}^4 - T_1^4)\right) * A_{spring} + \alpha_{rad\_spring\_glazing} * A_{spring} * F_{1-2} * (T_2 - T_1) + \varepsilon_{spring} * A_{spring} * F_{1-outside} * Q_z = m_{spring} * Cp_{spring} * (T_1^t - T_1^{t-1})/dt \quad \text{(eq. 6.33)}$$

Node 2 – Glazing

$$\alpha_{conv\_flat} * A_{glazing}^{uncovered} * (T_o - T_2) + \sigma * \varepsilon_1 \left(F_{2-sky}(T_{sky}^4 - T_1^4) + (1 - F_{2-sky})(T_{ae}^4 - T_1^4)\right) * A_{glazing}^{uncovered} + \alpha_{conv\_cavity_{glazing}} * A_{glazing}^{covered} * (T_4 - T_2) + \alpha_{rad\_spring\_glazing} * A_{glazing}^{uncovered} * F_{2-1} * (T_1 - T_2) + \alpha_{rad\_textile_{glazing}} * A_{glazing}^{covered} * F_{2-3} * (T_3 - T_2) + \alpha_{inside} * A_{glazing} * (T_i - T_2) + \varepsilon_{glazing} * A_{glazing}^{uncovered} F_{2-outside} * Q_z + \varepsilon_{glazing} * A_{glazing}^{covered} F_{3-2} * f_{textile} * Q_z = m_{glazing} * Cp_{glazing} * (T_2^t - T_2^{t-1})/dt \quad \text{(eq. 6.34)}$$

Node 3 – Textile

$$\alpha_{conv\_flat} * A_{textile} * (T_o - T_3) + \sigma * \varepsilon_3 \left(F_{3-sky}(T_{sky}^4 - T_3^4) + (1 - F_{3-sky})(T_{ae}^4 - T_3^4)\right) * A_{textile} + \alpha_{rad\_textile\_glazing} * A_{textile} * F_{3-2} * (T_2 - T_3) + \alpha_{conv\_textile\_cavity} * A_{textile} * (T_4 - T_3) + \varepsilon_{textile} * A_{textile} * Q_z = 0 \quad \text{(eq. 6.35)}$$

Node 4 – Cavity

$$\alpha_{conv\_glazing\_cavity} * A_{glazing} * (T_2 - T_4) + \alpha_{conv\_glazing_{textile}} * A_{textile} * + \rho_{air} * \dot{V}_{air} * Cp_{air} * (T_o - T_4) = 0 \quad \text{(eq. 6.36)}$$

Rearranging these by expliciting the unknowns $T_{1\text{-}4}$ and putting them into matrix form, we obtain a system of the form:

$$M \cdot T = B \quad \text{(eq. 6.37)}$$

Solving now for T by using:

$$T = M^{-1} \cdot B \quad \text{(eq. 6.38)}$$

It is possible to retrieve the temperatures of the four nodes at a time t. With these new temperatures, the coefficients are calculated, and the procedure is repeated until the last timestep.

Note that the "full open" case is just a special case of the closed one. For the former, the matrix is a 2x2 with the revised equations. In this case, the textile temperature was imposed equal to the ambient equivalent temperature, and the cavity temperature was set equal to the outside air temperature.

Sensitivity analysis

Following this, two sensitivity analyses are implemented using the SAFE toolbox developed by Pianosi et al. (2015).

The first analysis is a Fourier Amplitude Sensitivity Test (FAST), which returns first-order sensitivity indexes. These represent the proportion of the total output variance attributable to a specific parameter. However, it does not capture potential interactions or nonlinear relationships between parameters.

The second analysis is the Elementary Effects Test (EET) which returns two values. The first is the mean of the elementary effects, which indicates a certain parameter's overall impact or influence on the model output. The second one is the variance of the elementary effects, which provides information about the consistency or stability of the impact across multiple evaluations of the model.

For both analyses, the input parameters are summarized in table 6.2. The mean temperature of the SMA during the analyzed period was taken as the output parameter to run the indexes.

Table 6.2 Parameters considered for the sensitivity analysis. Their range and distribution.

Parameter	Range	Distribution
SMA Emissivity	[0, 1]	Uniform
Textile Emissivity	[0, 1]	Uniform
Textile solar transmittance	[0, 1]	Uniform
Convective heat transfer coefficient of spring	[1.5, 60]	Uniform

6.2 RESULTS

Figures 6.10a-d show the heat transfers and the temperature profiles for an activation temperature of the SMA equal to 19°C and 20°C, respectively.

a

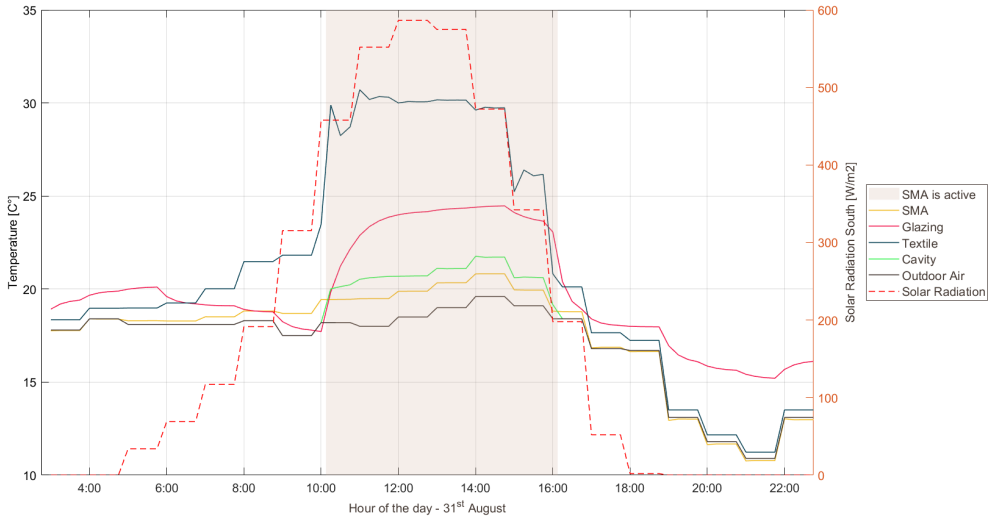

b

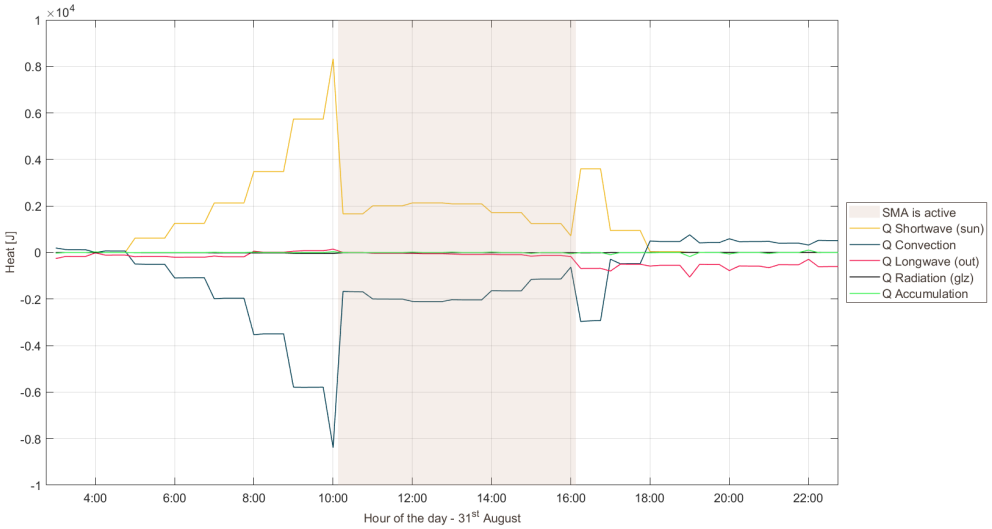

Figure 6.10 Thermal model results from the MatLab model. a) Temperature profiles when the SMA activation temperature is 19°C; b) Heat transfers when the SMA activation temperature is 19°C.

c

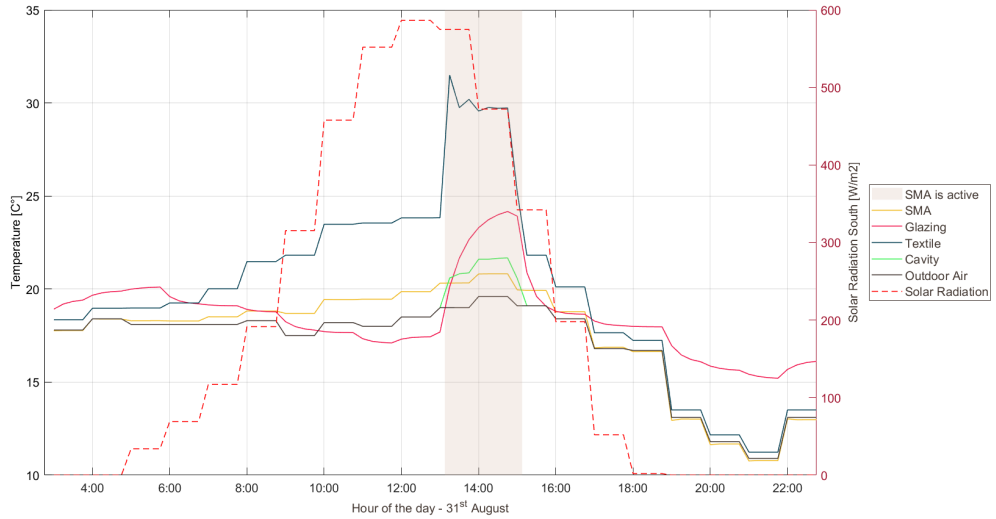

d

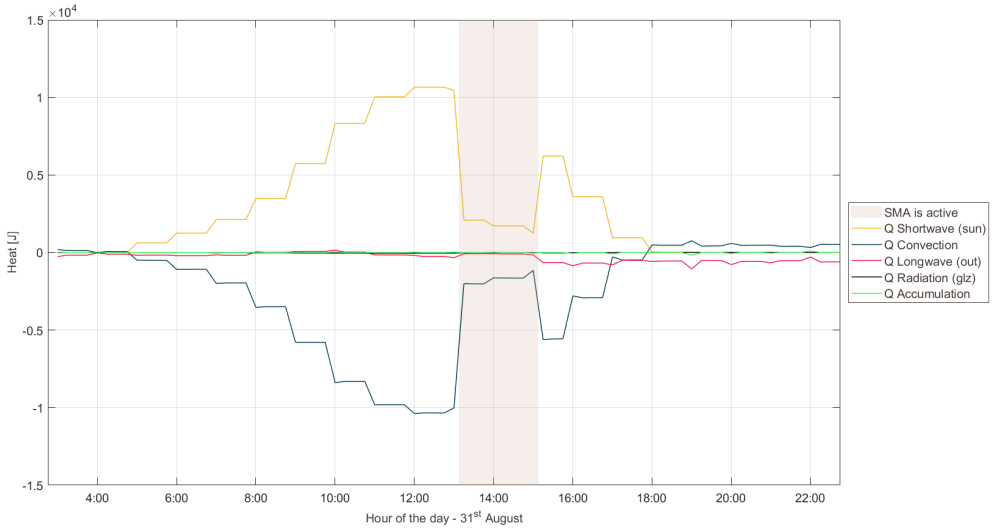

Figure 6.10 Thermal model results from the MatLab model. c) Temperature profiles when the SMA activation temperature is 20°C; d) Heat transfers when the SMA activation temperature is 20°C.

In both cases, the temperature of the SMA spring is just slightly higher than the outdoor air temperature over the whole analysis period. The difference between the two is the largest when the solar radiation reaches its peak. All nodes present profiles that look like step functions except for the glazing which is slightly delayed. Furthermore, the temperature of the glazing increases when the blind is closed. The cavity get slightly warmer compared to the outside air while the textile has the biggest increase in temperature when it is open. Solar radiation and convection to the outside are the most dominating heat transfers for the SMA. Meanwhile, the heat exchange by longwave radiation plays a small role during the day and a bigger one at night. Regarding the radiation with the glazing and the accumulation, the values are negligible (approximately equal to zero).

Figures 6.11a-d present the results of the FAST and EET analysis together with their convergence graphs.

The two analyses show similar results as the first-order sensitivity index from FAST, and the mean of the elementary effects from EET are not equal but comparable values. Both agree on the more significant impact of the convective heat transfer coefficient compared to that of the SMA emissivity. However, the EET also provided insight into the stability of the input parameters and their possible relation. It is observed that the variance for the convective heat transfer coefficient is much greater than the one for the SMA emissivity.

Figure 6.11 Results of the sensitivity analysis. a) First order sensitivity indexes from FAST; b) Convergence of FAST;c) Mean and variance of elementary effects from EET; d) Convergence of EET.

a

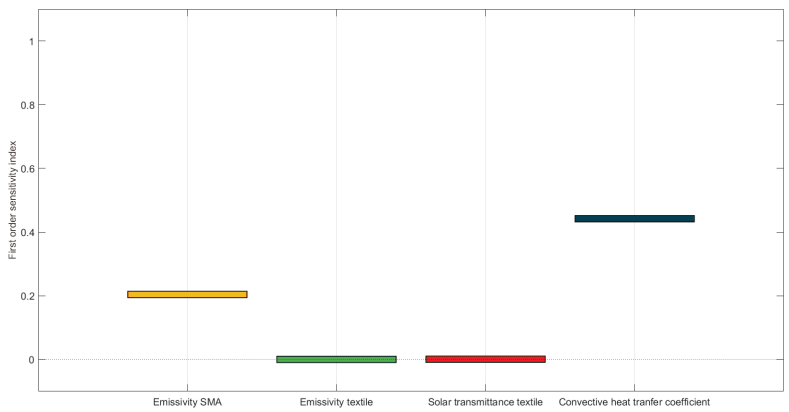

b

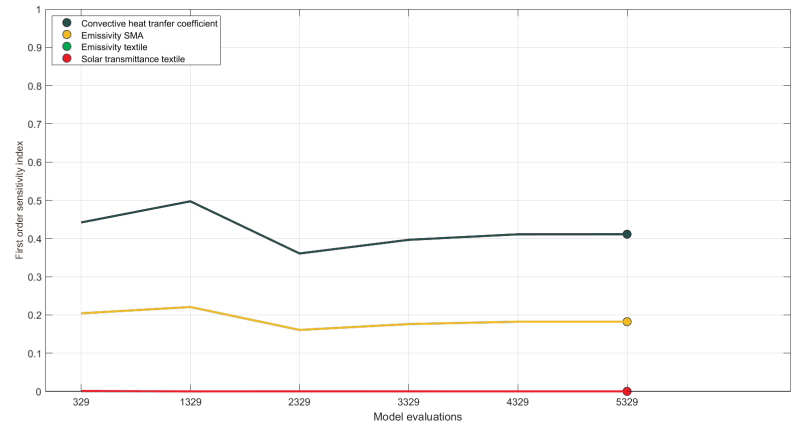

c

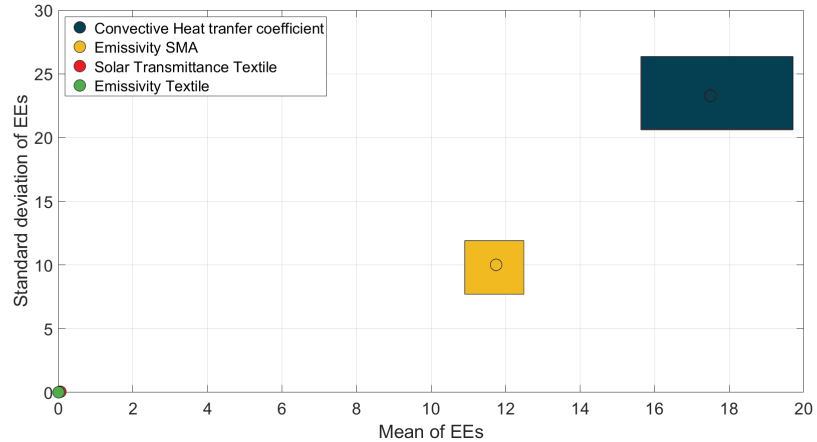

d

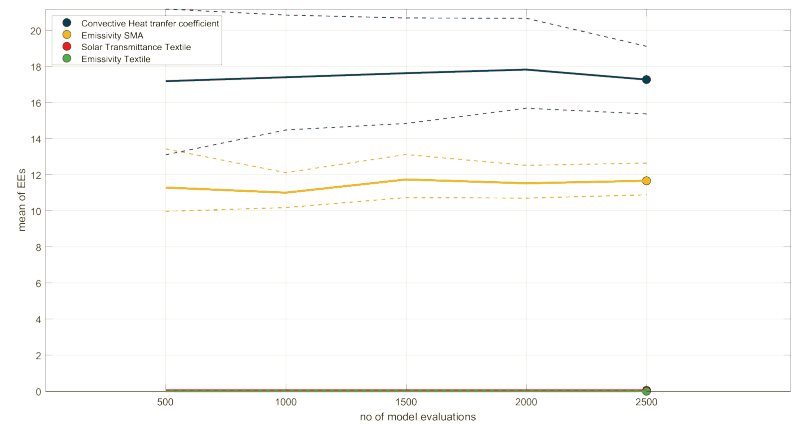

Moreover, both analyses agree on the minor importance of the textile's properties (emissivity and solar transmittance) on the temperature of the SMA spring. Finally, the convergence of both analyses shows stabilization, even though the EET one was faster.

6.3 DISCUSSION

The temperature profiles show credible results as the temperatures are within acceptable ranges. However, the slight difference in activation temperature between the two scenarios in figures 6.9a-d indicate that the system's performance differs significantly with a minimal change of activation temperature. This represents a challenge as it is difficult to calibrate the SMA with such precision as mentioned in section 2.3.

The glazing is the only node which temperatures do not follow a step function due to the accumulation component. Conversely, in the SMA, the mass is too low to produce observable results. Furthermore, when closed down, the temperature of the glazing rises. This is due to the heat transfer on the inside pane, which with an ambient with a temperature set to 24°C.

The SMA temperature profile is observed to follow the outdoor air temperature with a slight offset due to solar radiation. This is explained by the heat transfers in figure 6.9b/d and by the variance of the elementary effects. The heat transfer by solar radiation is a known term in the heat balance equations defined in section 6.1.1, while the convective heat transfer is calculated at each timestep to balance with the other terms. This explains the variance of the Elementary Effects of the two most influencing parameters. The low variance of the ones related to emissivity means that its effect is significant and consistent. On the contrary, as convection is not a known term, its effect depends on emissivity, hence the large variance.

6.4 CONCLUSION

Heat transfer analysis gave insight into which heat transfer plays the major role in determining the temperature of the SMA and which design parameters are the most important to consider when designing the counterAKT.

In the current state, the temperature of the SMA spring is influenced by solar radiation

and convection with the outside air the most. However, the temperature profiles show that the SMA temperature follows the profile of the outdoor air temperature while being slightly higher due to solar radiation. The most significant difference is given when the solar radiation peaks.

The sensitivity analysis confirms this result by ranking emissivity (which influences solar radiation) and the convective heat transfer coefficient as the most sensitive parameters. On the other hand, the sensitivity analysis shows that the temperature of the SMA is not sensitive to the properties of the textile. This allows for design freedom of the textile as the latter does not influence the temperature of the former.

However, in its current state, the counterAKT system depends more on the outdoor air temperature than on solar radiation. This barrier hinders the system's effectiveness. As shown in Section 4.2, systems that depend on outdoor temperature yield poorer outcomes than those triggered by solar radiation.

In conclusion, future research should look into ways to make the system dependent on solar radiation and not on outdoor air temperature. This could be done by:

- Increasing the emissivity of the SMA;
- Decreasing the heat lost by convection with the outside environment;
- Concentrating solar radiation on the spring.

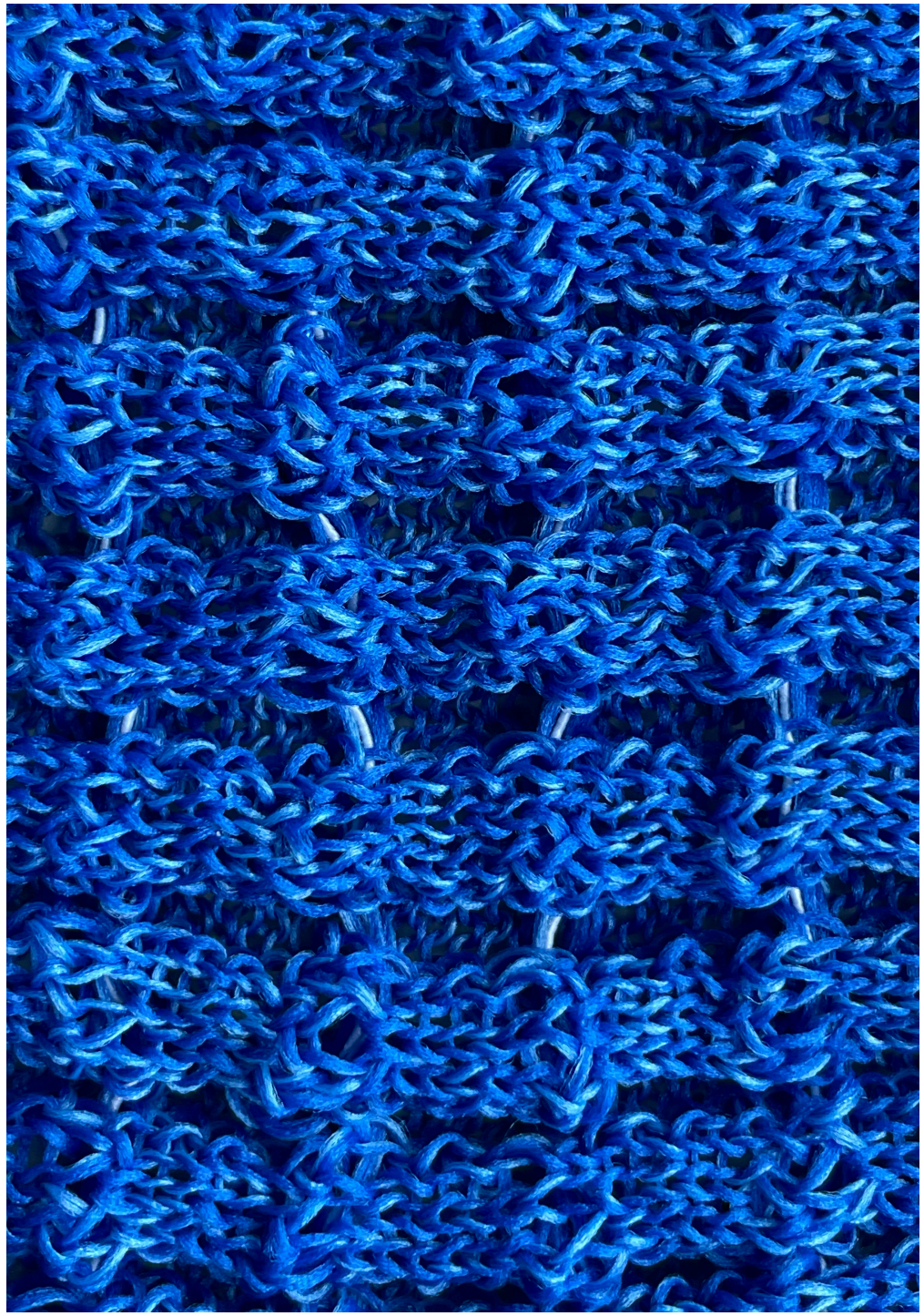

FUTURE DESIGNS

This chapter reflects on the conclusions drawn from the previous chapters and aims to give ideas for future designs that serve as possible solutions in the weaknesses found in the development of counterAKT. The three sections dive into possible design solutions inspired by real-life practice and examples.

Despite the promising results in terms of range of movement and reduction of mechanical complexity of the counterAKT, two major limitations have been identified within this study. In particular, the design did not achieve a sufficient range of movement to fulfill the need for contact with the exterior, and the temperature of the spring does not follow the ideal control strategy defined for an effective sunshade. While for the range of movement further research into knit architecture and SMA properties is needed, for the temperature of the spring the design should be improved significantly. This is due to the strong sensitivity of the SMA's temperature to the convective heat transfer coefficient. With this in mind, future designs should aim at increasing the system's dependence on solar radiation while limiting the number of extra components. In the following sections, concepts and designs worth exploring are presented.

7.1 WRAPPING OF THE SPRING

To increase the emissivity of the metal spring it would be possible to coat it with a black paint. This would therefore become hotter when sunlight hits it due to the increased solar gain. However, as the spring is in constant movement, painting it would cause the paint to chip off and become ineffective. Furthermore, the convective heat transfer would not be lowered. Wrapping the spring in a dark textile, for example, could lead to increased solar heat gain and lower heat loss due to convection.

Thanks to CNC knitting it would be possible to fabricate a stretchable pocket that accommodates the movement of the spring while enhancing its thermal behavior (figure 7.1).

However, the effectiveness of this approach remains to be tested, as the impact on emissivity enhancement and reduction in convective heat transfer coefficients may not be immediately apparent.

Figure 7.1 Pocket created to insert a wooden rod. The same geometry could be manufactured to create a pocket in which to insert the wire of the spring

7.2 ENCAPSULATION OF THE SPRING

Another approach solution would consist in encapsulating the spring in a container. This could improve performance as the air inside would be still and not cause as much heat loss from convection. The ideal design would be like a greenhouse or a solar panel, with a dark surface that can attract more solar radiation and increase the box's temperature while reducing the heat lost by convection with the outside environment. A preliminary scheme of such a system is presented in figure 7.2.

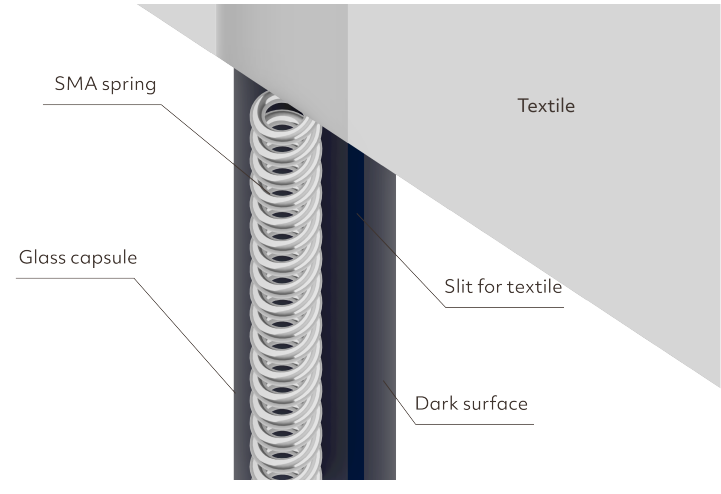

Figure 7.2 Scheme for encapsulating the SMA spring. The slit allows for the textile to move up and down while the dark surface absorbs solar radiation

As a preliminary study, the model presented in chapter 6 has been run with a convective heat transfer coefficient of 3.73 W/m2K which is typical for flat solar plate collector (Duffie & Beckman, 1991). In addition, the emissivity of the spring has been increased to 0.7 to take into account the amplification of the solar gains due to the dark surface behind the spring. The temperature profile and the heat transfers are presented in figure 7.3a-b.

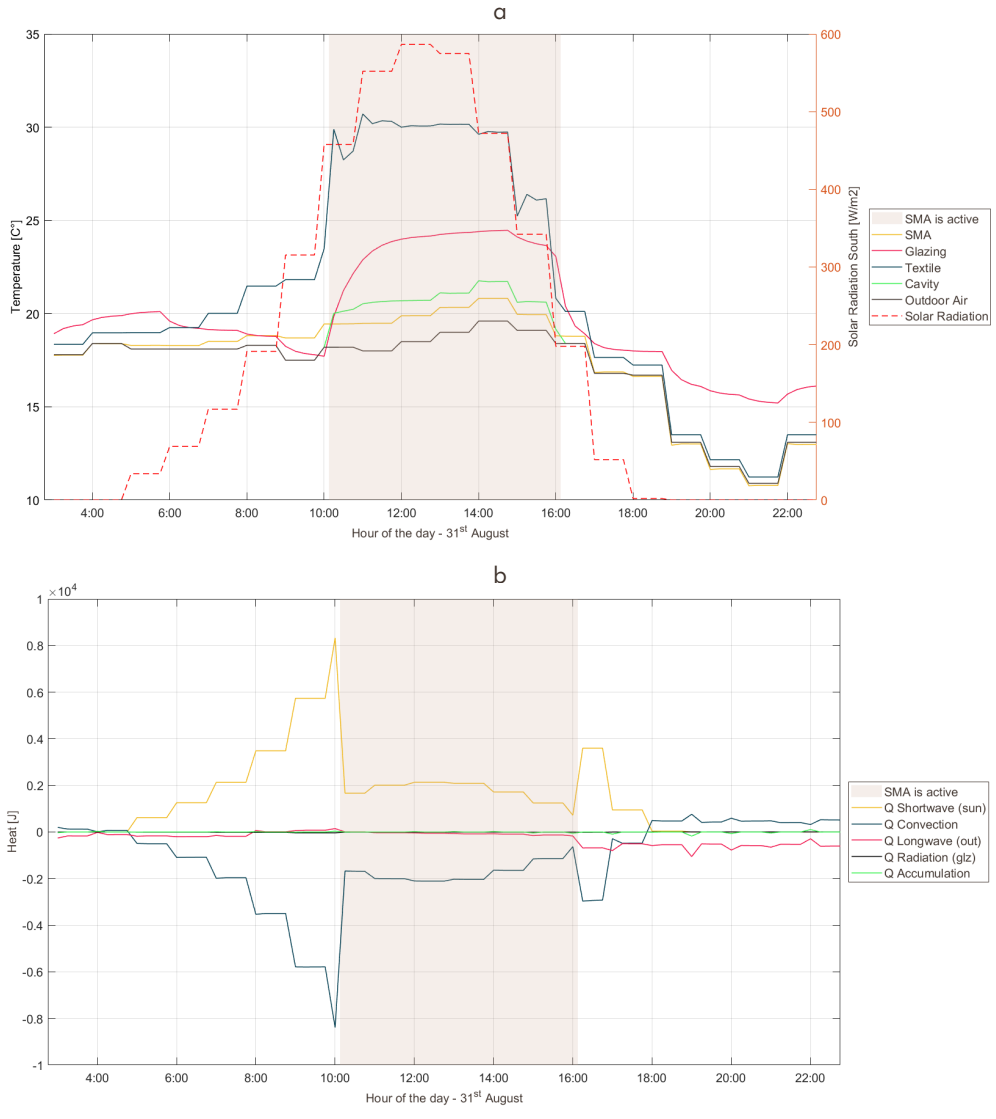

Figure 7.3 Results of the thermal model with the flat solar plate properties. a) Temperature profiles; b) Heat transfers on the SMA spring.

The temperature reached by the SMA spring is higher when compared to the results obtained in chapter 6. Furthermore, the spring now follows the curve of the solar radiation. The heat transfers show the higher contribution of the lost longwave radiation with the outside which might be mitigated by the glazing of the capsule which has not been taken into consideration. This preliminary study has been carried out by imposing variables found in literature but without changing the geometry of the nodes. Further studies are needed to account for the presence of the background dark surface, for the glazing capsule, and for the small gap needed to let the textile through the capsule.

7.3 SOLAR LENSES CONCENTRATION

In some buildings the glazing was placed in a way that would redirect the solar rays and concentrate the solar radiation on a certain spot. This concentration could melt part of cars (Lallanilla, 2013). Thanks to lenses or particularly designed glazing (figure 7.4) it would be possible to obtain a similar result onto the spring.

Such a system would increase the solar radiation falling onto the SMA and raise its temperature enough to trigger it. However, seeing the power of such systems raises concerns on their safety when applied so close to a façade. In particular, fire safety should be taken into account as well as the direction of the focus of the lenses.

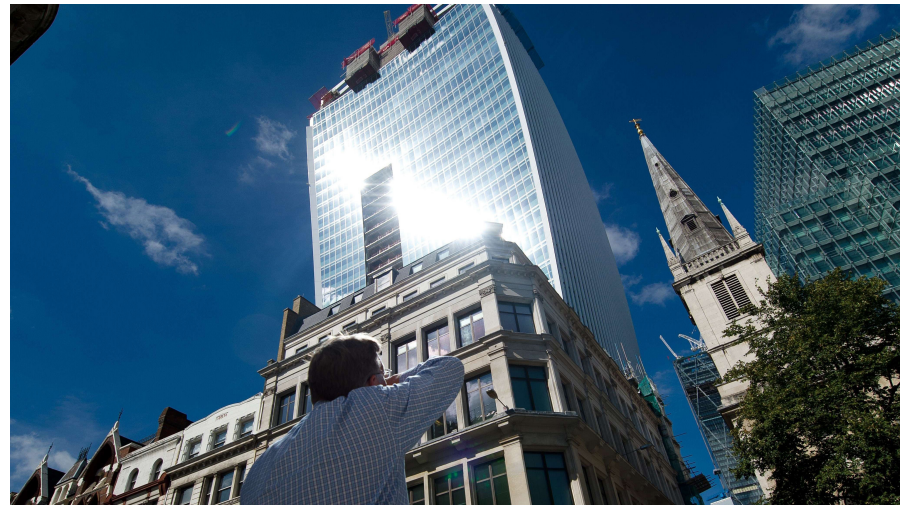

Figure 7.4 Curved glazing in a building that concentrates the solar radiation in a spot. The redirected radiation can increase the temperature and activate the SMA. (CNN, 2013)

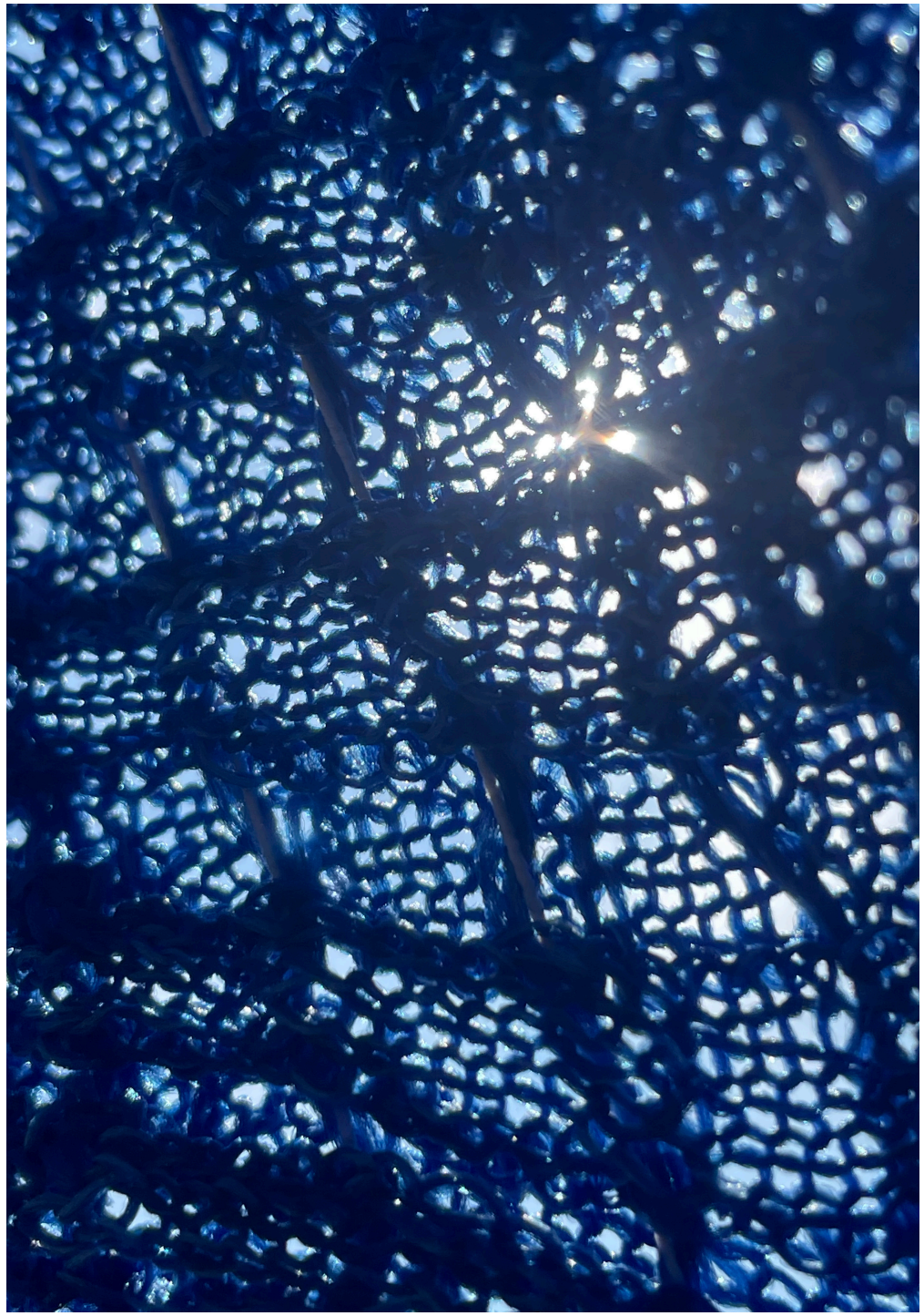

CONCLUSIONS

This thesis presented the design of a two-component passive dynamic sunshade that combines knitted textile and Shape Memory Alloys to reduce the mechanical complexity of adaptive façades. Chapters 1,2,3 provided the context, the current state-of-the-art of passive strategies, and the methods used within this work. Chapter 4 defined what an effective system is while providing guidelines on the benchmarks a passive dynamic sunshade should have. Chapter 5 presented the system's mechanical design, from the textile's characterization to the dimensioning of the SMA spring. Chapter 6 explained the system's thermal behavior and tested the effectiveness of the SMA actuator. Chapter 7 gave insight on possible future design solutions that aim at increasing the thermal efficiency of the system. Finally, this chapter summarizes the contribution of this thesis, discusses the advantages and limitations of the counterAKT system, and outlines possible future work.

8.1 CONTRIBUTIONS

This work contributes to the field of building physics and architectural engineering, in particular to that of adaptive façades research and development. The main research question:

"How can we combine knitted textile and shape memory alloys to create an effective passive dynamic sunshade?"

is now answered by collecting the conclusions from the sub-research questions in the following sections.

8.1.1 EFFECTIVENESS

In this work, chapter 4 concludes that a passive dynamic sunshade is effective when two conditions are met. First, it must comprise the least amount of components that have few interactions between them. Second, its performance enhances user satisfaction while lowering energy consumption. In this specific case, the ideal control strategy was defined for a typical office located in Rotterdam, NL. However, the thesis provided an approach to defining this strategy, which consisted of comparing the thermal, visual, and energy performance of different scenarios thanks to design optimization. In this specific case, the target was to maintain thermal comfort while reducing the cooling load and maximizing the opening hours of the shade to provide the user with contact with the exterior.

8.1.2 MECHANICAL DESIGN

With the aim of reducing complexity, the mechanical system of the counterAKT was explored in chapter 5. The designed system comprises only two components: an SMA spring that serves as sensor and actuator and a textile that provides shade and acts as the counteracting member. The feasibility of the design was demonstrated through mechanical testing and analytical calculations. The proposed design achieved a range of motion capable of covering less than half the window when deactivated. With more iterations on the knit architecture, it is possible to reach less covered area to leave the view unobstructed completely when unactive.

8.1.3 THERMAL BEHAVIOR

The thermal analysis performed in chapter 6 provided insight into the system's effectiveness in applying the ideal control strategy. The thermal analysis serves as a basis for future research as it can be reapplied to evaluate the performance of new iterations. In the current stage, the system does not follow the ideal control strategy and the design needs to be developed further as mentioned in chapter 7. However, thanks to the results of the sensitivity analysis, it was proven that the temperature of the SMA is not sensible to the properties of the textile. This result gives design freedom to the textile.

8.2 ADVANTAGES AND LIMITATIONS

The counterAKT system proved to be an effective solution for reducing mechanical complexity by reducing the number of components to two: a stretchable knitted textile that works as a biasing member and a SMA spring that acts as the sensor and the actuator for the system.

In terms of mechanical performance, even though the system did not meet the benchmark of 200% stroke, it showed promising results in achieving dynamicity. Particularly, the system was able to move for 130% of the initial length. More movement can be achieved with more iterations on the development of the textile. CNC knitting has been proven as a valid technique to produce testing specimens as it enables fast manufacturing of the knits. However, the best-performing specimens needed post-production tensioning to work which is a limit for serializing the system.

One of the system's main limitations regards SMA's properties. These are hard to predict and it post-production testing is needed to assess them. Not knowing the alloy's rigidity modulus makes the system depend on numerous mechanical tests to characterize the spring.

Another main advantage of the system is that the SMA is not sensitive to the properties of the textile, allowing designers to change the latter without influencing the system's behavior. However, the textile's properties still need to be measured or calculated. These are expected to affect the system's thermal performance, as shown in section 4.1. Moreover, due to the spring's temperature being more sensitive to the convective heat transfer coefficient rather than its emissivity, the ideal control strategy defined

in chapter 4 is not met, hindering the effectiveness of the system. Modeling the SMA without accounting for the fact that it transforms over a span of temperatures rather than on a specific set temperature is a limit of the study. However, in applications relying on high solar radiation, the simplified approach may still be suitable, as the temperatures reached exceed typical outdoor air temperatures. Furthermore, the temperature of the SMA does not seem to be affected whether it is in its martensitic or austenitic phase.

This thesis did not explore essential aspects needed to bring the system to a fully working product. In particular, the system was not tested for cycles of functioning (fatigue). This leaves an unknown on its durability. However, since it comprises only two components, its replaceability is deemed to be sufficiently simple. Since the system was assumed outside to raise its efficiency at reducing cooling loads, its capability to endure outside weather conditions is a crucial performance indicator that has not been considered within this work. Furthermore, this thesis explored small-scale experiments that should be scaled up to test whether the same conclusions hold for real-life applications.

Another aspect not addressed in this study pertains to user acceptance. It is important to conduct tests to gauge how occupants respond to the counterAKT system. Key areas for evaluation include user comfort with the interior color and the lack of control over sunshade activation. However, the latter issue is potentially resolvable. SMA technology can be activated using electrical current to facilitate sunshade deployment. As for sunshade retraction, a possible solution could involve employing a second, more robust SMA with electrical activation or integrating a switch mechanism. This switch could allow users to release tension in the system, leaving the glazing fully uncovered when desired.

Finally, this work focused on thermal comfort and visual contact with the exterior. However, a sunshade can perform more functions. As shown in section 4.1, a sunshade can for instance prevent from glare and enhance the daylight environment. These can be explored using a similar approach to the one explored within this thesis.

8.3 FUTURE WORK

In light of the discussions in section 8.2, future research directions can be outlined as follows: Firstly, examining the suitability of various control strategies across different

climates and geometries to assess their generalizability. Secondly, investigate ways to improve textile mechanical properties, particularly in terms of stretchability and spring-back response by iterating more on the specimens with different inlays properties. Additionally, developing methods for the production of tensioned textiles applicable to real-world scenarios is essential as it is unfeasible to post-tension each specimen. Furthermore, understand the thermal properties of textiles and optimize the knit architecture for enhanced thermal behavior. Standardization of Shape Memory Alloy (SMA) production methods to determine mechanical properties without extensive testing is crucial to avoid constant, time-consuming testing of the spring. Testing for durability, fatigue behavior, and full-scale model analysis to explore properties not covered in this study is also necessary. Furthermore, finding ways to characterize the system as temperature-dependent, rather than a step function, would be beneficial for the accuracy of both mechanical and thermal analyses. Lastly, exploring the potential for the system to depend on solar radiation rather than outdoor air temperature, as suggested in chapter 7, could offer improvements in practical applications

8.4 FINAL REMARKS

The essence of this research was to showcase that simple designs can be just as effective as those with complicated mechanical components. This approach ensures the system's durability and saves resources in the long run. By studying material's properties deeply and combining different fields, it was possible to achieve a working proof-of-concept to inspire future designers to focus more on often overlooked aspects such as maintenance and ease of use.

While the developed design aimed at ensuring thermal comfort and maintaining visual contact with the exterior, the knit has only been explored mechanically. However, since the elastic inlay provides mechanical performance, the PES part can be optimized for other comfort aspects.

Finally, with the almost infinite customization potential achievable thanks to CNC knitting, the possibilities designers can explore are practically endless and yet to be discovered.

BIBLIOGRAPHY

[1] Adsttc, 2023. [Online] Available at: https://images.adsttc.com/media/images/5227/c1a3/e8e4/4e5f/df00/000e/large_jpg/01-Stuttgart_303_Close-Up.jpg?1378337151 [Accessed 08 09 2023].

[2] Al-Masrani, S. M., Al-Obaidi, K. M., Zalin, N. A. & AIda Isma, M. I., 2018. Design optimisation of solar shading systems for tropical office buildings: Challenges and future trends. Solar Energy, Issue 170, pp. 849-872.

[3] ANSI/ASHRAE, 2007. Standard Method of Test for , Atlanta: American Society of Heating, Refrigerating and Air-Conditioning Engineers.

[4] Attia, S. et al., 2018. Current trends and future challenges in the performance assessment. Energy & Buildings 179, pp. 165-182.

[5] Attia, S., Lioure, R. & Declaude, Q., 2020. Future trends and main concepts of adaptive facade systems. Energy, Science & Engineering, pp. 3255-3272.

[6] Base Structures, 2023. [Online] Available at: https://www.basestructures.com/app/uploads/2021/09/ba100622_university_of_york-27-crop-1498x1000.jpg [Accessed 08 09 2323].

[7] Boetcher, S. K. S., 2014. Natural Convection from Cyrcular Cylinders. Daytona Beach: Springer.

[8] Böke, J., Denz, P.-R., Suwannapruk, N. & Vongsingha, P., 2022. Active, Passive and Cyber-Physical Adaptive Façade strategies: a Comparative Analysis Through Case Studies. Journal of Facade Design & Engineering, Volume 10.

[9] Boswell, C. K., 2013. Exterior Building Enclosures. Design Process and Composition for Innovative Facades. 1 ed. Hoboken: John Wiley & Sons.

[10] Boswell, C. K., 2013. Exterior Building Enclosures: Design Process and Composition for Innovative Facades. Hoboken: John Wiley & Sons.

[11] Bui, D.-K.et al., 2020. Enhancing building energy efficiency by adaptive façade: A computational optimization approach. Applied Energy, Issue 265.

[12] Building Green, 2023. [Online] Available at: https://www.buildinggreen.com/sites/default/files/live/images/04_207-14_LoRes.jpg [Accessed 08 09 2023].

[13] Cao, X. et al., 2020. Challenges and Opportunities toward Real Application of VO_2-Based Smart Glazing. Matter, Issue 2, pp. 862-881.

[14] Choi, K. F. & Lo, T. Y., 2003. An Energy Model of Plain Knitted Fabric. Textile Research , 73(8), pp. 739-748.

[15] Choi, K. F. & Lo, T. Y., 2006. The Shape and Dimensioning of Plain Knitted Fabric: A Fabric Mechanical Model. Textile Research Journal, 76(10), pp. 777-786.

[16] Churchill, S. W. & Bernstein, M., 1977. A Correlating Equation for Forced Convection From Gases and Liquids to a Circular Cylinder in Crossflow. Journal of Heat Transfer, Volume 99, p. 300–306.

[17] CIBSE, 2022. Monitoring indoor environmental quality, London: s.n.

[18] Climate.OneBuilding., 2023. Europe - Region 6. [Online] Available at: https://climate.onebuilding.org/WMO_Region_6_Europe/NLD_Netherlands/index.html [Accessed 06 09 2023`].

[19] Cloudfront, 2023. [Online] Available at: https://d2n4wb9orp1vta.cloudfront.net/cms/brand/am/2020-am/0920-am-csiro-nitinol-1.jpg;maxWidth=1200 [Accessed 08 09 2023].

[20] CNN, 2013. Reflected light from London skyscraper melts car. [Online] Available at: https://edition.cnn.com/2013/09/03/world/europe/uk-london-building-melts-car/index.html [Accessed 09 09 2023].

[21] Constro Facilitator, 2023. [Online] Available at: https://constrofacilitator.com/wp-content/uploads/2020/09/Steel-jacketing.jpg [Accessed 09 09 2023].

[22] Cui , Y. et al., 2018. Thermochromic VO_2 for Energy-Efficient Smart Windows. Joule, Issue 2, pp. 1707-1746.

[23] Cui, H., 2020. A Novel Switchable Thermal Insulation Technology, Cambridge: s.n.

[24] Denz, P.-R.et al., 2021. Smart Textile Sun Shading Development of Functional ADAPTEX Prototypes. Journal of Facade Design and Engineering, 9(1), pp. 101-116.

[25] Dinh, T. D., Weeger, O., Kaijima, S. & Yeung, S. -K., 2018. Prediction of mechanical properties of knitted fabrics under tensile and shear loading: Mesoscale analysis using representative unit cells and its validation. Composites Part B, Issue 148, pp. 81-92.

[26] Duffie, J. A. & Beckman, W. A., 1991. Solar Engineering of Thermal Processes. 2nd ed. New York: Wiley-Interscience.

[27] El Houda, A. N. & Mohamed, D., 2018. Advanced Building Skins Inspired From Plant Adaptation Strategies to Environmental Stimuli: A Review. Médéa, s.n.

[28] European Commission, 2020. In focus: Energy efficiency in buildings. [Online] Available at: https://ec.europa.eu/info/news/focus-energy-efficiency-buildings-2020-lut-17_en [Accessed 21 11 2022].

[29] Fabiani, C. & Pisello, A. L., 2021. Passive cooling by means of adaptive cool materials. In: W. Publishing, ed. Eco-efficient Materials for Reducing Cooling Needs in Buildings and Construction. s.l.:s.n., pp. 439-457`.

[30] Fangueiro, R. & Soutinho, F., 2016. Textile structures. In: Smart Textiles and their Applications. s.l.:Woodhead Publishing Limited, pp. 62-91.

[31] Feringold, A. & Gupta, K., 1970. New analytical approach to the evaluation of configuration factors in radiation from spheres and infinitely long cylinders. Journal of Heat Transfer, 92(1), pp. 69-76.

[32] Fiorito, F. et al., 2016. Shape Morphing Solar Shadings: a review. Renewable and Sustainable Energy Reviews, Issue 55.

[33] Goia, F., Perino, M. & Serra, V., 2014. Experimental Analysis of the energy performance of a full-scale PCM glazing prototype. Solar Energy, Issue 100, pp. 217-233.

[34] Grinham, J., Blabolil, R. & Haak, J., 2014. Harvest Shade Screens: Programming material for optimal energy building skins. Los Angeles, s.n.

[35] Guardian Glass, 2023. Guardian Glass Performance Calculator. [Online] Available at: https://www.guardianglass.com/eu/en [Accessed 20 06 2023].

[36] Hamilton, D. C. & Morgan, W. R., 1952. Radiant-interchange configuration factors, s.l.: NASA.

[37] Ibrahim, A., Abdelmohsen, S., Omar, W. & Zayan, A., 2020. Extending the Passive Actuation of Low-Tech Architectural Adaptive Systems by integrating Hygroscopic and Thermal Properties of Wood. Robotic Tectonics, Automation and Interaction, Volume 2, pp. 641-650.

[38] Iken, O. et al., 2019. Thermal and energy performance investigation of a smart double skin facade integrating vanadium dioxide through CFD simulations. Energy Conversion and Management, Issue 195, pp. 650-671.

[39] Illinois Tool Works Inc., n.d. Elastic Hysteresis. [Online] Available at: https://www.instron.com/en/resources/glossary/e/elastic-hysteresis#:~:text=Elastic%20Hysteresis%20is%20the%20difference,testing%20(loading%20and%20unloading). [Accessed 30 03 2023].

[40] Ingpuls, 2022. Intelligent shading solutions based on shape memory alloys. [Online] Available at: https://smart-shadings.com/#dsgvo [Accessed 05 01 2023].

[41] International Energy Agency, 2018. The Future of Cooling. Paris: s.n.

[42] Jezierski, W. & Zukowski, M., 2023. Evaluation of the Impact of Window Parameters on Energy Demand and CO2 Emission Reduction for a Single-Family House. Energies, 16(4429), pp. 1-20.

[43] Ji, Y. et al., 2022. Skin inspired thermoresponsive polymer for constructing self-cooling system. Energy Conversion and Management, Issue 254, pp. 1-8.

[44] Juaristi, M., Gómez-Acebo, T. & Monge-Barrio, A., 2018. Qualitative analysis of promising materials and technologies for the design and evaluation of Climate Adaptive Opaque Façades. Building and Environment, Issue 144, pp. 482-501.

[45] Juaristi, M., Monge-Barrio, A., Knaack, U. & Gómez-Acebo, T., 2018. Smart and Multifunctional Materials and their Possible Application in Façade Systems. Journal of Facade Design & Engineering, 6(3), pp. 019-033.

[46] Kellogg's Research Labs, 2023. Round Wire. [Online] Available at: https://www.kelloggsresearchlabs.com/product/round-wire/ [Accessed 05 01 2023].

[47] Ke, Y. et al., 2022. Tetra-Fish-Inspired aesthetic thermochromic windows toward Energy-Saving buildings. Applied Energy, Issue 315, pp. 1-9.

[48] Kim, M.-j., Kim, B.-g., Koh, J.-s. & Yi, H., 2023. Flexural biomimetic responsive building facade using a hybrid soft robot actuator and fabric membrane. Automation in Construction, Issue 145, pp. 1-20`.

[49] Kuhn, T. E., 2017. State of the art of advanced solar control devices for buildings. Solar Energy, Issue 154, pp. 112-133.

[50] Kumar, V. V., 2022. Energy Conservation of Residential Buildings in Extreme Climates with Phase Change Material-Aluminum Radiation Reflector Cool Roof. Energy Sources, Part A: Recovery, Utilization, and Environmental Effects, 44(4), pp. 9703-9715.

[51] Lallanilla, M., 2013. This London skyscraper can melt cars and set buildings on fire. [Online] Available at: https://www.nbcnews.com/sciencemain/london-skyscraper-can-melt-cars-set-buildings-fire-8c11069092 [Accessed 22 06 2023].

[52] Lelieveld, C. M. J. L., 2013. Smart Matherials For The Realization Of An Adaptive Building Component, Delft: s.n.

[53] Liang, J. J. et al., 2018. Performance Analysis on Knee Point Selection Methods for Multi-objective Sparse Optimization Problems. Rio de Janeiro, IEEE.

[54] Li, D. et al., 2022. Incorporating phase change materials into glazing units for building applications: Current progress and challenges. Applied Thermal Engineering.

[55] Loonen, R., Trčka, M., Cóstola, D. & Hensen, J., 2013. Climate adaptive building shells: State-of-the-art and future challenges. Renewable and Sustainable Energy Reviews, Issue 25, pp. 483-493.

[56] López-Escamilla, Á., Herrera-Limones, R. & León-Rodríguez, Á. L., 2022. Evaluation of environmental comfort in a social housing prototype with bioclimatic double-skin in a tropical climate. Building and Environment, Issue 218, pp. 1-15.

[57] Luna-Navarro, A., Lori, G., Callewaert, D. & Overend, M., 2023. Semi-automated vs manually controlled dynamic facades: assessment through a field study on multi-domain occupant satisfaction. Energy & Buildings, Issue 286, pp. 1-16.

[58] Mansourizadeh, K., Golahmadi, A., Paoletti, I. M. & Anishchenko, M., 2021. Design of a passive mechanical system actuated by the nitinol helical springs for shading and sustainable development purposes of the buildings. Building and Environment, Issue 187, pp. 1-15.

[59] Markilux, 2023. [Online] Available at: https://mx-static.markilux.com/images/260165/storage/master/02021299.jpg [Accessed 08 09 2023].

[60] Mohtashami, N. et al., 2022. State of the Art of Technologies in Adaptive Dynamic Building Envelopes (ADBEs). Energies, Volume 15.

[61] Mols, T., Blumberga, A. & Karklina, I., 2017. Evaluation of climate adaptive building shells: multi-criteria analysis. Riga, ScienceDirect.

[62] NEN-EN 14500, 2021. Blinds and shutters - Thermal and visual comfort - Test and calculation methods, Bruxelles: European Committee for Standardization.

[63] NEN-EN 14501, 2021. Blinds and shutters - Thermal and visual comfort - Performance characteristics and classification, Bruxelles: European Committee for Standardization.

[64] NEN-EN-ISO 52017-1, 2017. Energy performance of buildings - Sensible and latent heat loads and internal temperatures - Part 1: Generic calculation procedures, Bruxelles: European Committee for Standardization.

[65] NEN-EN-ISO 52022-1, 2017. Energy performance of buildings - Thermal, solar and daylight properties of building components and elements - Part 1: Simplified calculation method of the solar and daylight characteristic for solar protection devices combined with glazing, Bruxelles: European Committee for Standardization.

[66] NEN-EN-ISO 7730, 2005. Ergonomics of the thermal environment - Analytical determination and interpretation of thermal comfort using calculation of the PMV and PPD indices and local thermal comfort criteria, Bruxelles: European Committee for Standardization.

[67] Panjetani Build Well, 2023. [Online] Available at: https://www.panjetanibuildwell.com/blog/wp-content/uploads/2023/02/1550824410791.jpg [Accessed 08 09 2023].

[68] Patankar, S. V., 1980. Numerical Heat Transfer and Fluid Flow. New York: Hemisphere Publishing Corporation.

[69] PeierTech, 2016. Materials. [Online] Available at: http://www.peiertech.com/en/nitinol_wire.html#d1 [Accessed 05 01 2023].

[70] Pesenti, M., Masera, G. & Fiorito, F., 2018. Exploration of Adaptive Origami Shading Concepts through Integrated Dynamic Simulations. Architectural Engineering, 24(4).

[71] Pianosi, F., Sarrazin, F. & Wagener, T., 2015. A Matlab toolbox for Global Sensitivity Analysis. Environmental Modelling & Software, Issue 70, pp. 80-85.

[72] Popescu, M. A., 2019. KnitCrete: Stay-in-place knitter formworks for complex concrete structures, Zurich: ETH Zurich.

[73] Sculpteo, 2023. [Online] Available at: https://www.sculpteo.com/blog/wp-content/uploads/2018/01/Webp.net-resizeimage.jpg [Accessed 08 09 2023].

[74] Seidabadi, L., Ghadamian, H. & Aminy, M., 2019. A Novel Integration of PCM with Wind-Catcher Skin Material in Order to Increase Heat Trnasfer Rate. Int. Journal of Renewable Energy Development, 1(8), pp. 1-6.

[75] Simon, H. A., 1996. The sciences of the Artificial. 3rd ed. Cambridge: MIT Press.

[76] Soother, D. K., Daudpoto, J. & Chowdhry, B. S., 2020. Challenges for practical applications of shape memory alloy actuator. Materials Research Express, Issue 7.

[77] Sporns, O., 2007. Complexity. [Online] Available at: http://www.scholarpedia.org/article/Complexity [Accessed 27 1 2023].

[78] Sun, L. et al., 2012. Stimulus-responsive shape memory materials: A review. Materials and Design 33, pp. 577-640.

[79] Tartarini, F., Schiavon, S., Cheung, T. & Hoyt, T., 2020. CBE Thermal Comfort Tool: Online tool for thermal comfort. SoftwareX, Volume 12.

[80] Tomasetti, T., 2019. Design Explorer. [Online] Available at: https://tt-acm.github.io/DesignExplorer/ [Accessed 18 06 2023].

[81] Umar, J., Hussain, T. & Maqsood, M., 2016. Modeling the mechanical and compression properties of polyamide/elastane knitted fabrics used in compression sportswear. The Journal odf the The Textile Institute, 107(10), pp. 1240-1252.

[82] Umbra Shading, 2023. [Online] Available at: https://umbrashading.co.uk/wp-content/uploads/2022/11/Evolve-for-roller-page.png [Accessed 08 09 2323].

[83] United Nations Department of Economic and Social Affairs, 2022. The Sustainable Development Goals Report 2022, New York: United Nations Publications.

[84] Vassiliadis, S. G., Kallivretaki, A. E. & Provatidis, C. G., 2006. Mechanical simulation of the plain weft knitted fabrics. International Journal of Clothing Science and Technology, 19(2).

[85] Vercesi, L., Speroni, A., Mainini, A. G. & Pli, T., 2020. A Novel Approach to Shape Memory Alloys Applied to Passive Adaptive Shading Systems. Journal of Facade Design and Engineering, 8(1), pp. 43-64.

[86] View, 2023. [Online] Available at: https://view.com/sites/default/files/videos/how_it_works-hero-background-video.jpg [Accessed 08 09 2023].

[87] Voigt, M., Roth, D. & Kreimeyer, M., 2022. Main Characteristic of Adaptive Facades. Cavtav, s.n.

[88] Waqas, A. & Din, Z. U., 2013. Phase change material (PCM) storage for free cooling of buildings - A review. Renewable and Sustainable Energy Reviews, Issue 18, pp. 607-625.

[89] Weeger, O. et al., 2018. Nonlinear Multi-Scale Modelling Simulation and Validation of 3D Knitted Textiles. Applied Composite Material, Issue 25, pp. 797-810.

[90] Wikimedia, 2023. Paraffin. [Online] Available at: https://upload.wikimedia.org/wikipedia/commons/d/d7/Paraffin.jpg [Accessed 08 09 2023].

[91] Yamauchi, K., Ohkata, I., Tsuchiya, K. & Miyazaki, S., 2011. Shape Memory and Superelastic Alloys. s.l.:Woodhead Publishing.

[92] Yi, H. et al., 2020. 3D-printed attachable kinetic shading device with alternate actuation: Use of shape-memory alloy (SMA) for climate-adaptive responsive architecture. Automation in Construction, Issue 114, pp. 1-20.

[93] Yi, H. & Kim, Y., 2021. Self-shaping building skin: Comparative environmental performance investigation of shape-memory-alloy (SMA) response and artificial-intelligence (AI) kinetic control. Journal of Building Engineering, Issue 35, pp. 1-18.

[94] Yoon, J., 2018. Climate-adaptive Facade Design with Smart Materials. Hong Kong, s.n.

[95] Yoon, J., 2019. SMP Prototype Design and Fabrication for Thermo-responsive Facade Elements. Journal of Facade Design and Engineering, 7(1), pp. 41-62.

[96] Yoon, J. & Bae, S., 2020. Performance Evaluation and Design of Thermo-Responsive SMP Shading Prototypes. Sustainability, Issue 12, pp. 1-35.

[97] Zhao, C., Zhang, L. & Zhang, Y., 2023. Exploring the effect of longwave radiation exchange on the energy balance of building façades in subtropical regions. Building and Environment, Issue 223.

APPENDIX A

Script for the penalty function:

```
penVal1 = 1
dist = 0
if val1 > maxVal1:
 dist = val1 - maxVal1
 penVal1 = maxVal1
elif val1 < minVal1:
 dist = minVal1 - val1
 penVal1 = minVal1
if penVal1 == 0:
 p1 = dist
else:
 p1 = dist/penVal1
penVal2 = 1
dist = 0
if val2 > maxVal2:
 dist = val2 - maxVal2
 penVal = maxVal2
elif val2 < minVal2:
 dist = minVal2 - val2
 penVal2 = minVal2
if penVal2 == 0:
 p2 = dist
else:
 p2 = dist/penVal2
 penVal3 = 1
 dist = 0
if val3 > maxVal3:
 dist = val3 - maxVal3
 penVal = maxVal3
elif val3 < minVal3:
 dist = minVal3 - val3
 penVal3 = minVal3
if penVal3 == 0:
 p3 = dist
else:
 p3 = dist/penVal3
penVal4 = 1
dist = 0
if val4 > maxVal4:
 dist = val4 - maxVal4
 penVal = maxVal4
elif val4 < minVal4:
 dist = minVal4 - val4
 penVal4 = minVal4
if penVal4 == 0:
 p4 = dist
else:
 p4 = dist/penVal4
penVal5 = 1
dist = 0
if val5 > maxVal5:
 dist = val5 - maxVal5
 penVal = maxVal5
elif val5 < minVal5:
 dist = minVal5 - val5
 penVal5 = minVal5
if penVal5 == 0:
 p5 = dist
else:
 p5 = dist/penVal5
p = abs(p1) + abs(p2) + abs(p3) + abs(p4) + abs(p5)
p_sqr = math.sqrt(p)
p_fin = p_sqr + 1
```

APPENDIX B

Meteorological data:

Table B.1 gathers the meteorological data used to perform the analysis presented in chapter 6.

Table B.1 Meterorological data used in the thermal analysis presented in chapter 6.

Day and hour	Air temperature [°C]	Wind speed [m/s]	Solar radiation (S) [W/m2]	Longwave radiation [W/m2]	Global hor. Radiation [W/m2]
17-7 03:00	17.8	3	0	381	0
17-7 04:00	18.4	3	0	391	0
17-7 05:00	18.1	1	34	383	40
17-7 06:00	18.1	4	69	376	74
17-7 07:00	18.1	3	117	373	169
17-7 08:00	18.3	5	191.502	383	326
17-7 09:00	17.5	3	315.387066	384	472
17-7 10:00	18.2	5	457.896841	372	590
17-7 11:00	18.0	5	551.901604	351	624
17-7 12:00	18.5	6	586.466293	344	594
17-7 13:00	19.0	6	574.692947	335	531
17-7 14:00	19.6	5	472.117958	342	403
17-7 15:00	19.1	5	342.155292	326	266
17-7 16:00	18.4	6	197.869032	322	143
17-7 17:00	16.8	5	52.097601	337	41
17-7 18:00	16.7	6	2	333	3
17-7 19:00	13.1	3	0	318	0
17-7 20:00	11.8	2	0	304	0
17-7 21:00	10.9	1.8	0	306	0
17-7 22:00	13.1	2.5	0	308	0

Nodes properties:

Tables B.2-5 show the properties and constants of the nodes that have been assumed during the simulations explained in chapter 6:

Air:

Table B.2 Properties and constants for air assumed during the thermal simuation.

Property	Symbol	Value	Unit
Density	ρ	1.249	kg/m^3
Volume expansion coef.	β	0.00355	K^{-1}
Specific heat capacity	Cp	1006	J/(kg*K)
Thermal conductivity	λ	0.025	W/(m*K)
Kinematic viscosity	ν	14.21*10^{-6}	m²/s
Prandtl number	Pr	0.714	-
Rate of air through blind	r	0.001	-
Emissivity (environment)	ε	0.9	-

SMA spring:

Table B.3 Properties and constants for the SMA spring assumed during the thermal simuation.

Property	Value	Unit
External diameter	1.249	kg/m³
Wire diameter	0.00355	K^{-1}
Height activated	1.5	m
Height unactive	0.3	m
Distance from glazing	0.1	m
Specific heat capacity	320	J/(kg*K)
Density	6450	kg/m³
Mass	0.1483	kg
Emissivity	0.3	-

Glazing:

Table B.4 Properties and constants for the glazing assumed during the thermal simuation.

Property	Value	Unit
Width	1	m
Height	1.5	m
Thickness	0.012	m
Specific heat capacity	840	J/(kg*K)
Density	2500	kg/m3
Mass	45	kg
Emissivity	0.15	-

Textile:

Table B.5 Properties and constants for the textile assumed during the thermal simuation.

Property	Value	Unit
Width	1	m
Height	1.2	m
Solar factor ($f_{textile}$)	0.3	-
Emissivity	0.8	-

View factors:

The following view factors were calculated from literature:

(eq. B.1)

$$B = \frac{width_{glazing}}{2 * distance_{glazing-spring}}$$

(eq. B.2)

$$F_{1-2} = \frac{1}{\pi}\tan^{-1} B = 0.4372$$

(Feringold & Gupta, 1970)

(eq. B.3)

$$F_{1-outside} = 1 - F_{1-2} = 0.5628$$

$$F_{2-1} = F_{1-2} * Area_{spring}/Area_{glazing} = 0.0349 \quad \text{(eq. B.4)}$$

$$F_{2-outside} = 1 - F_{2-1} = 0.9651 \quad \text{(eq. B.5)}$$

$$X = \frac{width_{glazing}}{distance_{glazing-spring}} \quad \text{(eq. B.6)}$$

$$Y = \frac{heigth_{textile}}{distance_{glazing-spring}} \quad \text{(eq. B.7)}$$

$$F_{2-3} = F_{3-2} = \frac{2}{\pi XY}\left\{\ln\left[\frac{(1+X^2)(1+Y^2)}{1+X^2+Y^2}\right]^{\frac{1}{2}} + Y\sqrt[2]{(1+X^2)}\tan^{-1}\left(\frac{Y}{\sqrt[2]{(1+X^2)}}\right) + X\sqrt[2]{(1+Y^2)}\tan^{-1}\left(\frac{X}{\sqrt[2]{(1+Y^2)}}\right) - Ytan^{-1}Y - Xtan^{-1}X\right\} = 0.8398 \sim 1 \quad \text{(eq. B.8)}$$

(Hamilton & Morgan, 1952)

Approximated to infinite parallel planes

$$F_{3-outside} = 1 \quad \text{(eq. B.9)}$$

$$F_{1-sky} = 0.5 * F_{1-outside} = 0.2814 \quad \text{(eq. B.10)}$$

$$F_{2-sky} = 0.5 * F_{2-outside} = 0.4826 \quad \text{(eq. B.11)}$$

$$F_{3-sky} = 0.5 * F_{3-outside} = 0.5 \quad \text{(eq. B.12)}$$

Radiative heat transfer coefficients:

For what concerns the heat transfer by radiation between two surfaces the linearised version of the heat transfer coefficient has been used:

$$\alpha_{rad\_1\_2} = 4 * \varepsilon_{res} * \sigma * T_{gem}^3 \quad \text{(eq. B.13)}$$

Where:

ε_{res} is calculated from:

$$\varepsilon_{res} = \frac{\varepsilon_1 * \varepsilon_2}{\varepsilon_1 - \varepsilon_1 * \varepsilon_2 + \varepsilon_2} \quad \text{(eq. B.14)}$$

where ε_1 and ε_2 are the emissivities of the two surfaces [-]

σ is the Stefan Boltzmann constant [5.67*10-8 W/(m²K⁴)]

T_{gem} is the average temperature of the two surfaces [K]

Convective heat transfer coefficients:

Spring:

In case of natural convection the Grashof number expressed by:

$$Gr = \frac{g * \beta * l^3 * \Delta T}{\nu^2} \quad \text{(eq. B.15)}$$

Where:

g is Earth gravity acceleration [9.81 m/s²]

β is the volume expansion coefficient of air [1/K]

l is the characteristic lenght [height of the cylinder in m] (Boetcher, 2014)

ΔT is the temperature difference between the spring and the outside air at the previous timestep [K]

ν is the kinematic viscosity of air [m²/s]

From this the Nusselt Number was calculated as:

$$Nu = 0.56 * (Gr * Pr)^{\frac{1}{4}} \quad if\ Gr * Pr \leq 10^8 \qquad (eq.\ B.16)$$

$$Nu = 0.13 * (Gr * Pr)^{\frac{1}{3}} \quad if\ Gr * Pr > 10^8 \qquad (eq.\ B.17)$$

Where Pr is the Prandtl number.

In case of forced convectiondue to wind the the Reynolds number has been calculated by:

$$Re_D = \frac{u * l}{\nu} \qquad (eq.\ B.18)$$

Where:

u is the metheorological wind speed from the weather file [m/s]

l is the characteristic lenght [diameter of the cylinder in m] (Churchill & Bernstein, 1977)

ν is the kinematic viscosity of air [m²/s]

From this the Nusselt Number was calculated as:

$$Nu = 0.3 + \frac{0.62 * Re_D^{1/2} * Pr^{1/3}}{[1 + (0.4/Pr)^{2/3}]^{1/4}} * \left[1 + \left(\frac{Re_D}{282000}\right)^{5/8}\right]^{4/5} \quad if\ Re_D * Pr \geq 0.2 \qquad (eq.\ B.19)$$

$$Nu = 0.3 + \frac{0.62 * Re_D^{1/2} * Pr^{1/3}}{[1 + (0.4/Pr)^{2/3}]^{1/4}} \quad if\ Re_D * Pr < 0.2 \qquad (eq.\ B.20)$$

Once the Nusselt number was calculated for both cases the heat transfer coefficient derived from:

$$\alpha_{conv\_spring} = \frac{Nu * \lambda}{l} \qquad (eq.\ B.21)$$

Where:

Nu is the Nusselt number calculated previously [-]

l is the characteristic length used for the in calculating the Nusselt number for natural and forced convection [m]

λ is the thermal conductivity of air [W/mK]

Textile and glass to outside:

For the convective heat transfer of these two nodes to the outside air the formula from Akademischer Verein Hütte (2012) was used:

$$\alpha_{convection\_flat} = 6.2 + 4.2 * v_{air} \quad if\ v_{air} < 5 \qquad (eq.\ B.22)$$

$$\alpha_{convection\_flat} = 7.5 * v_{air}^{0.8} \quad if\ v_{air} \geq 5 \qquad (eq.\ B.23)$$

Where v_{air} is the wind speed from meteorological data [m²s]

Textile and glass to cavity:

For the convective heat transfer between these three nodes the equation was taken from Jóhannesson (2006):

$$Nu = 0.18 * \mathrm{Gr}^{\frac{1}{4}} \left(\frac{H}{d}\right)^{-\frac{1}{9}} \quad if \quad 2 * 10^4 < Gr \leq 2 * 10^5 \qquad (eq.\ B.24)$$

$$Nu = 0.065 * \mathrm{Gr}^{\frac{1}{3}} \left(\frac{H}{d}\right)^{-\frac{1}{9}} \quad if \quad 2 * 10^5 < Gr < 2 * 10^7 \qquad (eq.\ B.25)$$

Where:

Gr is Grashof number calculated with characteristic length equal to the depth of the cavity [-]

H is the height of the cavity [m]

d is the depth of the cavity [m]

Sky and ambient equivalent temperatures:

For these two temperatures, the following formulas have been adopted (Zhao, et al., 2023):

$$T_{sky} = \left(\frac{LR_{sky}}{\sigma}\right)^{0.25} \quad \textit{(eq. B.26)}$$

$$T_{ae} = 1.031T_{air} + 0.008SR \quad \textit{(eq. B.27)}$$

Where:

LR_{sky} is the longwave radiation from the sky [W/m2]

σ is the Stefan Boltzmann constant [(5.67*10-8 W/(m2K4)]

T_{air} is the air temperature [C°]

SR is the global horizontal solar radiation [W/m2]